E.O. Paton Electric Welding Institute of the National Academy of Science of Ukraine
International Association «Welding»

The Paton Welding Journal

07
2023

International Scientific-Technical and Production Journal ◊ Founded in January 2000 (12 Issues Per Year)

Address of Editorial Board
E.O. Paton Electric Welding Institute, 11 Kazymyr Malevych Str., 03150, Kyiv, Ukraine
Tel./Fax: (38044) 205 23 90, E-mail: journal@paton.kiev.ua
https://patonpublishinghouse.com/eng/journals/tpwj

State Registration Certificate 24933-14873 ПР from 13.08.2021
ISSN 0957-798X, DOI: http://dx.doi.org/10.37434/tpwj

Subscriptions, 12 issues per year:
$384 — annual subscription for the printed (hard copy) version, air postage and packaging included;
$312 — annual subscription for the electronic version (sending issues in pdf format or providing access to IP addresses).

Representative Office of «The Paton Welding Journal» in China:
China-Ukraine Institute of Welding, Guangdong Academy of Sciences
Address: Room 210, No. 363 Changxing Road, Tianhe, Guangzhou, 510650, China.
Zhang Yupeng, Tel: +86-20-61086791, E-mail: patonjournal@gwi.gd.cn

The content of the Journal includes articles received from authors from around the world in the field of welding, cutting, cladding, soldering, brazing, coating, 3D additive technologies, electrometallurgy, material science, NDT and selectively includes translations into English of articles from the following journals, published in Ukrainian:
- Automatic Welding (https://patonpublishinghouse.com/eng/journals/as);
- Electrometallurgy Today (https://patonpublishinghouse.com/eng/journals/sem);
- Technical Diagnostics & Nondestructive Testing (https://patonpublishinghouse.com/eng/journals/tdnk).

CONTENTS

ORIGINAL ARTICLES

*Translated Article(s) from “Automatic Welding”, No. 7, 2023.

**Translated Article(s) from “Electrometallurgy Today”, No. 2, 2023.

***Translated Article(s) from “Technical Diagnostics & Nondestructive Testing”, No. 2, 2023.

DOI: https://doi.org/10.37434/tpwj2023.07.01

MATHEMATICAL MODELING OF THE IMPACT OF ELECTRODYNAMIC TREATMENT IN THE PROCESS OF ADDITIVE SURFACING ON THE STRESS-STRAIN STATE OF VOLUMETRIC PRODUCTS FROM ALUMINIUM-MAGNESIUM ALLOY

L.M. Lobanov[2], V.M. Korzhyk[1,2], M.O. Pashchyn[2], O.L. Mikhodui[2], P.R. Ustymenko[3], Zhang Yupeng[1], A.O. Alyoshin[2], O.M. Voitenko[2]

[1]China-Ukraine Institute of Welding, Guangdong Academy of Sciences,
Guangdong Provincial Key Laboratory of Advanced Welding Technology
Guangzhou, 510650, China
[2]E.O. Paton Electric Welding Institute of the NASU
11 Kazymyr Malevych Str., 03150, Kyiv, Ukraine
[3]National Technical University of Ukraine «Igor Sikorsky Kyiv Polytechnic Institute»
37 Peremohy Prosp., 03056, Kyiv, Ukraine

ABSTRACT

Combined 3D printing technology including a combination of additive (layer-by-layer) surfacing with electrodynamic treatment of deposited layer was considered. On the basis of mathematical modeling with the use of the Prandtl-Reiss ratio, on the example of aluminium-magnesium AMg6 alloy, the influence of the shape of the indenter for electrodynamic treatment on the distribution of basic parameters and components of the stress-strain state, in particular, the size of the zone of plastic deformations and stresses, depth and width of the contact interaction zone in a metal layer interacting with a roller-indenter moving along the normal to a layer at a speed of 1, 5 and 10 m/s across the thickness of the deposited layer was studied. It was established that the use of a roller with a contact surface, having a shape of a semi-circle, leads to an almost uniform distribution of compression stresses components in the deposited layer, the values of which can reach the yield strength of AMg6 alloy. The results of mathematical modeling give reasons to recommend the use of an electrode in the form of a semicircle (EC) for the development of combined technologies of 3D printing of volumetric metal products, which consist in combination of additive surfacing (WAAM, plasma, microplasma surfacing, etc.) of a volumetric metal product with electrodynamic treatment of each deposited layer.

KEYWORDS: 3D printing, additive surfacing, shaping technologies, electrodynamic treatment, aluminium alloy, impact interaction, mathematical modeling, residual stresses, plastic deformations, roller-indenter, generatrix, elastic-plastic environment

INTRODUCTION

3D printing (additive surfacing) is a method of shaping volumetric products on the base of digital models, the essence of which consists in layer-by-layer reproduction of objects. The use of technologies for 3D printing of parts based on aluminium alloys is promising in the engineering practice of manufacturing high-tech critical structures for the aircraft and space industries. The wide use of aluminium alloys is dictated by the fact that they have a high chemical resistance and a better ratio of strength to specific weight among most structural metal materials [1]. Usually, in the aerospace industry, AK12, AK94, 6061, 7075, AlSi12, AlSi10Mg alloys, etc. are used for 3D printing.

A promising direction of 3D printing is the use of welding technologies, such as layer-by-layer (additive) pulsed-arc surfacing of layers using wires as a shaping material (WAAM technology — Wire Direct Energy Deposition/Wire Arc Additive Manufacturing), as well as plasma (microplasma) layer-by-layer surfacing using powders or wires as additive materials, etc. [1, 2]. In these technologies, the material is deposited layer-by-layer by a robotic manipulator (or 3D positioner) according to the 3D model, as a result of which a three-dimensional workpiece is produced for further machining in a machine-tool with a numerical control (CNC) [3, 4].

It should be noted that, from the point of view of safe operation of aerospace engineering structures, the presence of even minimal defects in the structure of 3D printed parts of aluminium alloys is critically important for making a decision on the suitability of the specified technology. On the one hand, there is a need to refine the microstructure and improve the fatigue strength of parts produced by additive surfacing [4]. On the other hand, in the mentioned technologies

Figure 1. Process of 3D printing with plastic deformation of the deposited layer by electrodynamic treatment: *1* — torch for 3D printing; *2* — cylindrical electrode-indenter with the contact surface in the form of a straight line; *3* — printed layer of metal

there are risks of occurrence and the need in eliminating such a defect as discontinuity of material [5].

To solve these problems, electrodynamic treatment (EDT), which is one of the promising methods of influencing the structure of the surface layers of metal materials and regulating the stress-strain state (SSS), can be used [6]. EDT technology can be implemented in a combined process together with additive surfacing. The EDT process of the printed (deposited) layer is close to that in welding conditions, where the executive device (electrode system) moves behind the welding torch at a distance L_{EDT} behind it [7]. The values of L_{EDT} specify the temperature T_{EDT} of heating a printed layer as a result of the action of the thermal cycle of surfacing, at which its electrodynamic treatment can be carried out. At the same time, EDT can be applied to a printed layer, whose metal is at elevated or room temperatures.

Experimental and numerical methods of SSS analysis are used to study the EDT process. The work [8] considered the results of the numerical calculation of the process of impact interaction of the electrode-indenter with the plate of AMg6 during EDT based on the Prandtl–Reiss equations [9], which describe the movement of the medium in a planar two-dimensional formulation in the ANSYS/LS-DYNA software package.

The electrode-indenter for compacting a printed layer by the EDT method can be designed as a cylindrical roller with a different shape of the contact surface, for example, in the form of a straight line (Figure 1). The results of mathematical modeling of the impact of different structural forms of the indenter during EDT on residual welding stresses are presented in [10].

The results of [10] proved that a designed shape of the indenter during EDT has a significant impact on the distribution of residual welding stresses in the plate of AMg6 alloy. Control of welding stresses, including the formation of compressive stresses, is precisely one of the important tasks in the development of additive surfacing technologies. Considering the abovementioned, it should be noted that the shape of the contact surface of the indenter for EDT should affect the characteristics of the plastic deformation of the metal after 3D printing, which is determined by the formation of compressive stresses in it. Thus, optimization of the geometric shape of the contact surface of the roller-indenter for EDT, which performs the treatment of the deposited layer, can generally improve the mechanical characteristics of a printed metal.

The aim of the work is to evaluate, based on the mathematical modeling, the impact of the shape of the electrode-indenter on the distribution of components of plastic deformations and residual stresses during the formation of volumetric metal products in the combined process of "additive surfacing - layer-by-layer electrodynamic treatment".

CALCULATION (MATHEMATICAL) MODEL OF THE PROBLEM

Mathematical modeling of residual stress states after EDT of welded joints is considered in detail in [8]. The scheme of the EDT process of the plate metal after 3D printing is shown in Figure 2. During EDT, the electrodynamic pressure on the disc *2* of a non-ferromagnet (Figure 2, *a*) and the indenter *4* is the result of the interaction of eddy currents with the pulsed magnetic field of the inductor 1 when the contactor *K* starts the discharge cycle of the capacitor *C* [6].

Figure 2 shows that in the EDT process, the copper electrode-indenter *4* and the deposited layer *5* of AMg6 alloy with a thickness $\delta = 4$ mm and a width of 50 mm, which in the calculations is taken in the form of a plate located on a completely rigid surface (working table *6*), interact with impact. At the same time, the electrode-indenter moves in the direction (along the normal) to the plate *5* at a speed V_0. Geometric symmetry in modeling allows using only a half of the plate and indenter, located to the right of the line of electrodynamic pressure V_0 in Figure 2, *b*, *c*. In modeling, it is assumed that the cross-section of a printed layer does not exceed the cross-section of the plate.

Thus, the numerical calculation using a planar two-dimensional model in the Lagrangian setting will correspond to the modeling of the EDT process of the plate by electrode-indenter with a profiled contact surface in the form of a semicircle — EC (Figure 2, *b*) or in a planar shape (EP) (Figure 2, *c*). The difference between the two presented calculation schemes consists in the fact that the contact of EC surface and the plate occurs at a point (Figure 2, *b*), and the contact of EP surface and the plate occurs along the line (Figure 2, *c*).

The creation of a mathematical model of the process described above was carried out using a simplified two-dimensional (2D) planar setting. The problem was solved using the ANSYS/LS-DYNA software [8–10]. A planar two-dimensional finite element in the form of SOLID162 rectangle was used to construct the finite element mesh of the problem. Taken into account that the stress-strain state of solid bodies is considered in this problem, the computer modeling should be carried out using the Lagrangian approach [8–10]. As is known, the Lagrangian approach uses a moving finite-element mesh that is rigidly connected to the environment and deforms together with it.

The presence of the abovementioned described geometric symmetry of impact-interacting bodies allows considering only half of their cross-section relative to *OY* axis with the simultaneous imposition of the corresponding boundary conditions. These conditions include banning the movement of nodes of the finite element mesh (FEM) of bodies located on the axis of symmetry in the horizontal direction *OX*. The presence of the working table 6 in the scheme of electrodynamic treatment of the plate (Figure 2, *a*) is rational to be replaced by resting on an absolutely rigid base, which in the mathematical setting will be equivalent to banning movement in the vertical direction *OY* to the FEM nodes that belong to the lower surface of the plate *5*, which is in contact with the table.

A finite element with a maximum characteristic size of 0.1 mm was chosen to construct the finite element model of the plate and electrode-indenter. The constructed finite element models for both variants of the calculation scheme had the same number of finite elements (SOLID 162 type) — 4288 and the same number of nodes — 4514, where the electrode-indenter had 2688 elements and 2797 nodes, and the plate consisted of 1600 elements and 1717 nodes.

For numerical modeling of a high-speed impact process, a continuous model of the experimental medium was used [8–10]. The basis of the model is the hypothesis about the continuity of changes in the characteristics of the medium in space (coordinate, time), which allows recording the laws of conservation of mass, amount of motion and energy in the form of partial differential equations.

If we choose a Cartesian (rectangular) coordinate system to describe the adiabatic motion of an elastic-plastic medium with a density ρ (kg/m^3), then the system of the corresponding equations in the two-dimensional setting will have the form [9]:

The equation of continuity:

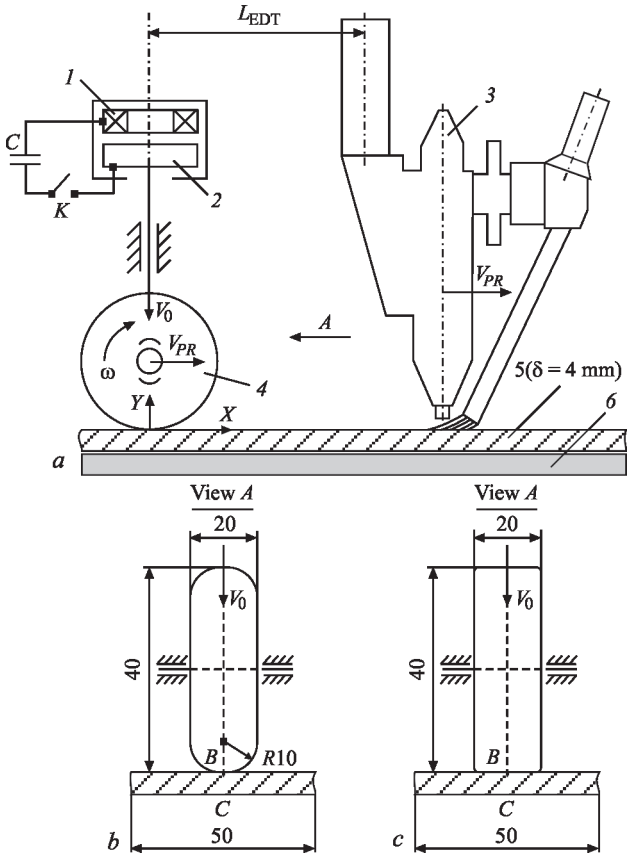

Figure 2. Process of EDT of plate metal after 3D printing: *a* — scheme of EDT process after 3D printing: *1* — inductor; *2* — disc; *3* — torch for 3D printing; *4* — indenter; *5* — plate for 3D printing with the thickness δ; *6* — working table; *C* — capacitor; *K* — contactor-switch; L_{EDT} — distance between the torch *3* and the indenter *4*; *X*, *Y* — axis of action of stresses; V_0 — line of electrodynamic pressure direction; V_{PR} — direction of 3D printing; ω — direction of rotation; *b* — geometric characteristics of the electrode-indenter with the contact surface in the form of a semicircle (EC), where B and C are the points along the line of V_0 respectively on the outer and back surfaces of the plate *5* (Figure 2, *a*); *c* — geometric characteristics of the electrode-indenter with the contact surface of a planar shape (EP), where *B* and *C* — similar to *b*)

$$\frac{d\rho}{dt}+\rho\left(\frac{\partial u}{\partial x}+\frac{\partial v}{\partial y}\right)=0, \qquad (1)$$

where *u*, *v* are the components of the velocity vector of the medium, m/s.

The equation of motion of the medium:

$$\rho\frac{du}{dt}=\frac{\partial\sigma_{xx}}{\partial x}+\frac{\partial\sigma_{xy}}{\partial y},\ \rho\frac{dv}{dt}=\frac{\partial\sigma_{yx}}{\partial x}+\frac{\partial\sigma_{yy}}{\partial y}, \qquad (2)$$

where σ_{ij} are the components of the stress tensor, Pa.

The energy equation E^* for a unit of mass:

$$\rho\frac{dE*}{dt}=\sigma_{xx}\dot{\varepsilon}_{xx}+\sigma_{yy}\dot{\varepsilon}_{yy}+2\sigma_{xy}\dot{\varepsilon}_{xy},$$

$$\dot{\varepsilon}_{xx}=\frac{\partial u}{\partial x},\quad \dot{\varepsilon}_{yy}=\frac{\partial v}{\partial y},\quad \dot{\varepsilon}_{xy}=\frac{1}{2}\left(\frac{\partial u}{\partial y}+\frac{\partial v}{\partial x}\right), \qquad (3)$$

where $\dot{\varepsilon}_{ij} = \frac{d\varepsilon_{ij}}{dt}$ are the components of the strain rate tensor, (s^{-1}).

To study the processes associated with large plastic deformations of the medium, finite deformations and the theory of plastic flow are used. This theory considers the plastic deformation of a solid body as a state of motion. The corresponding Prandtl–Reiss ratios can be written as:

$$\frac{dD_{\sigma_{xx}}}{dt} + 2G\dot{\lambda}D_{\sigma_{xx}} = 2G\left(\dot{\varepsilon}_{xx} + \frac{1}{3\rho}\cdot\frac{d\rho}{dt}\right), \quad (4)$$

$$\frac{dD_{\sigma_{yy}}}{dt} + 2G\dot{\lambda}D_{\sigma_{yy}} = 2G\left(\dot{\varepsilon}_{yy} + \frac{1}{3\rho}\cdot\frac{d\rho}{dt}\right), \quad (5)$$

$$\frac{dD_{\sigma_{xy}}}{dt} + 2G\dot{\lambda}D_{\sigma_{xy}} = 2G\dot{\varepsilon}_{xy}, \quad (6)$$

where G is the shear modulus, Pa; D_{ij} is the stress deviator components:

$$D_{ij} = \sigma_{ij} + p\delta_{ij},\ \delta_{ij} = 1\ (i = j),\ \delta_{ij} = 0\ (i \neq j), \quad (7)$$

where p is the average normal stress, Pa:

$$p = -\frac{\sigma_x + \sigma_y + \sigma_z}{3}.$$

The value of the specific power of plastic deformation is determined as:

$$\dot{\lambda} = \frac{3}{2Y^2}\sigma_{ij}\dot{\varepsilon}^p_{ij}, \quad \left(\frac{1}{\text{Pa}\cdot\text{s}}\right), \quad (8)$$

where Y is the dynamic yield strength of the material under study.

The system of equations is closed by the equation of the medium state in the form:

$$p = p(\rho, E). \quad (9)$$

In the mathematical setting, the behavior of the materials of the plate (aluminium AMg6 alloy) and electrode-indenter (copper M1) under the action of an external pulsed load was described using an ideal elastic-plastic rheological model of the material, which is available in the materials library of the ANSYS/LS-DYNA software. For this model, the value of the dynamic yield strength of material Y was accepted to be equal to the value of the yield strength σ_y. The corresponding values of the parameters of this model in the work were accepted as follows:

A plate with sizes of 500×500×4 mm of aluminium AMg6 alloy:

- density ρ = 2640 kg/m^3;
- modulus of elasticity E = 71 GPa;
- Poisson's ratio μ = 0.34;
- yield strength σ_y =150 MPa.

The electrode-indenter of M1 copper alloy with a mass of 102.5 g obtains three values of V_0, namely, 1, 5 and 10 m/s:

- density ρ = 8940 kg/m^3;
- modulus of elasticity E = 128 GPa;
- Poisson's ratio μ = 0.35;
- yield strength σ_y = 300 MPa.

Throughout the whole area of motion of an ideal-plastic medium, the ratio should be fulfilled, representing the Mises yield condition:

$$D^2_{\sigma_1} + D^2_{\sigma_2} + D^2_{\sigma_3} \leq \frac{2}{3}Y^2, \quad (10)$$

where D_{σ_1}, D_{σ_2} and D_{σ_3} are the main components of the stress deviator, Pa.

Thus, to evaluate the impact of EC and EP shape on the EDT efficiency of AMg6 alloy after 3D printing, numerical calculations of the process of their interaction with the plate at the contact speeds V_0 = 1, 5 and 10 m/s were carried out based on Prandtl–Reiss ratios. The value of V_0 was set based on the electrophysical characteristics of the capacitor C + inductor system (Figure 2, *a*), which are used for EDT [8].

MODELING RESULTS AND COMPARISON OF TECHNOLOGICAL APPROACHES

As a result of modeling, geometric characteristics of the cross-section of the deposited (printed layer 3) were established, Figure 1, which can be deformed by EDT in a one pass as a result of its contact interaction with the electrode-indenter (EC or EP) at different values of the speed V_0. The values of the height h_{PR} and width b_{PR} of the printed layer, subjected to EDT shaping during the period of the contact interaction t_{EDT} are given in Table 1.

The value of h_{PR} was determined as one, equal to the depth of the indentation as a result of a normal introduction of the indenter into the deposited layer at the point *B* (Figure 2, *b*, *c*) from its initial position to the position corresponding to the end of the contact. It was assumed that the value of h_{PR} of the layer, at which its deformation flush with the surface of the plate is guaranteed, should be not less than the depth of the indentation. The value of b_{PR} of the layer was determined as the distance from the impact line (axis *Y* in Figure 2, *a*) to the point that is located flush with the surface of the plate. The calculation of the values of h_{PR} and b_{PR}, which was carried out without taking into account the conditions of compressed or free plastic deformation [11], should be considered simplified. But the calculation results are sufficient for selecting the additive surfacing mode, which provides

Table 1. Parameters of contact interaction of the electrode and geometric characteristics of the deposited layer subjected to shaping by EDT

Number	Electrode shape	Electrode speed V_0, m/s	Contact duration t_{EDT}, μs	Layer height h_{PR}, mm	Layer width b_{PR}, mm
1	EP	1	74	0.016	0.53
2		5	86	0.168	1.89
3		10	102	0.451	3.06
4	EC	1	166	0.049	1.27
5		5	128	0.266	2.56
6		10	120	0.547	3.76

the required values of h_{PR} and b_{PR} of the printed layer, which can be subjected to EDT.

From the data in Table 1, it is seen that t_{EDT} between the layer and EP increases by 28 μs (38 %) with a rise in the initial speed of movement V_0 by an order. When using EC, on the contrary, an increase in V_0 to 10 m/s leads to a decrease in t_{EDT} by 46 μs (27 %). This is explained by the peculiarities in the energy exchange processes between the electrode-indenter and the plate. In accordance with an increase in the speed V_0, the kinetic energy grows, which during contact is converted into the energy of plastic deformation at the place of the contact, which affects the sizes of h_{PR} and b_{PR} of the compacted layer on the plate.

A rise in V_0 from 1 to 5 and up to 10 m/s increases the size of h_{PR} in both problem statements. At the same time, the values of h_{PR} and b_{PR} for EP increase by 10 and 3.6 times, respectively, when the speed grows to 5 m/s, and at V_0 = 10 m/s, the values of h_{PR} and b_{PR} increase by 2.5 and 1.6 times. At the same time, for EC, the growth is less rapid, the depth and width increase at V_0 = 5 m/s by 5.4 and 2 times, respectively, and at V_0 = 10 m/s they increase by another 2 and 1.4 times, respectively.

To evaluate the level of plastic deformations, the effective plastic deformations ε_{eff}^{p} were used, which represent a scalar value of the plastic component of the tensor of strain rate, which grows when the stress state is at the level of the yield strength. The values ε_{eff}^{p} were determined by the formula [10]:

$$\varepsilon_{eff} = \frac{\sqrt{2}}{3}\sqrt{(\varepsilon_1 - \varepsilon_2)^2 + (\varepsilon_2 - \varepsilon_3)^2 + (\varepsilon_3 - \varepsilon_1)^2}, \quad (11)$$

where ε_1, ε_2, ε_3 are the main deformations.

Although, an increase in the values of h_{PR} and b_{PR} for EP is more intensive, the absolute values of the geometric sizes of the compacted cross-section at the same speeds are greater for EC, which leads to a corresponding increase in the effective plastic deformations ε_{eff}^{p} and sizes of the plastic deformation zone (Figure 3). It should be noted that the boundaries of the plastic deformation zone, marked with an arrow, were determined under the condition that $\varepsilon_{eff}^{p} \geq 0.01$.

From Figure 1, it is seen that the zone of ε_{eff}^{p} distribution grows with an increase in V_0 and the shape of the distribution changes from a circle segment to a shape close to a trapezoid. The area of the plastic deformation zone increases faster during EC treatment (Figure 3, *b*). EDT at V_0 = 5 m/s does not deform the back surface of the metal when using EP (Figure 3, *a*) in contrast to the option of using EC (Figure 3, *b*). On the other hand, at the same V_0, it can be seen that the width of the deformation zone on the face surface at EC is 2 times larger than at EP. This proves the advantages of the shape EC over EP, as a technological tool for plastic deformation of metal of the next printed layer during additive surfacing.

Thus, the use of EDT at a speed of 1 m/s allows obtaining the surface effect of deformation with a segment radius with the center at the contact point of 0.7 and 1.6 mm size at EP and EC shapes of the electrode, respectively. When the speed increases to 5 m/s, EP provides a deformation zone with a radius of 2 mm, and EC forms a zone in the form of a trapezoid with a larger base on the face surface of 4 mm and a smaller base of 1.9 mm. An increase in V_0 up to 10 m/s leads to the creation of the plastic deformation zone of in the form of a trapezoid in both cases, with a larger and smaller base of 3.3 and 1.1 mm, respectively, at EP, and 6.2 and 4.7 mm, respectively, at EC.

Also, from Figure 1 it is seen, that as V_0 grows, not only the sizes of the plastic deformation zone increases, but also the values of ε_{eff}^{p} accordingly, it can be said here that when applying EP, the maximum values are formed on the contact surface of the printed layer with the electrode closer to the plane of symmetry. In the case of using EC, on the contrary, the peak values of ε_{eff}^{p} are shifted by 1.8–2.0 mm from the impact line (axis of symmetry) with the transition from the segmental shape of the deformation zone to the trapezoidal one. To compare the values of the maximum ε_{eff}^{p} and the values of ε_{eff}^{p} at the points *B* and *C* (Figure 2, *b*, *c*), located along the impact line, are given in Table 2.

Analyzing the data in Table 2 and Figure 1, it can be said that a growth of V_0 in the general case leads

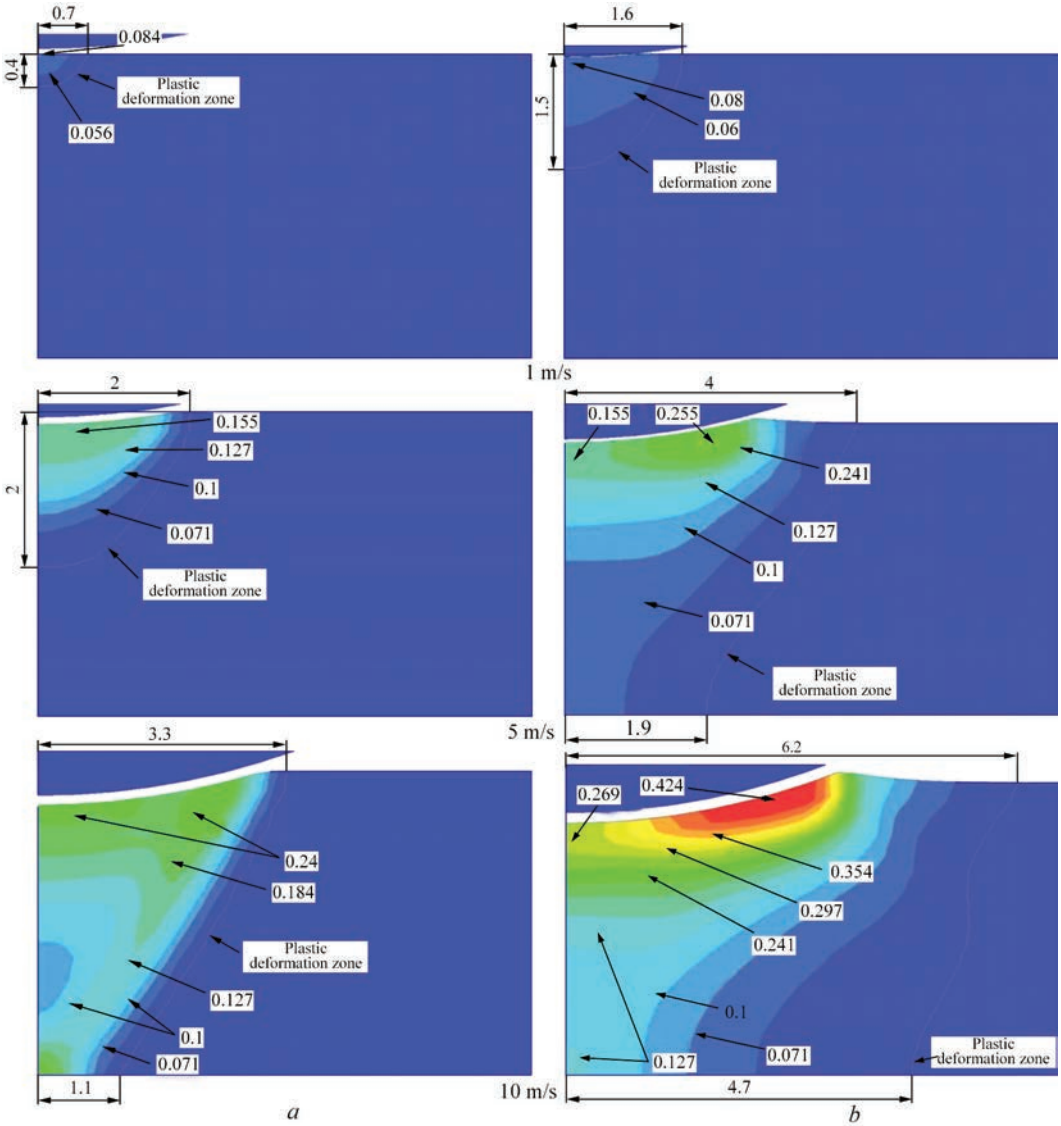

Figure 3. Calculated distribution of effective plastic deformations ε_{eff}^{p} along the OX axis along the line V_0 (Figure 2) in the plate after EDT EP (*a*) and after EDT EC (*b*) at the values of speed V_0 = 1, 5 and 10 m/s

to an increase in the maximum values of ε_{eff}^{p} regardless of the shape of the electrode. When using EP, an increase in V_0 from 1 to 5 m/s leads to an increase in the maximum ε_{eff}^{p} by 2.9 times, and a further increase to 10 m/s contributes to an increase by another 30 %. When using EC, the corresponding growth values are slightly higher: at 5 m/s — by 3.8 times, and at 10 m/s — by another 1.8. Thus, it can be seen that the use of the contact surface of EC contributes to a greater intensity of compaction at EDT than in EP.

The geometric characteristics of the deformation zone when using EC or EP have some differences. But if we consider the distribution of ε_{eff}^{p} at a speed of 1 m/s, then ε_{eff}^{p} concentrate on the face surface, and their values do not exceed 6 %, with a gradual decrease to zero along the impact line regardless of the shape of the electrode.

With an increase in V_0 to 5 m/s at EP, the distribution of ε_{eff}^{p} reaches the middle of the plate, but still has a superficial character with the maximum values on the contact surface being 17 % and a gradual decrease to almost zero on the back surface of the plate. The use of EC forms a trapezoidal deformation zone with the concentration of the maximum ε_{eff}^{p} at its edge with the value of up to 17.1 %. In this case, the value of ε_{eff}^{p} along the impact line gradually decreases from 15.1 % on the face surface to 3.8 % on the back one.

During treatment at V_0 = 10 m/s using EP, ε_{eff}^{p} have a trapezoidal distribution with the highest values on the back and face surfaces, from 22.4 to 20.5 %, respectively. In this case, the boundary of the plastic deformation zone represents almost a straight line, and the maximum values of ε_{eff}^{p} are at the point C. Also, at a distance of 2.5 mm from the face surface along the impact line, a local reduction in ε_{eff}^{p} to 8.5 % is observed, which should be taken into account when determining the critical zones of destruction when designing printed products. At the same time, the use of

Table 2. Values of effective plastic deformations ε_{eff}^{p}

Number	Electrode shape	Electrode-indenter speed, m/s	Maximum values ε_{eff}^{p}	ε_{eff}^{p} values on plate surfaces	
				Face (point *B*)	Back (point *C*)
1	EP	1	0.06	0.06	0
2		5	0.171	0.165	0.004
3		10	0.224	0.205	0.224
4	EC	1	0.063	0.04	0
5		5	0.239	0.151	0.038
6		10	0.424	0.260	0.116

EC at V_0 = 10 m/s determines the geometric shape of the deformation zone, which is qualitatively similar to the zone at V_0 = 5 m/s, but with a greater value of ε_{eff}^{p} — up to 42.4 %. At the same time, on the impact line, the values of ε_{eff}^{p} decrease from the point *B* to the point *C* from 26 to 11.6 %, respectively.

The distributions of ε_{eff}^{p} (Figure 3) are the result of the impact of the electrode shape at EDT on the overall intensity of plastic deformation of the metal, which characterizes its compaction at 3D printing. With the aim of more in-depth evaluation of the nature of the compaction of the printed metal, the distribution of ε_{x}^{p} and ε_{y}^{p} components along the axes *OX* and *OY* (Figure 2) of ε_{eff}^{p} deformation was calculated. The distribution of ε_{x}^{p} values determines the nature of deformation along the direction of V_{RR} printing (Figure 2), and the distribution of ε_{y}^{p} components along the impact line of V_0 (Figure 2). The distribution of ε_{x}^{p} components is shown in Figure 2.

Comparing ε_{x}^{p} for all cases, it is seen that with an increase in speed, the effect of the striker action on its distribution grows. At V_0 = 1 and 5 m/s, ε_{x}^{p} does not reach noticeable values at EP, but with an increase in V_0 to 10 m/s on the back surface at the point *C*, the deformation zone with the value more than 19 % ε_{x}^{p} is formed. In this case, the distribution of ε_{x}^{p} in the central up to cross-section has a form that is close to an isosceles triangle.

At the same time, at EC, a gradual increase in the intensity of deformation with an increase in V_0 from 1 m/s to 10 m/s is observed, where an accompanying increase in ε_{y}^{p} on the contact surface and in the zone near the symmetry axis (*Y*) is observed. At the same time, a zone of negative values up to –26 % is formed on the face surface on the boundary of the interaction surface of the plate with the electrode.

When considering the distribution of ε_{y}^{p} plastic deformation components, we have a more dynamic picture of the change in the process with a growing speed (Figure 5).

Considering the distribution of ε_{y}^{p} plastic deformation components at EP, the creation of a zone of negative values on the contact surface of the plate in the form of a circle segment is observed. With an increase in V_0, it grows over the plane and transforms into a trapezoid with the bases on the surfaces of the plate.

While analyzing the action of EC, the effect from the growth of speed is higher than when using EP. A transition from the zone of negative values on the contact surface in the form of a circle segment to a trapezoid-shaped zone at V_0 = 5 m/s and a rectangle at V_0 = 10 m/s is observed. The local zone of positive peak values at the border of the contact surface at V_0 = 1 m/s is absent, but becomes noticeable at V_0 = 5 and 10 m/s.

In order to analyze the distribution of values of stress state components over the thickness of the plate, the correpsonding calculated pictures of σ_x (Figure 6) and σ_y (Figure 7) distribution were constructed, which determine the characteristics of the printed metal during EDT with the use of EC or EP.

With an increase in the initial speed of the electrode-indenter, it is possible to conditionally see the trajectory of movement of compression and tension zones regarding the overall kinetics of changing the distribution of field σ_x and σ_y stress components. Thus, if we consider the distribution of σ_x at a speed of 1 m/s at EP (Figure 6, *a*), it is possible to see the origination of the tension zone along the plane of symmetry on the contact surface, behind which, the compression zone, and after it again the tension zone are created.

At a speed growth of up to 5 m/s, the extension of a near-surface tension area from the point of impact along the surface of the point *B* (Figure 2) is observed. In this case, the compressive stress zone extends to a half of the thickness of the plate, and across the width — behind the area of EP contact with a printed layer. The tension zones in the form of circle segments with the center in the point *C* (Figure 2) are formed on the back surface of the plate, where the peak value of σ_x reaches 76 MPa.

A growth in the speed of V_0 to 10 m/s leads to an increase in the surface tension zone across the thickness of the plate and in value. In this case, the compression stress zone decreases both by sizes and in

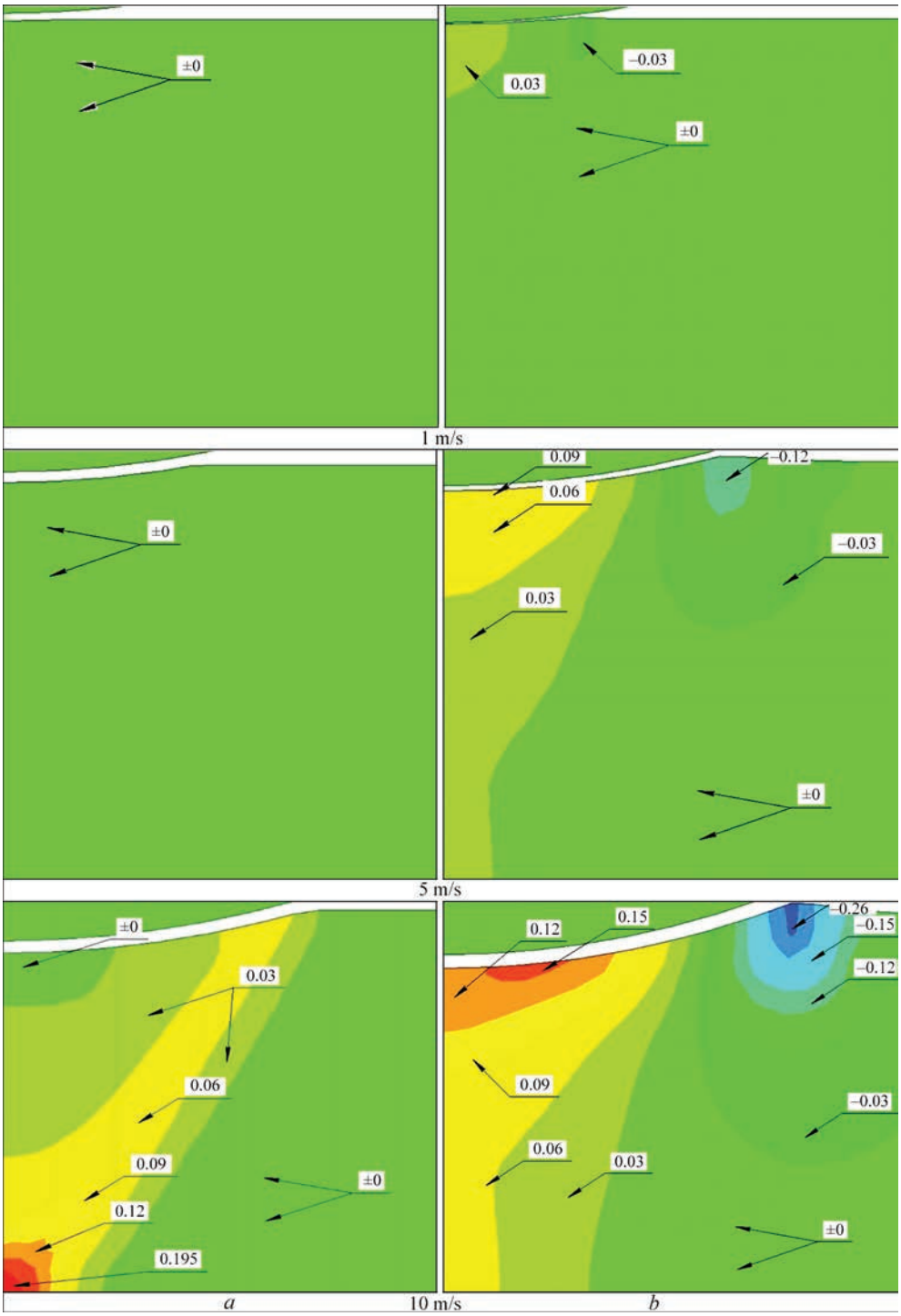

Figure 4. Calculated distribution of plastic deformations ε_x^p for the electrode shape of EP (*a*) and EC (*b*) at the initial speeds V_0 of the electrode of 1, 5 and 10 m/s

value, moving to the middle of the plate. At the same time, tensile stresses in the vicinity of the point *B* decrease and the geometric sizes of the zone decrease. The creation of a new compression zone on the back surface symmetrically to the surface tension zone is noted.

The plastic deformation of the deposited layer metal with the use of EC is more efficient (than with EP), because it leads to the dominance of σ_x compression zones throughout the area of action and values (compared to tension zones). At the same time, the value and area of distribution of compression σ_x grows with an increase in V_0.

At EDT by EC, already at V_0 = 1 m/s, a compression zone of about –200 MPa is created, which extends to the upper half of the thickness of the plate. The zone of the highest concentration of compression stresses with a peak value is at a depth of 1 mm from the face surface of the plate, and its width is equal to the width of the contact zone of EC with the metal. In the lower half of

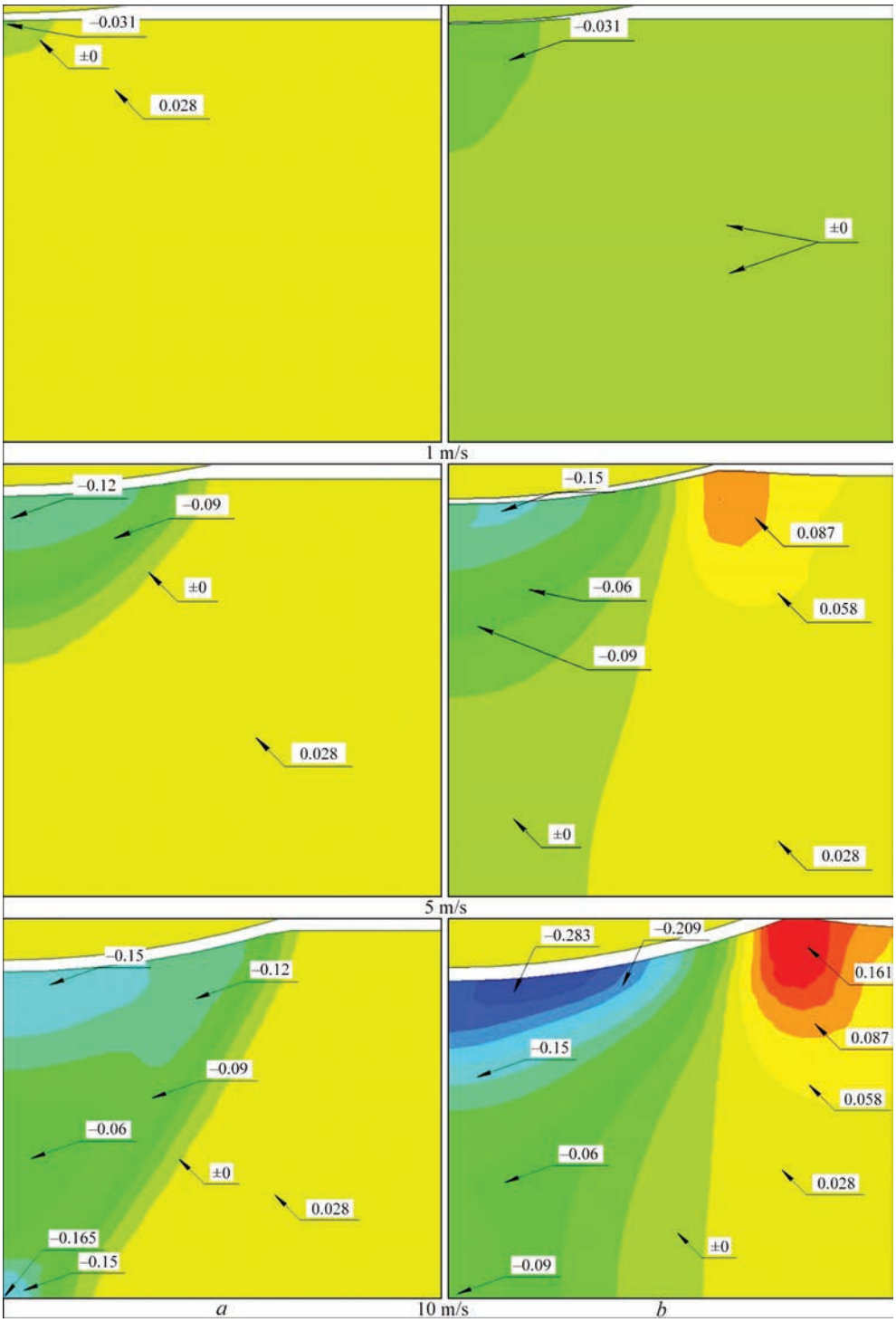

Figure 5. Calculated distribution of plastic deformations ε_y^p for the electrode shape of EP (*a*) and EC (*b*) at the initial speeds V_0 of the electrode of 1, 5 and 10 m/s

the thickness of the plate, the tension zone near the axis of symmetry is formed, the width of which also corresponds to the width of the contact zone. The maximum values of σ_x in this zone reach 25 MPa.

The growth of V_0 to 5 m/s throughout the whole thickness of the plate in the treatment zone forms a compression stress with two concentration zones. One of them is created in the form of a circle segment on the surface of the plate behind the edge of the contact zone, and the other is formed across the thickness of the plate with a uniform compression with the values close to the conditional yield strength $\sigma_{0.2}$ of AMg6 alloy (150 MPa).

The use of EC at V_0 = 10 m/s leads to an increase in the compression stresses to –200 MPa behind the contact zone. In this case, the compression zone in the thickness of the plate is shifted in its minimum to the point *C*, where peak values reach –200 MPa.

At the same time, the distribution of σ_y has its own features, which are shown in Figure 7. In general con-

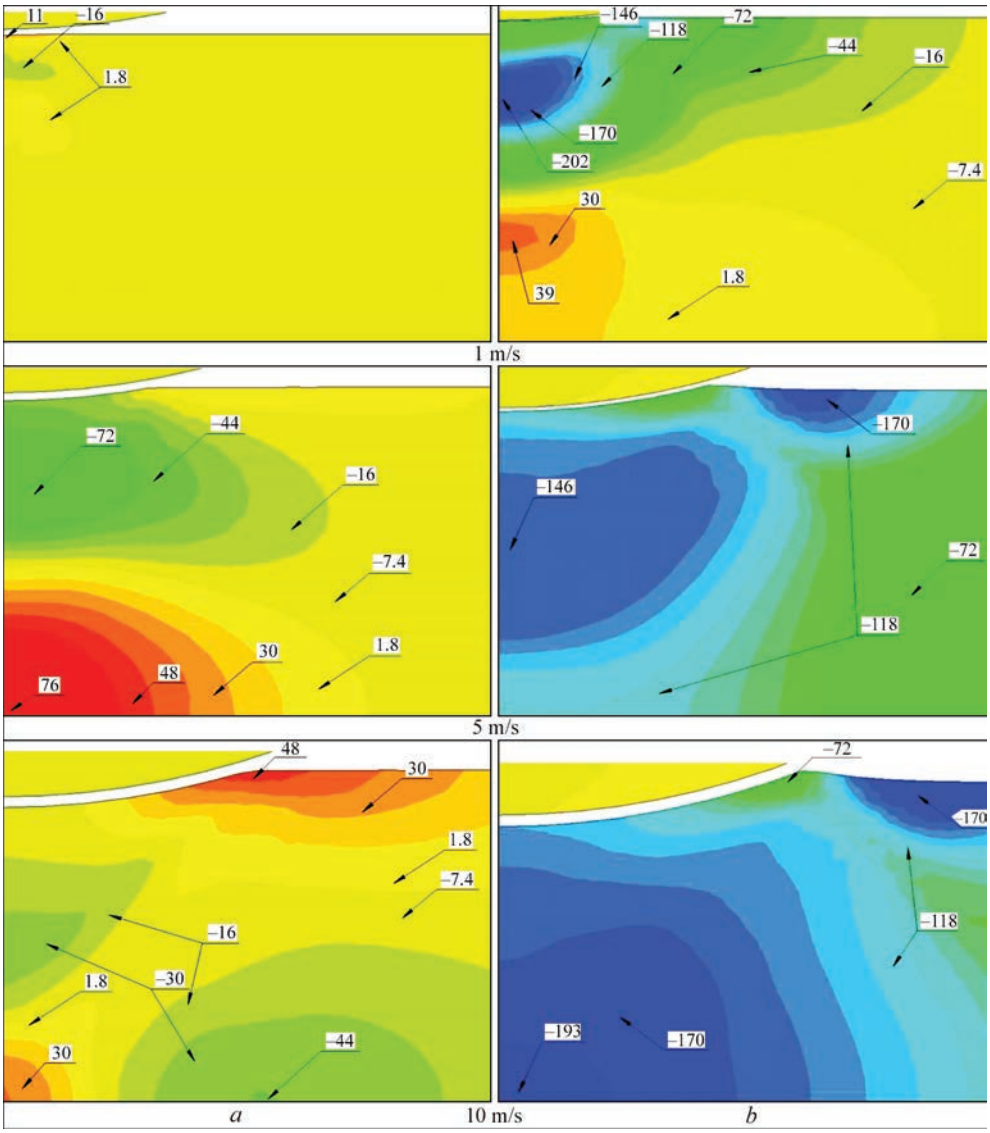

Figure 6. Distribution of residual σ_x stresses (MPa) as a result of EDT using EP (*a*) and EC (*b*) at the initial speeds V_0 of the electrode of 1, 5 and 10 m/s

sideration of evolution of σ_x stress component in EDT with the use of EP, a transition from a slight change in the stress state at V_0 = 1 m/s to the formation of two pronounced tension and compression zones at an increase in the speed to 5 and 10 m/s is observed. The tension zone, which is created at the peak at the point *C*, is similar to a rectangle with an elongated angle in the direction of the dent boundary. The compression zone, formed behind the tension zone, has a shape similar to a triangle with a base on the back surface and the vertex, which with an increase in the speed approaches the dent edge. At V_0 = 5 and 10 m/s, no significant changes in the stress state on the face surface compared to the state at V_0 = 1 m/s is observed.

When considering the distribution, the stress σ_y components in EDT with the use of EC, the formation of alternate tension and compression zones is also observed. The compression zone is created under the dent surface in the form of a circle segment, the outer radius of which reaches a half of the thickness of the plate at V_0 = 1 m/s. At V_0 = 5 and 10 m/s, the area of the compression zone extends to the entire thickness of the plate, and reaches the dent edge across its width, reducing the area of the tension zone and moving it from the impact line. At the same time, with an increase in speed, the shape of the tension zone is converted into a pointed strip with the edge vertex near the dent edge.

The results of the calculation of the values of σ_x and σ_y residual stress components at the reference points along the impact line are summarized in Tables 3 and 4.

Based on the data of Table 3, it can be seen that σ_x component at V_0 = 1 m/s when using EP is exclusively tensile and at EC acquires a negative sign already in the upper half of the thickness of the plate. At the same time, due to intensive plastic deformation, the values of σ_x stresses at EC at V_0 = 1 m/s reach 202 MPa, i.e.

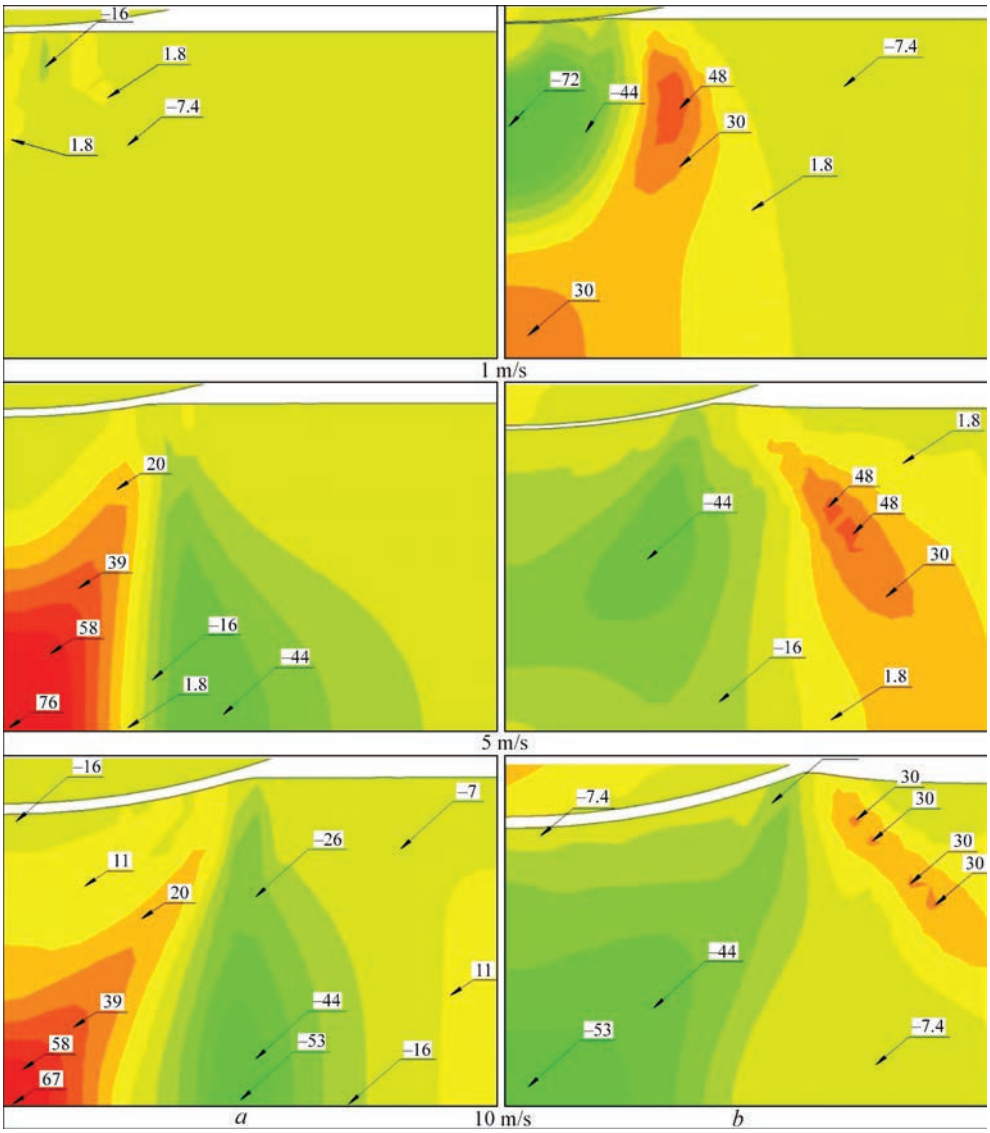

Figure 7. Distribution of values of residual σ_y stresses (MPa) as a result of EDT using EP (*a*) and EC (*b*) at the initial speeds V_0 of the electrode of 1, 5 and 10 m/s

they are behind the elasticity limit on the local area under the contact surface (at a point at a distance of 1 mm from the surface).

In the range of V_0 = 5–10 m/s, the values of σ_x acquire a negative sign on the upper half of the plate when applying EP and are exceptionally negative when using EC. Also, at V_0 = 5–10 m/s when using EP, the compression σ_x values on the upper half of the plate are close to tensile σ_x on the lower one.

During an increase in V_0, the use of EC allows increasing the value of compression σ_x stresses and their distribution zone. The compression stresses reach the values close to the yield strength of the material over the entire thickness of the metal.

Analyzing the distributions of σ_x component (Table 4), it should be noted that the value of this stress component is significantly lower compared to σ_y. Thus, when applying EP, the effect on the face half of the plate along the impact line is minimal regardless of the speed. At the same time, at speeds of 5 and 10 m/s, an increase in tensile stresses on the back half of the plate of up to 78 MPa is observed.

The use of EC throughout the whole speed range initiates the formation of compression σ_y stresses within –5– –36 MPa, except for the point at a thickness of

Table 3. Calculated values of residual stress state σ_x components (in MPa) over the thickness of the plate (from the point *B* to the point *C* (see Figure 2))

Electrode shape	V_0, m/s	Point coordinate over the thickness of the plate (along the impact line), mm				
		0 (point *B*)	1	2	3	4 (point *C*)
EP	1	15	4	1	0	0
	5	–25	–61	–2	59	76
	10	–6	–7	–16	13	32
EC	1	–29	–202	–16	21	13
	5	–133	–160	–164	–153	–128
	10	–147	–163	–166	–177	–180

Table 4. Calculated values of residual stress state σ_y components (in MPa) over the thickness of the plate (from the point *B* to the point *C* (see Figure 2))

Electrode shape	V_0, m/s	Point coordinate over the thickness of the plate (along the impact line), mm				
		0 (point *B*)	1	2	3	4 (point *C*)
EP	1	–7	2	0.5	0	0
	5	0.1	0.1	23	61	78
	10	0.1	5	12	40	60
EC	1	–5	–79	–24	21	21
	5	0	–12	–18	–17	–7
	10	–3	–20	–25	–36	40

1 mm from the face surface at a speed of treatment of 1 m/s, where σ_y = –79 MPa. But on the back side, a localized tension zone of up to 40 MPa is formed.

Based on the abovementioned comparisons of values of stress state components along the impact line (Tables 3, 4), it should be noted that, unlike the shape of the electrode-indenter EP, the use of EC shape leads to the formation of almost uniform distribution of both stress components (σ_x and σ_y) across the thickness of the deposited layer. In addition, the use of EP leads to the formation of both compression stresses, as well as more dangerous tensile stresses with the values that can reach half of the value of the material yield strength. Whereas, the use of EC leads to the formation of both σ_x and σ_y compression stress components, the values of which can reach the yield strength of the material. As was shown in [12–14], such distribution of plastic deformations contributes to refinement of the metal structure, and the resulted distribution of components of compression stresses facilitates an increase in the resistance to the destruction of products in the conditions of fatigue loads.

Thus, by combining electrodynamic treatment with additive surfacing, an improvement in the physical and mechanical characteristics of the material of metal products in 3D printing technologies can be expected.

CONCLUSIONS

1. Based on the Prandtl–Reiss ratio, numerous experiments on studying the effectiveness of the influence of the shape of the contact surface of the electrode-indenter for electrodynamic treatment of the deposited layer in the technologies of additive surfacing on the distribution of components of plastic deformations and residual stresses in it were carried out.

2. It was established that the use of the copper electrode-indenter in the form of a roller with a contact surface in the form of a semicircle (EC) for EDT compared to the electrode with a contact surface in the form of a straight line (EP), which moves under the same conditions, results in:

● an increase in the duration of the contact with the deposited layer treated by 50 % and, as a result of this, the sizes of the depth and width of the layer increase by 55 and 35 %, respectively;

● distribution of the deposited layer of the zone of effective plastic deformations, having a shape close to trapezoid, across the entire thickness (in the case of EP, the zone of ε_{eff}^{p} extends only to a half of the thickness of the plate and has a shape of a circle segment), and the values of maximum deformations at EC are 1.4 times higher than the action of EP;

● formation of almost uniform distribution of both stress state σ_x and σ_y components over the thickness of the plate, which, unlike EP, are the compression stresses, the values of which can reach the yield strength of AMg6 alloy.

3. The results of the mathematical modeling give reason to use the shape of the electrode-indenter — EC for the development of combined technologies of 3D printing of volumetric metal products, which consist in the combination of layered (additive) surfacing (WAAM, plasma, microplasma surfacing, etc.), a volumetric product with electrodynamic treatment of each deposited layer.

The work was performed with the support of the following projects:

● *The National Key Research and Development Program of China (grant number 2020YFE0205300).*

● *GDAS'Project of Science and Technology Development (2020GDASYL-20200301001), China.*

REFERENCES

1. Peleshenko, S., Korzhyk, V., Voitenko, O. et al. (2017) Analysis of the current state of additive welding technologies for manufacturing volume metallic products (review). *Eastern European J. of Enterprise Technologies*, **87**, 42–52. DOI: https://doi.org/10.15587/1729-4061.2017.99666
2. Kvasnytskyi, V., Korzhyk, V., Lahodzinkyi, I. et. al. (2020) Creation of Volumetric Products Using Additive Arc Cladding with Compact and Powder Filler Materials. In: *Proc. of the 2020 IEEE 10th Inter. Conf. on Nanomaterials: Applications and Properties (Sumy, Ukraine, 9–13 Nov. 2020)*, 02SAMA16-1-02SAMA16-5, DOI: https://doi.org/10.1109/NAP51477.2020.9309696
3. Soshi, M. (2017) Innovative grid molding and cooling using an additive and subtractive hybrid CNC machine tool. *CIRP Annals – Manufacturing Technology*, 66(**1**), 401–404.
4. Dongqing, Yang, Gang, Wang, Guangjun, Zhang (2017) Thermal analysis for single-pass multi-layer GMAW based additive manufacturing using infrared thermography. *J. Materials Proc. Technology*, **244**, 215–224.
5. Trufyakov, V.I. (1973) *Fatigue of welded joints.* Kyiv, Naukova Dumka [in Russian].
6. Lobanov, L.M., Pashchyn, N.A., Kondratenko, I.P. et al. (2018) Development of post-weld electrodynamic treatment using electric current pulses for control of stress-strain states and improvement of life of welded structures. *Materials*

Performance and Characterization, **7**(**4**). DOI: https://doi.org/10.1520/MPC20170092
7. Lobanov, L.M., Korzhyk, V.M., Pashchyn, M.O. et al. (2022) Deformation-free TIG welding of AMg6 alloy with application of electrodynamic treatment of weld metal. *The Paton Welding J.,* **8**, 3–8. DOI: https://doi.org/10.37434/tpwj2022.08.01
8. Lobanov, L.M., Pashchyn, M.O., Mikhodui, O.L. et al. (2017) Effect of the indenting electrode impact on the stress-strain state of an AMg6 alloy on electrodynamic treatment. *Strength of Materials*, 49(**3**), 369–380.
9. Sidorenko, Y.M., Shlenskii, P. (2013) On the assessment of stress-strain state of the load-bearing structural elements in the tubular explosion chamber. *Strength of Materials*, 45(**2**), 210–220.
10. Lobanov, L.M., Pashchyn, M.O., Mikhodui, O.L. et al. (2022) Influence of electrode shape on stress-strain state of AMg6 alloy during its electrodynamic treatment. *The Paton Welding J.,* **9**, 3–10. DOI: https://doi.org/10.37434/as2022.09.01
11. Johnson, K. (1989) *Mechanics of contact interaction.* Moscow, Mir [in Russian].
12. Lobanov, L.M., Pashchin, N.A., Solomijchuk, T.G. (2012) Changes of structure of aluminium alloy AMg6 in the zone of electrodynamic actions. *Visnyk Ukr. Materialoznavchogo Tovarystva,* **5**, 30–42 [in Russian].
13. Lobanov, L.M., Pashchin, E.N., Berdnikova, E.N. (2015) Influence of electrodynamic treatment on features of fracture mictomechanism of aluminium alloy AMg6 at cyclic loading. *Visnyk Ukr. Materialoznavchogo Tovarystva,* **8**, 27–37 [in Russian].
14. Lobanov, L.M., Pashin, N.A., Timoshenko, N. et. al. (2017) Effect of the electrodynamic treatment on the life of AMg6 aluminium alloy weld joints. *Strength of Materials*, 49(**2**), 234–238. DOI: http://dx.doi.org/10.1007/s11223-017-9862-8

ORCID
L.M. Lobanov: 0000-0001-9296-2335,
V.M. Korzhyk: 0000-0001-9106-8593,
M.O. Pashchyn: 0000-0002-2201-5137,
O.L. Mikhodui: 0000-0001-6660-7540,
P.R. Ustymenko: 0000-0002-5318-2675,
A.O. Alyoshyn: 000-001-9696-6800

CONFLICT OF INTEREST
The Authors declare no conflict of interest

CORRESPONDING AUTHOR
M.O. Pashchyn
E.O. Paton Electric Welding Institute of the NASU
11 Kazymyr Malevych Str., 03150, Kyiv, Ukraine.
E-mail: svarka2000@ukr.net

SUGGESTED CITATION
L.M. Lobanov, V.M. Korzhyk, M.O. Pashchyn, O.L. Mikhodui, P.R. Ustymenko, Zhang Yupeng, A.O. Alyoshin, O.M. Voitenko (2023) Mathematical modeling of the impact of electrodynamic treatment in the process of additive surfacing on the stress-strain state of volumetric products from aluminium-magnesium alloy. *The Paton Welding J*., **7**, 3–14.

JOURNAL HOME PAGE
https://patonpublishinghouse.com/eng/journals/tpwj

Received: 14.06.2023
Accepted: 06.09.2023

DOI: https://doi.org/10.37434/tpwj2023.07.02

FEATURES OF FORMATION AND TRANSFORMATION OF OXIDES IN FLASH-BUTT WELDING OF K76F RAILS

V.I. Shvets, I.V. Ziakhor, L.M. Kapitanchuk

E.O. Paton Electric Welding Institute of the NASU
11 Kazymyr Malevych Str., 03150, Kyiv, Ukraine

ABSTRACT

The transformation of oxide inclusions in flash-butt welding (FBW) of K76F rails was studied with the use of the Auger-microprobe JAMP 9500F of JEOL Company (Japan) with the X-ray energy dispersion spectrometer INCA Penta FET x3 mounted on it and involvement of the most informative methodologies of fractographic analysis. It is shown that high-temperature oxide inclusions without changing the aggregate state are removed as a flash. On the basis of silicon oxides on a molten surface in the welding process, easy fusible ferromanganese and in the near-contact layer — manganese silicates are formed. The heterogeneity of silicon distribution is the cause of formation of clusters of silicates and formation of "matt spots" in the near-contact layer.

KEYWORDS: flash-butt welding, KF76 rails, silicates, "matt spots"

INTRODUCTION

Nonmetallic inclusions (NI) violate the integrity of metal and, having excellent mechanical and physical properties, exert a significant impact on its mechanical and operational properties [1]. Modern converter rail steels are characterized by the presence of the following NI in the structure: globular sulphides and manganese oxides, in-line ferromanganese sulphides, complex oxides containing silicon, aluminium and calcium elongated along the direction of rolling. The listed NI represent non-removed products of deoxidation and desulfurization of steel [2].

In thermal deformation conditions of welding, it is possible to transform NI with a probable enhancement of their negative impact. In [3], the problem of flashing of ferromanganese sulphides in the near-contact layer of rails is considered. The flashing is caused by the existence of eutectics with a melting point of 1164 °C in the Fe–Mn–S system. It is shown that after flashing, the melt spreads along the structural boundaries. During cooling of welded joints, opening of metal may occur on the formed cast interlayers. Such a defect is manifested by the means of US testing. The joint in this case is recognized as defective. The danger is posed by cracking over these layers during operation after laying the rails in the track. Here it is recommended to use a welding mode, during which the heat input is reduced in order to hinder the process of flashing sulphides at the stage of coagulation before the spread of the melt along the intergranular boundaries [4].

Simple oxides, encountered in the metal of rails, are characterized as refractory — their melting point is much higher than the melting point of iron — 1538 °C. At the same time, the data of studying the state diagrams indicate the existence of easy fusible eutectics in oxide systems [5]. The presence of easy fusible eutectics gives grounds to suggest about a probable flashing of both complex oxides, as well as products of diffusion interaction of oxides with the matrix in FBW. The formation of a liquid phase with its subsequent crystallization may cause additional inner stresses in the metal and reduce the properties of joints.

The aim of the work was to establish the features of formation and transformation of oxide inclusions in rail steels in FBW.

PROCEDURE AND EQUIPMENT

The joints of K76F rails, produced in the K1000 machine for flash-butt welding by the technology developed at PWI of NASU, were considered [6]. The studies of NI were performed on the fracture surfaces of the joints after tests for static bending. The examinations of the microstructure of the fracture surface and determination of the chemical composition of structural components were conducted with the use of the Auger-microprobe JAMP 9500F of JEOL Company (Japan) with the X-ray energy dispersion spectrometer INCA Penta FET x3 of Oxford Instrument Company, mounted on it. The power of the primary electron beam was 10 KeV at a current of 0.5 nA for the SEM and EPMA methods and at a current of 10 nA for the Auger-electron spectroscopy method. The Auger-spectra were registered with the energy separation ability $\Delta E/E = 0.6$ %. Before the examinations, the surface of the specimens was subjected to

cleaning directly in the analysis chamber of the device by argon Ar+ ions etching with the energy of 1 keV during 10 min. The rate of SiO_2 etching over the reference witness specimen was 4 nm/min. The vacuum in the analysis chamber was within $5 \cdot 10^{-6}$–$5 \cdot 10^{-7}$ Pa. Metallographic examinations were performed in the optical NEOPHOT 32 microscope, equipped with a digital camera. Microstructure was revealed by etching of preliminary polished specimens in a 4 % alcohol HNO_3 solution.

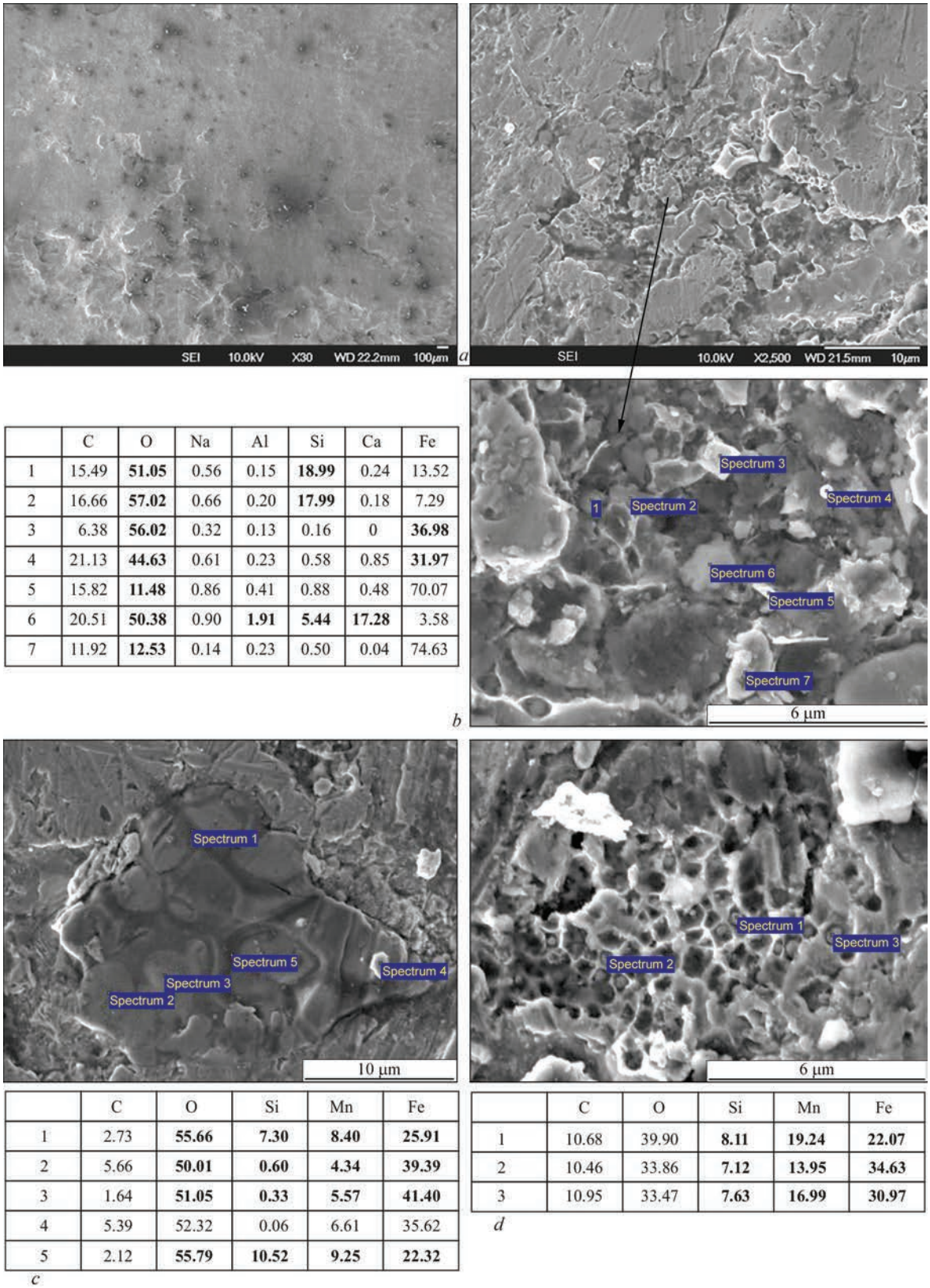

	C	O	Na	Al	Si	Ca	Fe
1	15.49	**51.05**	0.56	0.15	**18.99**	0.24	13.52
2	16.66	**57.02**	0.66	0.20	**17.99**	0.18	7.29
3	6.38	**56.02**	0.32	0.13	0.16	0	**36.98**
4	21.13	**44.63**	0.61	0.23	0.58	0.85	**31.97**
5	15.82	**11.48**	0.86	0.41	0.88	0.48	70.07
6	20.51	**50.38**	0.90	**1.91**	**5.44**	**17.28**	3.58
7	11.92	**12.53**	0.14	0.23	0.50	0.04	74.63

b

	C	O	Si	Mn	Fe
1	2.73	**55.66**	**7.30**	**8.40**	**25.91**
2	5.66	**50.01**	**0.60**	**4.34**	**39.39**
3	1.64	**51.05**	**0.33**	**5.57**	**41.40**
4	5.39	52.32	0.06	6.61	35.62
5	2.12	**55.79**	**10.52**	**9.25**	**22.32**

c

	C	O	Si	Mn	Fe
1	10.68	39.90	**8.11**	**19.24**	**22.07**
2	10.46	33.86	**7.12**	**13.95**	**34.63**
3	10.95	33.47	**7.63**	**16.99**	**30.97**

d

Figure 1. Microstructure of fracture surface in the area of "cold welding": *a* — general appearance; *b–d* — results of X-ray microanalysis of nonmetallic inclusions (at.%)

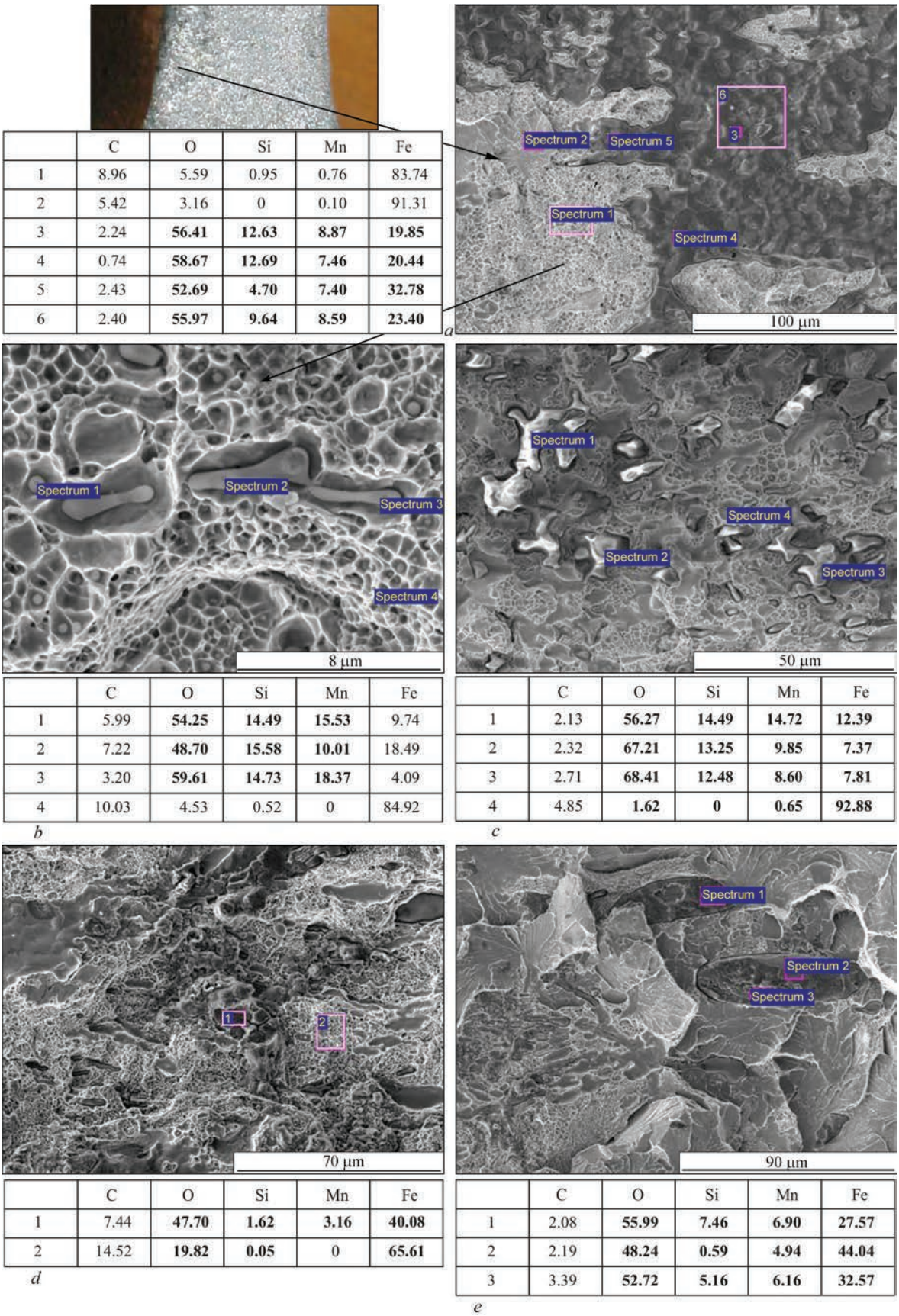

	C	O	Si	Mn	Fe
1	8.96	5.59	0.95	0.76	83.74
2	5.42	3.16	0	0.10	91.31
3	2.24	**56.41**	**12.63**	**8.87**	**19.85**
4	0.74	**58.67**	**12.69**	**7.46**	**20.44**
5	2.43	**52.69**	**4.70**	**7.40**	**32.78**
6	2.40	**55.97**	**9.64**	**8.59**	**23.40**

a

	C	O	Si	Mn	Fe
1	5.99	**54.25**	**14.49**	**15.53**	9.74
2	7.22	**48.70**	**15.58**	**10.01**	18.49
3	3.20	**59.61**	**14.73**	**18.37**	4.09
4	10.03	4.53	0.52	0	84.92

b

	C	O	Si	Mn	Fe
1	2.13	**56.27**	**14.49**	**14.72**	**12.39**
2	2.32	**67.21**	**13.25**	**9.85**	**7.37**
3	2.71	**68.41**	**12.48**	**8.60**	**7.81**
4	4.85	**1.62**	**0**	**0.65**	**92.88**

c

	C	O	Si	Mn	Fe
1	7.44	**47.70**	**1.62**	**3.16**	**40.08**
2	14.52	**19.82**	**0.05**	0	**65.61**

d

	C	O	Si	Mn	Fe
1	2.08	**55.99**	**7.46**	**6.90**	**27.57**
2	2.19	**48.24**	**0.59**	**4.94**	**44.04**
3	3.39	**52.72**	**5.16**	**6.16**	**32.57**

e

Figure 2. Microstructure of fracture surface in the "lack of fusion" area: *a* — general appearance; *b*–*e* — results of X-ray microanalysis of nonmetallic inclusions (at.%)

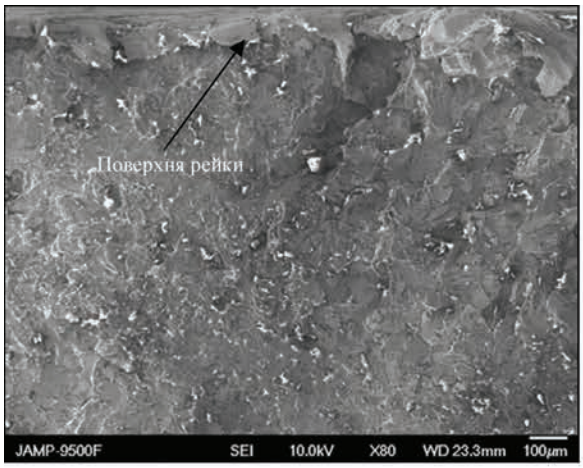

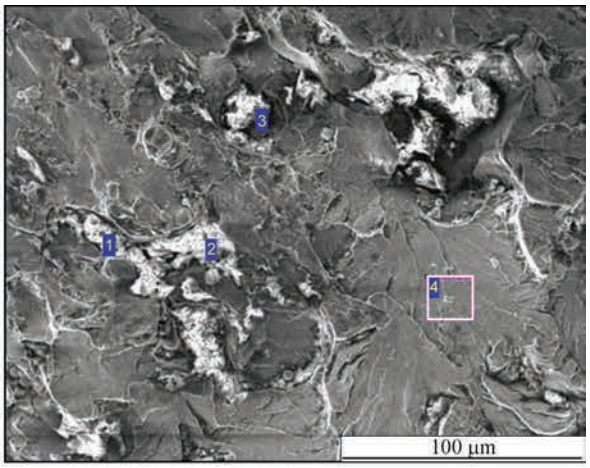

	C	O	Na	Mg	Al	Si	S	Cl	K	Ca	Fe
1	65.54	**23.93**	0.62	0.26	**1.32**	**1.04**	0.50	0.26	0.32	**2.54**	**3.70**
2	32.24	**33.83**	0.31	0.51	**2.08**	**1.09**	0.40	0.50	0.23	**1.29**	**27.52**
3	65.48	5.79			**4.76**	**16.05**	1.04		2.05	**1.80**	**3.04**
4	8.34	6.74			0.40	0.92					83.60

a

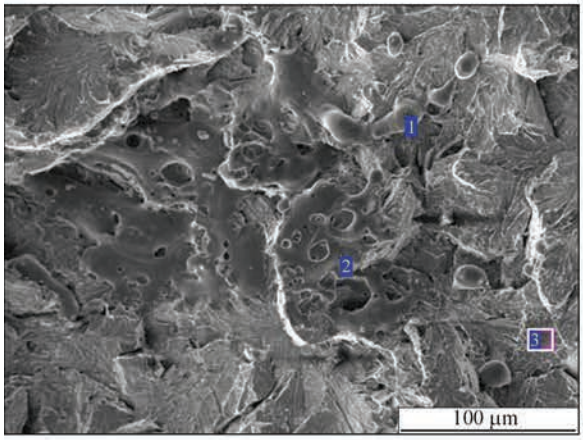

b

	C	O	Si	Mn	Fe
1	7.57	**23.32**	0.21	0	**68.89**
2	3.09	**57.02**	0.98	0.10	**38.82**
3	5.43	3.53	1.37	0.23	89.43

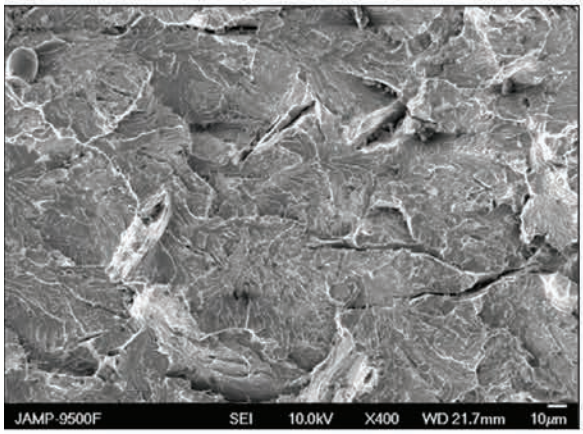

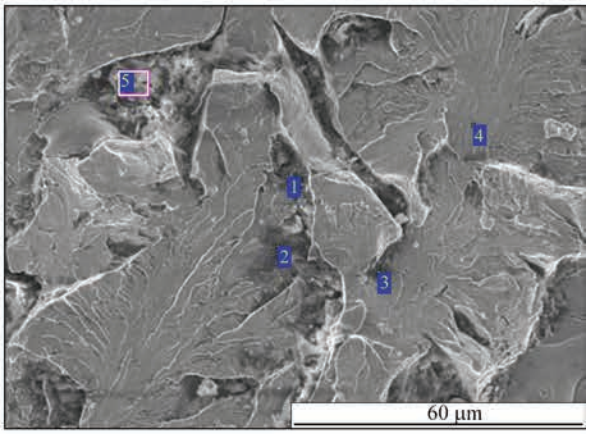

	C	O	Na	Al	Si	S	Ca	Fe	Cu
1	**71.29**	13.13	0.23	0.29	0.92	–	0.61	13.53	–
2	**73.69**	14.97	–	**1.34**	0.68	–	–	9.32	–
3	**70.75**	17.11	0.10	**1.17**	0.81	0.23	0.69	9.16	–
4	7.85	3.36	–	–	**1.26**	–	–	**87.53**	–
5	**67.52**	**24.46**	–	**2.13**	**1.29**	0.15	1.08	2.96	0.27

c

Figure 3. Microstructure of fracture surface and results of X-ray microanalysis of nonmetallic inclusions in the area of incomplete removal of the melt as a flash: *a* — refractory oxides; *b* — iron oxides; *c* — secondary cracks (at.%)

RESEARCH RESULTS AND DISCUSSION

The fracture surface of the rail joints produced on the optimal mode is crystalline. On the opened welding defects formed in the case of deviation of the mode parameters from the optimal ones, the surface is visually flat. To get a more complete notion of the formation and transformation of NI along with the study on the surface of the crystalline fracture and in the near-contact layer of the joint, the formation of structural components in the regions of such welding defects as "cold welding" and "lack of fusion" was considered [7].

The peculiarity of "cold welding" consists in the insufficient heating of rail before upsetting and, as a consequence, a partial flashing of the end. The fracture surface in this region of opening is flat (Figure 1). Within the flat surface, refractory nonmetallic inclusions, such as oxides of silicon, aluminium, complex oxides, including aluminium, calcium, silicon, globular iron oxides are observed (Figure 1, *b*). Near the oxides, flashed-type silicates in the form of films (Figure 1, *c*) and clusters of tiny globular particles are encountered, the size of which amounts to fractions of a micron (Figure 1, *d*). Globular particles are a product of ferromanganese film fragmentation and cause a locally tough nature of the fracture.

Lacks of fusion are formed in the places of more intense penetration. On the fracture surface, lacks of fusion are distinguished as smooth regions, that do not have a distinct crystalline structure. According to the results of X-ray microanalysis, a layer of ferromanganese silicate (Figure 2, *a*, spectrum 3) makes a bulk part of the lack of fusion surface. Within the lack of fusion, films of an easy fusible iron oxide — wüstite are encountered (Figure 2, *d*, spectrum 1). In the layers of ferromanganese silicates, as well as in the wüstite films, the clusters of globular particles with the size of less than 1 μm are revealed (Figure 2, *b*, spectrum 1). The particles are films fragmentation products of ferromanganese silicates and wüstite, respectively. A negligible size of particles causes a tough nature of the fracture in the regions of their location.

In the transition zone on the boundary of the lack of fusion area with a crystalline fracture, the inclusions of flashed-type ferromanganese silicates with a reduced content of iron compared to the layer of ferromanganese silicates are encountered (Figure 2, *c*). There, films of ferromanganese silicates with elevated ferro content are encountered (Figure 2, *e*).

As is seen, the structural components observed on the surface of the lack of fusion, belong to the Si–Mn–Fe–O system. The prerequisite for their formation is obviously the presence of eutectics with a temperature of 1178 and 1117 °C [4] in the SiO_2–FeO system, as well as unlimited solubility in the MnO–FeO system [8]. Obviously, that in the process of welding, an oxidation of metal of flashed rail ends occurs. On the surface, first of all, an easy fusible iron oxide (wüstite) with some content of manganese is formed. The interaction of the near-surface silicon oxide with iron oxide and an increase in the content of diffusion-active manganese leads to the formation of ferromanganese silicates. The source of manganese can be both the rail metal, as well as its refractory oxides. The presence and distribution of silicon oxide inclusions in the surface layer determines the chemical composition and morphology of structural components of the lack of fusion surface.

In FBW, the rail metal, flashed on the ends, is removed during upsetting beyond the boundaries of a workpiece cross-section. Together with the melt, oxidation products of the surface layer and NI, contained in the melt, are removed. While studying the fracture area with an incomplete removal of the melt, numerous inclusions of complex oxides of aluminium, calcium and silicon were found (Figure 3, *a*). There, globular and film oxides of iron are encountered (Figure 3, *b*). A typical feature of the microstructure is secondary cracks of up to 100 μm in size (Figure 3, *c*). The cracks contain small oxide inclusions observed on the background of carbon content, elevated up to 50–70 at.%. A high carbon content is associated with its redistribution in thermal-deformation conditions of welding and filling the volumes on the boundary of nonmetallic inclusions and matrix [9].

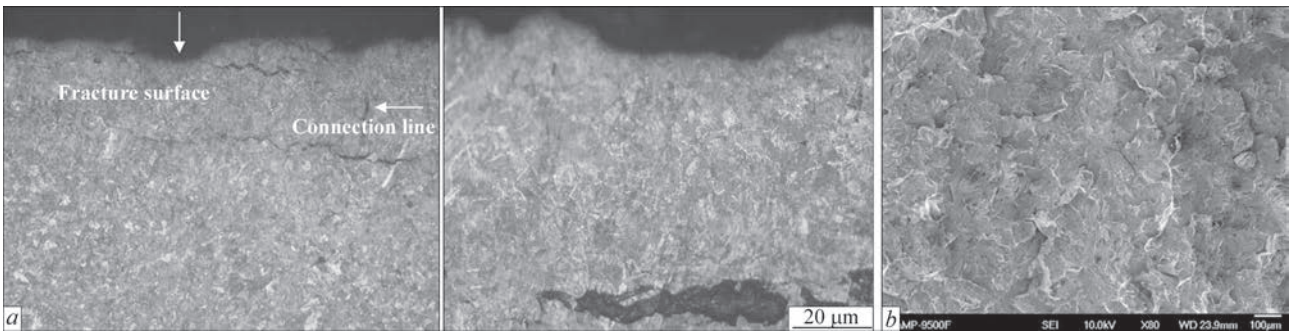

Figure 4. Microstructure of near-surface layer (*a*) and fracture surface (*b*)

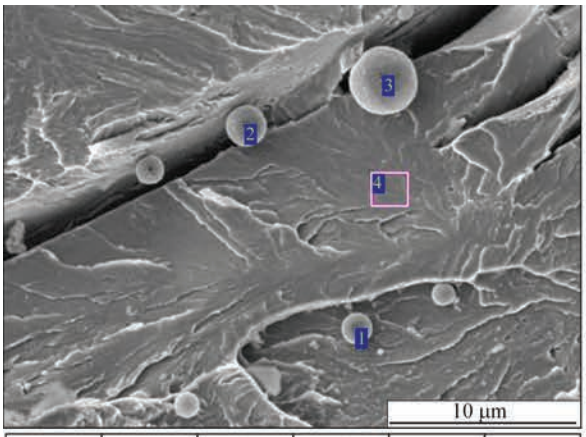

	C	O	Si	Mn	Fe
1	0.62	**28.07**	0.18	0.47	**70.66**
2	0.80	**27.63**	0	0.62	**70.95**
3	0.57	**28.07**	0.52	1.30	**69.55**
4	0.76	0.93	0.36	0.96	96.99

a

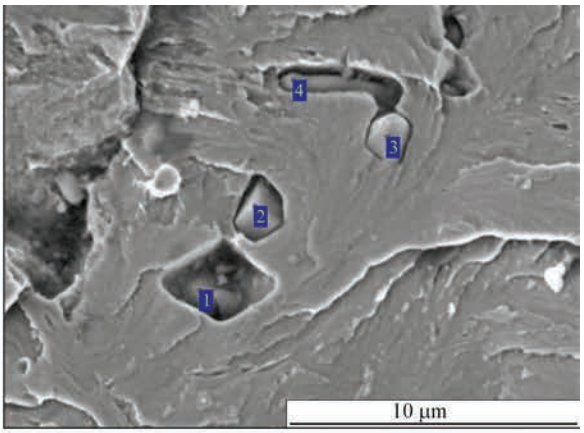

	C	O	Al	Si	S	Mn	Fe	Cu
1	11.05	8.09	0.32	1.56			78.97	
2	23.67	4.65		0.17	**31.11**	**32.75**	3.84	3.81
3	10.29			0	**41.72**	**39.44**	3.83	4.73
4	18.91	5.62		0.18	**30.70**	**32.47**	6.01	6.11

b

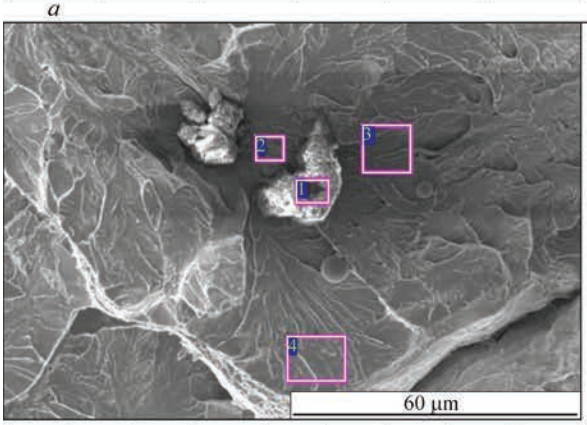

	C	O	Al	Si	S	Ti	Mn	Fe
1	**50.50**	**35.71**	0.61	0.47	0.54	**10.41**	0	1.66
2	18.63	8.41	0.20	0.52	0.18	0.59	0.60	69.77
3	9.37	1.49	0.13	0.63	0	0	0.67	87.39
4	8.22	2.62	0.11	0.74	0.06	0.13	0	87.88

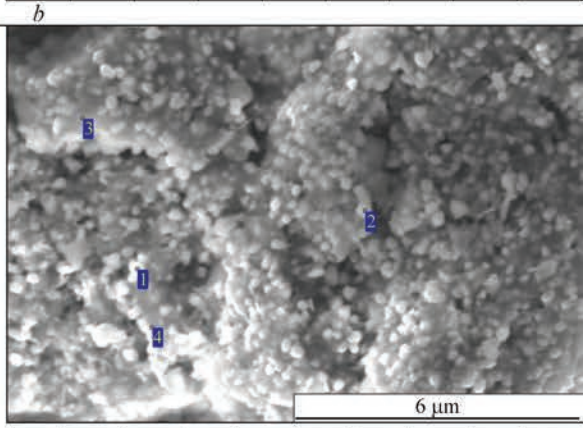

	C	O	Al	Si	S	Ca	Ti	Mn	Fe
1	**30.17**	**52.28**	0.29	0.45	0.15	0.29	**13.54**	0.14	2.54
2	**23.99**	**57.50**	0.78	0.33	0.13	0	**15.91**	0.12	1.23
3	**56.19**	**34.40**	0.33	0.42	0.88	0.14	**5.79**	0.05	1.54
4	**61.43**	**29.82**	0.45	0.72	0.33	0.01	**5.96**	0.07	1.09

c

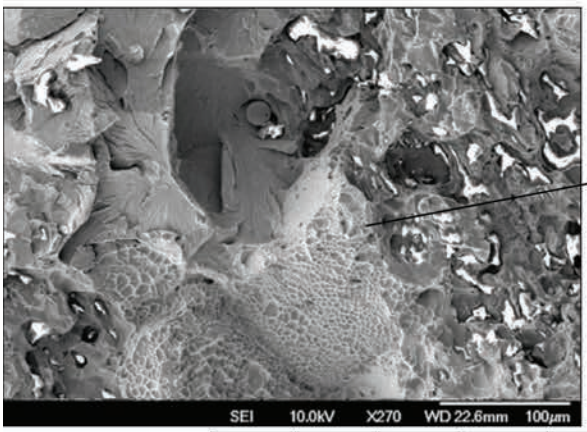

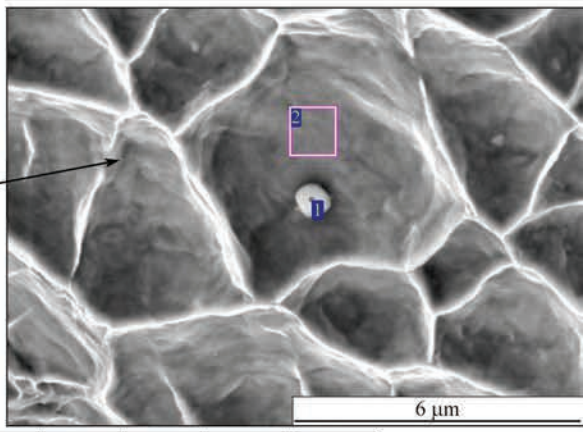

	C	O	Al	Si	S	Ti	Mn	Fe
1	19.24	**5.66**	0.42	0.24	**30.12**	0.67	**33.81**	**9.84**
2	5.67	1.28	0	0.59	0	0	1.04	**91.42**

d

Figure 5. Results of X-ray microanalysis of nonmetallic inclusions on the surface of crystalline fracture (at.%): *a* — iron oxides; *b* — manganese oxides; *c* — titanium carbon oxides; *d* — ferromanganese sulphides

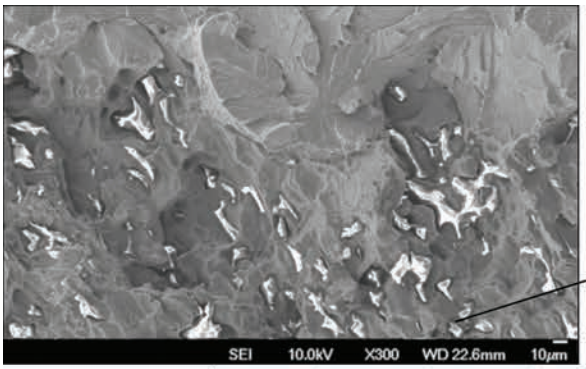

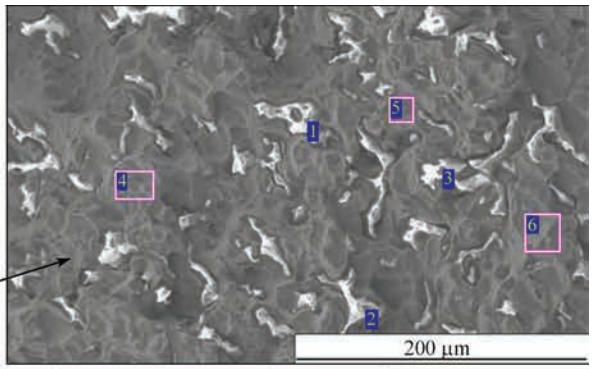

	C	O	Al	Si	Mn	Fe
1	3.27	**66.66**	**1.11**	**16.48**	**11.61**	0.86
2	3.36	**61.08**	**3.15**	**16.70**	**14.73**	0.99
3	2.41	**68.91**	**1.32**	**16.39**	**6.90**	0.90
4	4.43	1.57	0.11	0	0.80	93.09
5	5.51	0.86	0	0.18	0.81	90.76
6	4.70	1.50	0	0.15	1.11	92.54

a

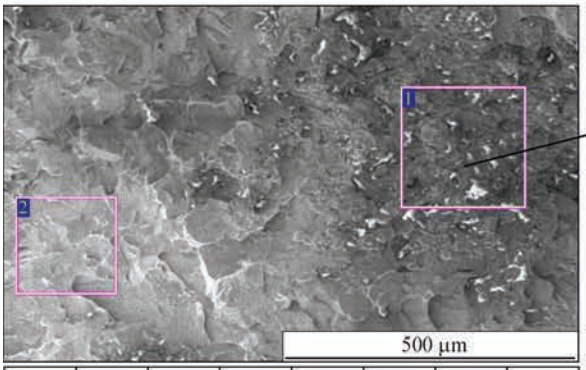

	C	O	Al	Si	Cr	Mn	Fe
1	14.43	21.93	0.11	5.76	0.34	5.47	51.96
2	7.01	1.63	0.05	0.41	0.34	1.45	89.11

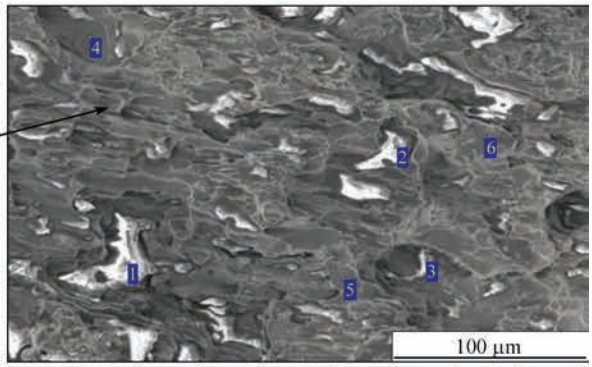

	C	O	Na	Al	Si	Cr	Mn	Fe
1	2.88	**66.74**	0	0	**18.05**	0	**10.32**	2.01
2	31.24	**50.68**	0.47	0.16	**10.67**	0.04	**5.85**	0.89
3	3.16	**59.39**	0.25	0.06	**18.88**	0.04	**15.63**	2.60
4	7.85	1.74	0	0	0.73	0	0.71	**88.97**
5	8.81	4.65	0	0.16	0.81	0.05	1.50	**84.02**
6	3.88	1.74	0.29	0	0.51	0	0.08	**93.51**

b

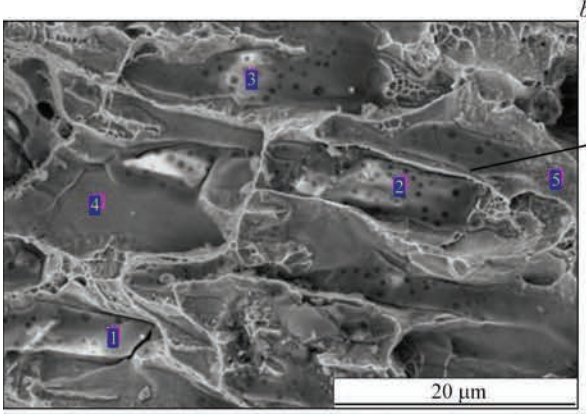

	C	O	Al	Si	S	Cr	Mn	Fe
1	1.72	**59.34**	0.16	**17.06**	0.33	0.27	**18.95**	2.17
2	1.85	**61.66**	0.21	**16.54**	0.20	0.05	**17.76**	1.75
3	1.96	**63.29**	0.04	**16.14**	0.05	0	**17.06**	1.46
4	1.28	0.98	0.05	0.20	0	0	1.23	96.27
5	11.57	17.56	0.31	3.96	0.36	0	5.84	60.40

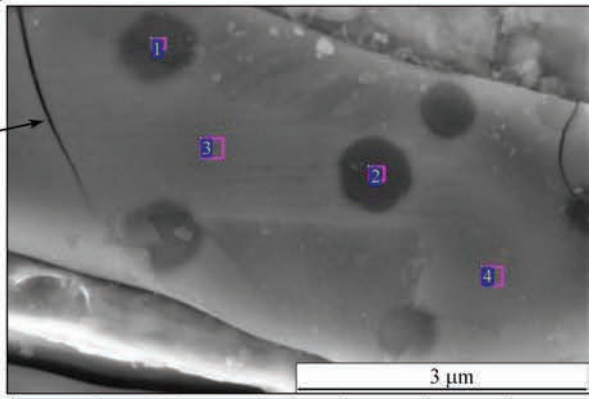

	C	O	Al	Si	Mn	Fe
1	1.99	51.28	0	**20.57**	1.81	24.35
2	2.10	62.25	0.06	**23.36**	3.49	8.74
3	0.68	58.26	0.22	**16.10**	21.05	3.69
4	1.91	59.21	0.11	**16.63**	18.96	3.17

c

Figure 6. Results of X-ray microanalysis of silicates of the near-contact layer of the rail joint (at.%): *a* — manganese aluminosilicates; *b*, *c* — manganese silicates

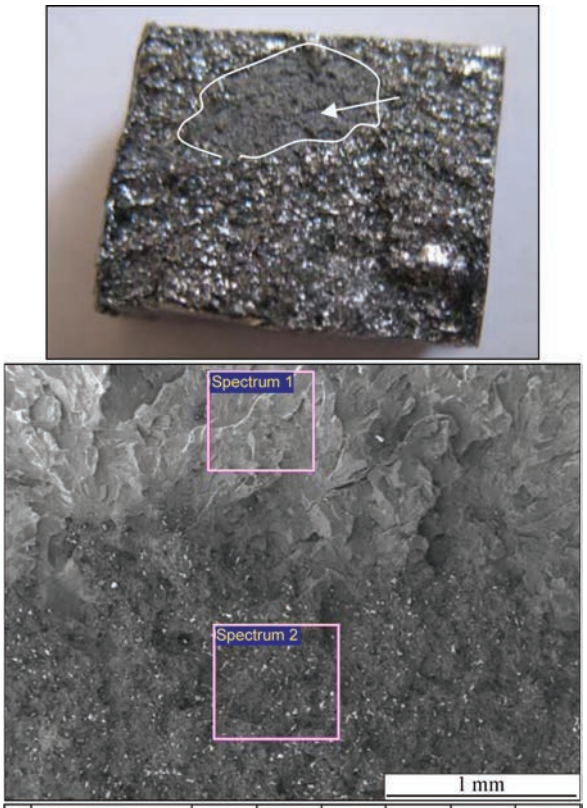

	Notes	C	O	Al	Si	Mn	Fe
1	Facets of spalling	8.34	2.74	0	0.25	0.13	88.55
2	Spot	7.01	16.52	0.45	4.08	5.86	66.08

Figure 7. "Matt spots" on the fracture surface of rail joints and results of X-ray microanalysis of surfaces from the area (at.%)

On the crystalline surface of the fracture, the microstructure represents facets of intragranular spalling with elements of plastic deformation: tongues, tear ridges (Figure 4, *b*). In the microstructure, tiny inclusions of manganese sulphide (Figure 5, *b*), globular inclusions of iron oxide (Figure 5, *a*), inclusions of oxides of alloying elements, in particular, titanium carbon oxides (Figure 5, *c*) are present. There, clusters of tiny sulphides (Figure 5, *c*) — fragmentation products of an easy fusible film (Fe, Mn)S are encountered, that is formed in the near-contact layer [3].

Along with the high-temperature oxides, on the fracture surface, flashed-type manganese silicates and alumosilicates of up to 30 μm in size (Figure 6, *a*, *b*) are observed. It is shown, that they have a cast structure (Figure 6, *c*). Unlike a layer of ferromanganese silicates on the lack of fusion surface, the content of iron in them is insignificant. The main crack during fracture passes at a distance of about 20–50 μm from the joint line (Figure 4, *a*). The transformation of nonmetallic inclusions, present on the surface of the crystalline fracture, apparently occurs in the layer of non-flashed metal. Considering that in the SiO_2–MnO system there are eutectics with a temperature of 1250 and 1315 °C [4], the formation of manganese silicates in the near-contact layer, apparently, occurs due to the diffusion interaction of surface-active manganese in iron with silica-containing oxides.

The inclusions of silicates often form clusters. Considering that opening of the rail metal during loading occurs along the weakened boundary of silicates with the matrix, as is seen in the fracture microstructure (Figure 6, *a*, *b*), the places of clusters of silicates in the normative documents are attributed to defects of welded joints that are classified as "matt spots" (Figure 7). Their appearance in the fracture microstructure is predetermined by the peculiar distribution of silicon oxide in the rail metal. Some amount of "matt spots" in the rail joints is acceptable. However, the total area should not be more than 15 mm^2 [10].

CONCLUSIONS

1. In welding of rails, high-temperature oxide inclusions, in addition to silicon oxide, transfer into a flashed layer and they are removed as a flash during upsetting without changing the aggregate state.

2. The existence of easy fusible eutectics with a temperature of 1178, 1117, 1250 and 1315 °C in the oxide SiO_2–FeO and MnO–FeO systems, respectively, as well as unlimited solubility in the MnO–FeO system is a prerequisite for the formation of manganese silicates on the surface of flashed rail ends during welding and in the near-contact layer of the joint.

3. Ferromanganese silicates on the flashed ends of the rails are formed as a result of the interaction of easy fusible iron oxide with the inclusions of silicon oxide and the subsequent diffusion of manganese from the rail metal. The welding technology involves the removal of ferromanganese silicates together with the melt as a flash during upsetting.

4. Manganese silicates in the near-contact layer of the joint are a product of diffusion interaction of surface-active manganese in iron with silica-containing oxide inclusions. Inclusions of manganese silicates often form clusters as a result of a nonuniform distribution of silicon oxides in the rail metal. Due to a weak adhesion to iron, the clusters of silicates affect the results of testing joints on impact toughness and static bending and are classified as defects of welded joints, the so-called "matt spots". Their total area is limited and should not exceed 15 mm^2 [10].

REFERENCES

1. Gubenko, S.I., Oshkaderov, S.P. (2016) *Nonmetallic inclusions in steel.* Kyiv, Naukova Dumka [in Russian].
2. Levchenko, N.V. (2006) Change of nonmetallic inclusions in manufacture of rails. *Metallurgicheskaya i Gornorudnaya Promyshlennost,* **2**, 63–65 [in Russian].
3. Kuchuk-Yatsenko, S.I., Didkovsky, A.V., Shvets, V.I. et al. (2016) Flash-butt welding of high-strength rails of nowadays

production. *The Paton Welding J.,* (**5–6**), 4–12. DOI: https://doi.org/10.15407/tpwj2016.06.01
4. Kuchuk-Yatsenko, S.I., Didkovsky, O.V., Bogorsky, M.V. et al. (2002) *Method of frash-butt welding.* Pat. 46820 Ukraine, Int. Cl. 6 B23K11/04, C2, Publ. 17.06.2002
5. Galakhov, F.Ya. (1991) *State diagrams of refractory oxide systems:* Refer. Book. Leningrad. Nauka [in Russian].
6. Kuchuk-Yatsenko, S., Shvets, V., Didkovsky, A. et al. (2016) Flash-butt welding of high-strength rails. Mining Informatics. *Automation and Electrical Engineering*, 528(**4**), 40–48.
7. Kuchuk-Yatsenko, S.I., Lebedev, V.K. (1976) *Flash-butt welding.* Kyiv, Naukova Dumka [in Russian].
8. Javojskij, V.I. (1969) *Theorie der Stahlerzeugung*. VEB Deutscerher Verlag fur Grundstoffindustrie. Leipzig.
9. Aksenova, K.V., Gromov, V.E., Ivanov, Yu.F. et al. (2017) Carbon redistribution under deformation of steels with bainite and martensite structures. *Izvestiya. Ferrous Metallurgy*, 60(**7**), 544–548 [in Russian]. DOI: https://doi.org/10.17073/0368-0797-2017-7-544-548.
10. TUU 24.1-40075815-002:2016: *New welded rails for railways* [in Ukrainian].

ORCID
V.I. Shvets: 0000-0003-4653-7453,
I.V. Ziakhor: 0000-0001-7780-0688,
L.M. Kapitanchuk: 0000-0002-8624-2590

CONFLICT OF INTEREST
The Authors declare no conflict of interest

CORRESPONDING AUTHOR
I.V. Ziakhor
E.O. Paton Electric Welding Institute of the NASU
11 Kazymyr Malevych Str., 03150, Kyiv, Ukraine.
E-mail: zyakhor2@ukr.net

SUGGESTED CITATION
V.I. Shvets, I.V. Ziakhor, L.M. Kapitanchuk (2023) Features of formation and transformation of oxides in flash-butt welding of K76F rails. *The Paton Welding J.*, **7**, 16–24.

JOURNAL HOME PAGE
https://patonpublishinghouse.com/eng/journals/tpwj

Received: 22.05.2023
Accepted: 06.09.2023

DOI: https://doi.org/10.37434/tpwj2023.07.03

USE OF LASER WELDING AND SURFACING TECHNOLOGIES FOR REPAIR AND MANUFACTURE OF THIN-WALLED WELDED JOINTS OF HIGH-ALLOY STEELS

A.V. Bernatskyi, O.V. Siora, V.I. Bondareva, N.O. Shamsutdinova, Yu.V. Yurchenko

E.O. Paton Electric Welding Institute of the NASU
11 Kazymyr Malevych Str., 03150, Kyiv, Ukraine

ABSTRACT

Thin-walled welded joints of corrosion-resistant high-alloy steels are used in various industries for the manufacture of critical structures. The tendency to reduction in the mass of products in order to save costs and energy resources makes it relevant to find the ways to solve the problem of welding such joints, including also the use of concentrated power sources such as laser radiation. The use of laser technologies in welding thin-walled joints of high-alloy steels may be applied not only at the manufacturing stage but also at the stage of repair. The high cost of treatment of such materials makes the problem of finding the ways to avoid the formation of defects in such welded joints relevant. At the same time, it is urgent to develop technologies for repair of thin-walled welded joints made of high-alloy steels. The article is devoted to the solution of this task namely by using laser welding and surfacing technologies. According to the results of visual, radiographic testing and metallographic examinations, the parameters of thin-walled welded T-joints of AISI 321 steel were evaluated, namely: geometry, ripple, presence of craters, pores, their quantity, sizes, mutual position and other parameters provided by DSTU EN ISO 13919-1:2015 standard. The analysis of the obtained data made it possible to find the presence of individual defects of welded T-joints in the form of single pores, chain of pores, lacks of fusion, depression of the weld, lacks of penetration, shrinkage cavities and cavities in the crater, undercuts, excess of convexity. The procedure for their elimination and prevention of their formation was developed. It was established that thin-walled welded T-joints of AISI 321 steel after repair according to the proposed procedure have mechanical characteristics at the level of defect-free welded joints and amount to 670–717 MPa. This allows recommending the proposed procedure to perform the operation of repair of such joints when eliminating defects in the form of burn-outs.

KEYWORDS: laser welding, high-alloy steels, welded T-joints, repair, procedures of defects elimination, critical structures

INTRODUCTION

In many industries, structures of corrosion-resistant high-alloy steels of small thickness (0.1–2.0 mm) are widely used [1–3]. Butt, T-joint and fillet welded joints of thin metal are used by developers and manufacturers of all kinds of devices for delivery, redistribution of flows, measurement of pressure and flow rate of liquids and gases used in the nuclear industry, automotive industry and rocket construction [4–6]. Their specific requirements are specified to the aim and conditions of service of these products. Quite often, a welded joint should not only have a sufficient strength, but also be sealed. The operation in an aggressive environment at high temperatures requires an increased corrosion resistance. In addition, these products should have an increased reliability. This is caused by the fact that they are usually used in critical assemblies, which, first of all, applies to aviation, space and nuclear power engineering [7–9].

Welded joints of such parts may be produced using different welding methods. The main among them are argon-arc [6], microplasma, contact-roller, electron beam and laser welding [10–12]. The latter refers to the most acceptable methods to solve the tasks of producing small thickness joints. Laser welding does not require vacuum chambers as electron beam welding, it allows producing narrower welds compared to arc methods, allows carrying out precision adjustment of technological parameters, it is distinguished by a high stability and allows receiving satisfactory service characteristics of the weld during welding of thin metal.

However, when producing welded joints of thin-sheet steels, certain technical problems arise. In the case of excessive heat input, that occurs while welding thin-walled parts or producing sufficiently wide welds, residual deformations of welded structures arise [11]. This is especially clear when welding austenitic corrosion-resistant steels, that have a low thermal conductivity and a high linear expansion ratio [1, 3, 7]. This enhances the curvature and deformation of edges of thin-walled parts during welding. As a result, the gaps between the welded surfaces increase, and, as a consequence, in welding, defects in the form of burn-outs, lacks of fusion, lacks of penetration arise and the geometry of the welded joint becomes unstable.

A high cost of treatment of such materials makes the problem of finding the ways to avoid the formation of defects in such welded joints relevant. At the same time, the urgent problem is to develop technologies for repairing thin-walled welded joints of high-alloy

Table 1. Chemical composition of AISI 321 steel, wt.%

Grade of steel	C	Si	Mn	Ni	S	P	Cr	Ti	Fe
AISI 321	< 0.1	< 0.8	1–2	10–11	< 0.2	< 0.035	17–19	< 0.6	Base

steels. The article is devoted to the solution of this task namely by using laser welding and surfacing technologies.

MATERIAL AND PROCEDURES OF RESEARCH

The research material (Table 1) was high-alloy AISI 321 steel. The specimens were made from a sheet of 1.2 mm thickness. The size of the billet of a T-joint stiffener is 320×100 mm; the size of the billet of a T-joint flange is 300×200 mm.

OPTIMIZATION MODE OF REPAIRING WELDED JOINTS

Laser welding of welded T-joints of AISI 321 steel with the thickness of the flange and stiffener of 1.2 mm was performed "uphill" in a vertical position in a one pass with a slot weld in a pulsed mode of laser radiation generation in the laboratory bench, shown in Figure 1.

The parameters of welding modes were as follows: maximum laser radiation power P_{max} = 4.4 kW; average laser radiation power P_{av} = 3.2 kW; pulse duration T = 75 %; frequency of passing laser radiation pulses is 250 Hz; focal length of the lens F = 300 mm; lifting of laser radiation focus over the welded surface ΔF = +2 mm; welding speed V_w = 4000 mm/min. The choice of this mode is predetermined by the most stable formation on both sides of fillets between the flange and stiffener of the T-joint, while providing the required geometry of the welded joint and a high level of mechanical characteristics.

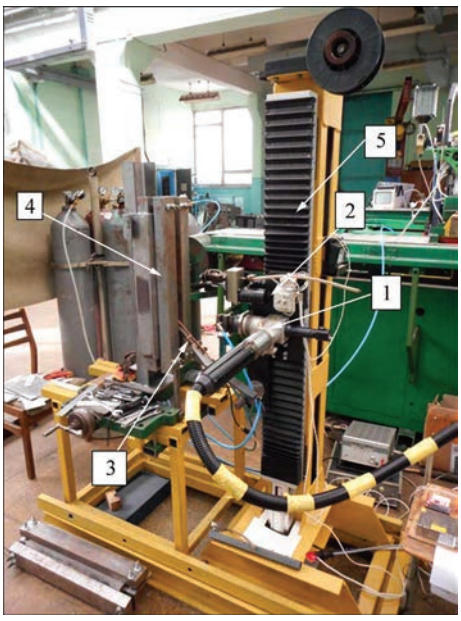

Figure 1. Part of the laboratory bench for optimization technological techniques of laser welding in a vertical spatial position: 1 — head for laser welding; 2 — manipulator carriage; 3 — gas shielding; 4 — clamp; 5 — manipulator beam (Z axis)

Typical defects of welded joints are normalized by DSTU EN ISO 13919-1:2015 standards "Welding. Joints made by electron beam and laser welding. Guidelines on quality level assessment depending on defects. Part 1. Steel" and DSTU EN ISO 6520-1:2015 "Welding and related processes. Classification of geometric defects in metal materials. Part 1. Fusion welding". According to these standards, three levels of joint quality are recommended: moderate "D", average "C" and high "B".

According to the results of visual and radiographic testing, the parameters of thin-walled welded joints of AISI 321 steel were evaluated, namely: geometry, ripple, presence of craters, pores; their quantity, sizes, mutual position and other parameters provided by DSTU EN ISO 13919-1:2015 standard.

The evaluation of the obtained data made it possible to establish the probability of forming individual defects in welded T-joints, namely, single pores, chain of pores, lacks of fusion, depression of the weld, lacks of penetration, shrinkage cavities and cavities in the crater, undercuts, excess of convexity. The procedure of their elimination and prevention of their formation was developed, which has the following content:

- to eliminate defects in the form of pores, chain of pores, lacks of fusion, depression of the weld, lacks of penetration – rewelding of the weld with the addition of filler material (if necessary);
- to prevent the formation of shrinkage cavities and cavities in the crater — run off tabs; software control of smooth growth of laser radiation power at the beginning of welding and smooth drop at the end of welding were used;
- to eliminate undercuts, excess of convexity — additional remelting with a defocused beam was performed.

The studies on consideration of options for repair of defects in the form of burn-outs (melt-through) and cracks were conducted. The options of using filler materials in the form of powder and a thin strip are considered. During repair, as a filler material, a strip of 0.25 mm thick of AISI 321 steel and a surfacing powder with a fraction "150 + 53" of grade "16316" produced by the Castolin Eutectic Company with the following chemical composition, %: Fe — base; 0.03 C; 17.5 Cr; 13 Ni; 2.7 Mo were used.

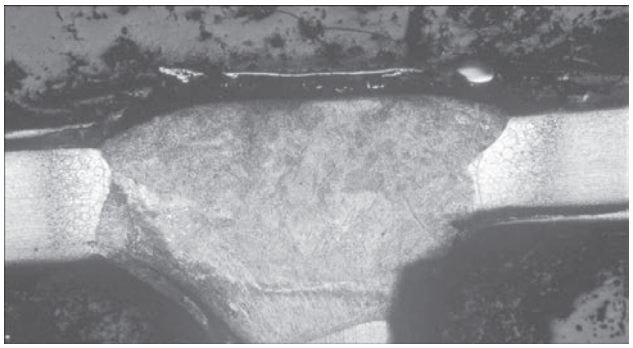

Figure 2. General appearance of welded T-joint after repair welding (×25)

Below, the procedure of repair treatment on the example of eliminating a defect in the form of a burn-out in the T-joint was considered. Defective areas of the specimen were subjected to repair.

As a result of the carried out works, it was established that at the presence of defective areas with burn-outs at the welding area, welded joints should be repaired by the following procedure, namely (the given data for repairing the defect of 1.5×1.5 mm, as for such that is most often encountered in visual testing of produced welded joints):

- mechanical treatment (cleaning) of repair place;
- cleaning with acetone immediately before repair;
- putting of repair patch of AISI 321 steel (δ = = 0.25 mm thick) with an area by 30–50 % larger than a defect area;
- laser repair spot welding on the mode: laser radiation defocusing ΔF = 30 mm, laser radiation power P = 1 kW, exposure time is 0.5 s;
- mechanical treatment (cleaning) of the repair place after welding;
- cleaning with acetone immediately before the next operation of repair;
- applying the required volume of filler material in the form of powder (powder with "150 + 53" fraction of 16316 grade, produced by the Castolin Eutectic Company is used; it is admitted to use the analogue of powder close to the base material as to its composition and properties);
- performance of repair surfacing for elimination of the weld depression (formation of a sufficient reinforcement of the upper bead) on the mode: laser radiation defocusing ΔF = +30 mm, laser radiation power P = 1 kW, exposure time is 0.5 s.

Performance of repair operation according to the abovementioned procedure allows: eliminating discontinuities in welded T-joints; forming fillets on both sides of a stiffener in the T-joints; forming the required reinforcement of the upper weld bead.

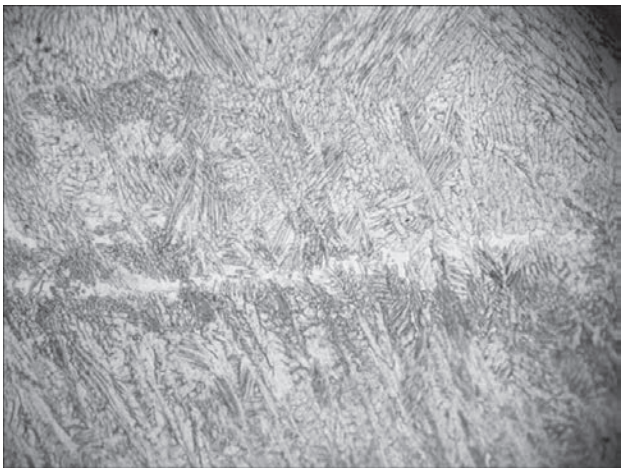

Figure 3. Fusion line of weld metal of T-joint after repair welding (×200)

METALLOGRAPHIC EXAMINATIONS OF PRODUCED WELDED JOINTS AFTER REPAIR

The structure in the welded T-joint after the repair was examined according to the abovementioned sequence of operations. From the repaired T-joint with a rewelded defect in the form of a burn-out, a template was cut out, which was fixed in a metal frame by filling latacryl. After mechanical treatment (grinding and polishing), the specimen was studied by the methods of optical microscopy and microdurometric analysis.

The studied joint represents a T-joint, consisting of a stiffener and a flange (Figure 2).

The cast structure of the weld is almost uniform throughout the whole area of the joint both in the base weld, as well as in the repaired part (Figures 3 and 4).

At the boundary of the weld of repair welding, a zone was revealed, that was still bright after etching having a hardness in the upper part $HV1$ — 3090–3510 MPa, and on the side of the flange — $HV1$ — 4010–4210 MPa. Whereas the hardness of the repair welding metal is on average $HV1$ —

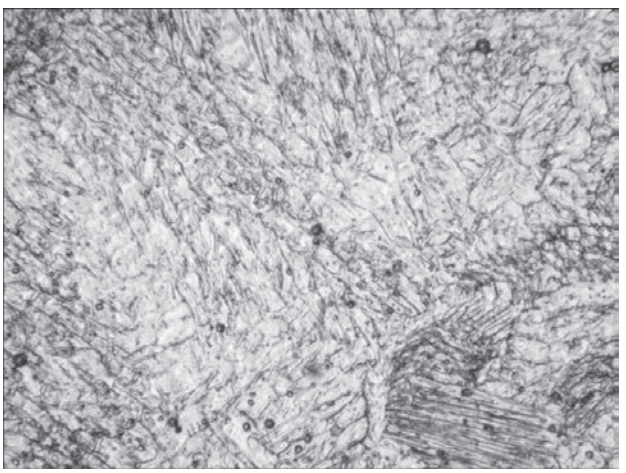

Figure 4. Microstructure (×500) of cast weld metal in the T-joint with repair welding, general appearance

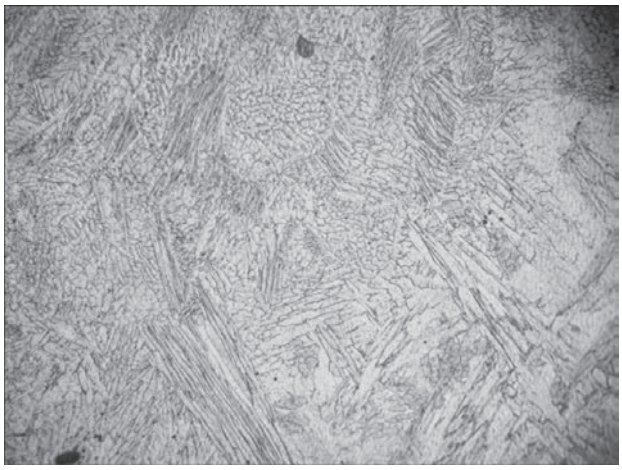

Figure 5. Microstructure (×200) of repair welding metal

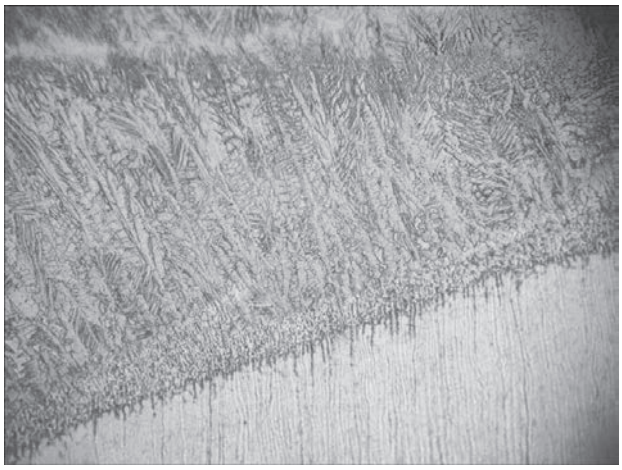

Figure 6. Microstructure (×200) of initial weld and HAZ metal in the stiffener of welded T-joint after repair welding

3510–3830 MPa with separate areas where it is reduced to *HV*1 — 3140–3362 MPa and increased to *HV*1 — 4010 MPa.

The structure of the base weld and the weld after repair welding is austenitic with δ-ferrite, probably contains martensite (Figures 5 and 6).

The presence of martensite is evidenced by an increased hardness and the presence of relief in the body of crystallites (Figure 7). This assumption requires verification by local research methods.

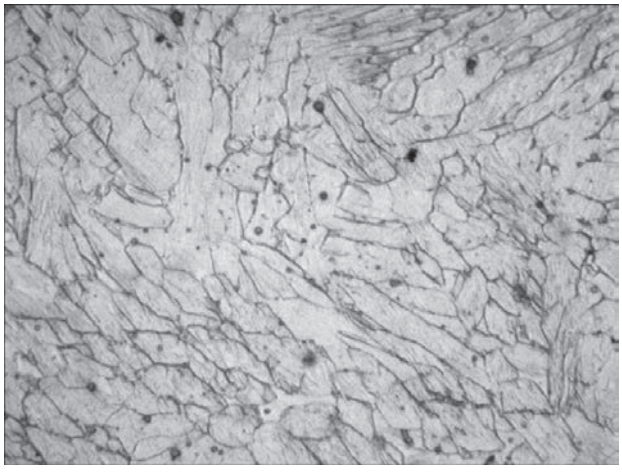

Figure 7. Microstructure (×1000) of repair welding metal (relief)

Figure 8. Microstructure (×500) of initial weld and HAZ metal in the stiffener of welded T-joint after repair welding

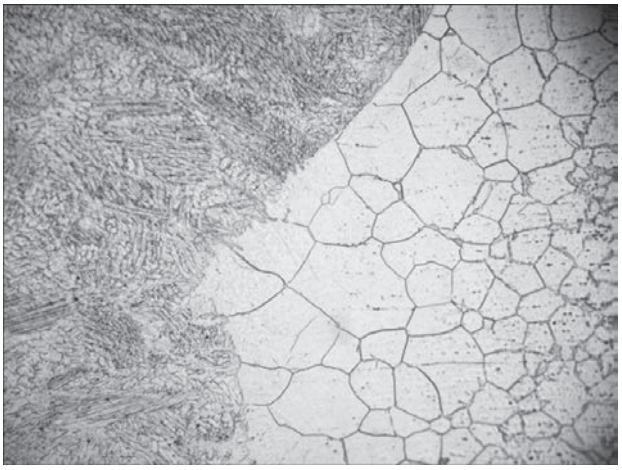

Figure 9. Microstructure (×200) of HAZ metal and fusion line with the flange of welded T-joint after repair welding

The structure of the weld near the fusion line with the stiffener is smaller compared to the rest of the weld (Figure 8) and represents austenite and δ-ferrite, the width of this area is ~ 100 μm. The hardness here

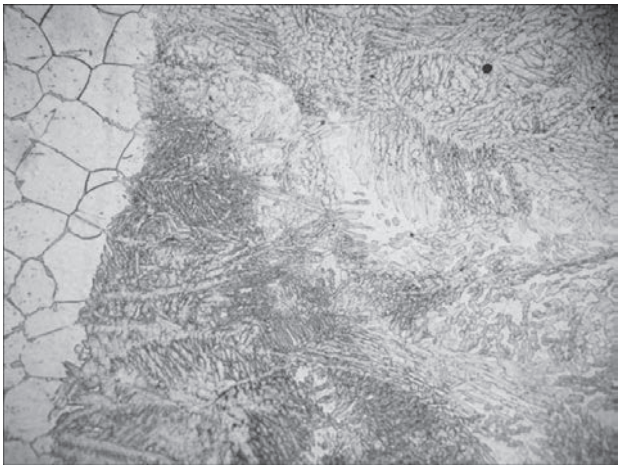

Figure 10. Microstructure (×200) of weld and HAZ metal of the flange of welded T-joint after repair welding

Table 2. Results of tests of specimens on static tension with repaired spot defects

Number	Width, mm	Thickness, mm	σ_t, MPa	Fracture place
1	25.3	1.2/1.2	717	Fracture along BM
2	25.5		670	Fracture along weld
3	25.2		684	
4	25.1		672	Fracture along BM
5	24.9		694	
6	25.3		715	

is slightly lower than in other areas of the weld — *HV*1 — 2740 MPa.

The structure of HAZ of the stiffener metal represents austenite and δ-ferrite. The size of the austenite grain in HAZ did not change compared to the base metal (Figure 8). At a distance of up to 50 μm from the fusion line, the amount of δ-ferrite increased. The hardness in this area is *HV*1 — 2450 MPa.

The structure of HAZ of the flange also consists of austenite and δ-ferrite (Figure 9), but differs by a coarser grain of austenite — grain size No. 4.5 (GOST 5639–82). At the boundary of the grains of austenite (Figure 10), δ-ferrite is precipitated, the width of the overheating area of a coarse grain is ~ 400 μm. HAZ hardness in the overheating area is *HV*1 — 2740–3090 MPa.

After repair welding, no defects in the areas of base and repair welds and HAZ were detected. The structure of the base metal is two-phase austenitic-ferritic. Along the direction of rolling, δ-ferrite is precipitated, the hardness is *HV*1 — 2060–2580 MPa.

MECHANICAL TESTS OF SPECIMENS OF WELDED T-JOINTS AFTER REPAIR ON STATIC TENSION

The tests of welded specimens on static tension were performed after repair. The tests were performed on the specimens of T-joints in a quantity of 6 pieces cut out from different tested joints. To simulate defects in the form of burn-outs, drills (from 1 to 3 pieces at a length of 20 mm) were performed in the specimens prepared for tests on static tension. Defects simulated in such a way were repaired by the spot powder laser surfacing (Figure 11).

The results of testing the specimens with repaired spot defects on static tension are given in Table 2.

According to the results of carried out tests of the specimens with repaired spot defects on static tension, the values of the tensile strength σ_t for all the tested repaired welded joints are not lower than the indices obtained for the base welded joints without repair and the base material of the specimens (tensile strength σ_t of the base welded joints is 665–712 MPa; tensile strength σ_t of the base material of the specimens is

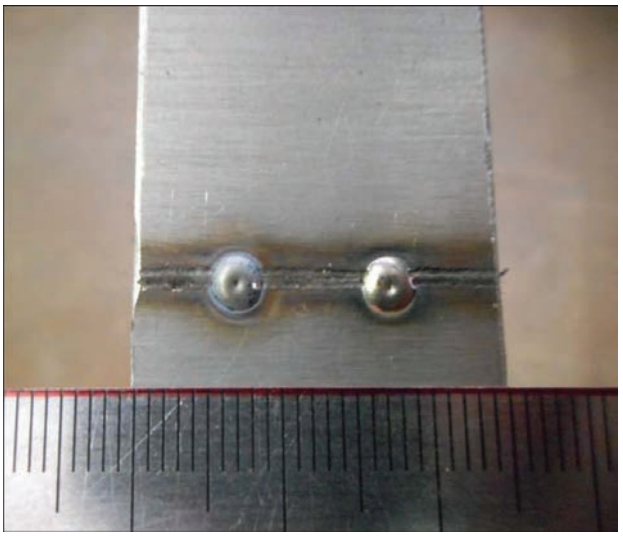

Figure 11. Photo of specimen for tests on static tension with repaired two spot defects

685–725 MPa). These results allow suggesting that mechanical properties of welded joints produced after repair by the proposed procedure meet the standards DSTU EN ISO 13919-1:2015 and DSTU EN ISO 6520-1:2015, specified to welded joints produced by fusion welding.

CONCLUSIONS

According to the results of visual, radiographic testing and metallographic examinations, the parameters of thin-walled welded T-joints of AISI 321 steel were evaluated, namely: geometry, ripple, presence of craters, pores; their quantity, sizes, mutual position and other parameters provided by DSTU EN ISO 139191:2015 standard. The analysis of the obtained data made it possible to establish the presence of individual defects of welded T-joints in the form of single pores, chain of pores, lacks of fusion, depression of the weld, lacks of penetration, shrinkage cavities and cavities in the crater, undercuts and excess of the convexity. The procedure for their elimination and prevention of their formation was developed.

It was established that thin-walled welded T-joints of AISI 321 steel after repair by the proposed procedure have mechanical characteristics at the level of defect-free welded joints and amount to 670–717 MPa. This allows recommending the proposed procedure to perform the operation of repairing such joints while eliminating defects in the form of burn-outs.

REFERENCES

1. Soltani, H. M., Tayebi, M. (2018) Comparative study of AISI 304L to AISI 316L stainless steels joints by TIG and Nd: YAG laser welding. *J. of Alloys and Compounds*, **767**, 112–121. DOI: https://doi.org/10.1016/j.jallcom.2018.06.302
2. Ramakrishna R, V.S.M., Amrutha, P.H.S.L.R., Rahman Rashid, R.A., Palanisamy, S. (2020) Narrow gap laser welding (NGLW) of structural steels — a technological review and

future research recommendations. *The Inter. J. of Advanced Manufacturing Technology*, **111**, 2277–2300. DOI: https://doi.org/10.1007/s00170-020-06230-9
3. Khokhlov, M., Bernatskyi, A., Berdnikova, O. et al. (2022) Optimization of T-Joints laser robotic welding procedure parameters from AISI 321 stainless steel. In: *Proc. of Smart Technologies in Urban Engineering* (*STUE-2022)*, 513–524. Cham, Springer International Publishing. DOI: https://doi.org/10.1007/978-3-031-20141-7_47
4. Khaskin, V.Yu., Korzhyk, V.M., Dong, C., Illyashenko, E.V. (2020) Improvement of the effectiveness of laser welding processes by reciprocating movement of the focus. *The Paton Welding J.*, **1**, 54–60. DOI: https://doi.org/10.37434/tpwj2020.01.08
5. Bernatskyi, A., Sydorets, V., Berdnikova, O. et al. (2021) Research of technology for repair of heat exchangers of nuclear power plants by laser welding. *Solid State Phenomena*, **313**, 94–105. DOI: https://doi.org/10.4028/www.scientific.net/SSP.313.94
6. Bernatskyi, A., Goncharov, P., Sokolovskyi, M. et al. (2023) Spot welded joints of steels produced by electric arc and laser welding in different spatial positions. In: *Proc. of Advances in Mechanical and Power Engineering (AMPE 2021)*, 198–207. Cham, Springer International Publishing. DOI: https://doi.org/10.1007/978-3-031-18487-1_20
7. Krivtsun, I.V., Korzhik, V.N., Khaskin, V.Y. et al. (2019) Hybrid laser-microplasma welding of stainless steels. *The Paton Welding J.*, **12**, 31–36. DOI: https://doi.org/10.15407/tpwj2019.12.04
8. Wang, L., Gao, X., Kong, F. (2022) Keyhole dynamic status and spatter behavior during welding of stainless steel with adjustable-ring mode laser beam. *J. of Manufacturing Processes*, **74**, 201–219. DOI: https://doi.org/10.1016/j.jmapro.2021.12.011
9. Das Banik, S., Kumar, S., Singh, P. K., Bhattacharya, S. (2023) Influence of weld repair on the residual stresses induced in austenitic stainless steel weld joints. *Production Engineering*, 17(**1**), 81–94. DOI: https://doi.org/10.1007/s11740-022-01156-5
10. Chen, Z., Sun, W., Huang, Y. et al. (2022) The effect of laser energy density on microstructural evolution and mechanical properties of laser clad 316L stainless steel for repair. *Surface and Coatings Technology*, **448**, 128899. DOI: https://doi.org/10.1016/j.surfcoat.2022.128899
11. Zhu, J., Li, L., Li, D. et al. (2022) Microstructural evolution and mechanical properties of laser repaired 12Cr12Mo stainless steel. *Materials Sci. and Eng.: A*, **830**, 142292. DOI: https://doi.org/10.1016/j.msea.2021.142292
12. Sheikhbahaee, H., Mirahmadi, S.J., Pakmanesh, M.R., Asghari, S. (2022) Investigating sensitivity to process parameters in pulsed laser micro-welding of stainless steel foils. *Optics & Laser Technology*, 148, 107737. DOI: https://doi.org/10.1016/j.optlastec.2021.107737

ORCID
A.V. Bernatskyi: 0000-0002-8050-5580,
O.V. Siora: 0000-0003-1927-790X,
V.I. Bondareva: 0000-0002-4745-0995,
N.O. Shamsutdinova: 0000-0002-3525-0080,
Yu.V. Yurchenko: 0000-0001-9253-009X

CONFLICT OF INTEREST
The Authors declare no conflict of interest

CORRESPONDING AUTHOR
A.V. Bernatskyi
E.O. Paton Electric Welding Institute of the NASU
11 Kazymyr Malevych Str., 03150, Kyiv, Ukraine.
E-mail: avb77@ukr.net

SUGGESTED CITATION
A.V. Bernatskyi, O.V. Siora, V.I. Bondareva, N.O. Shamsutdinova, Yu.V. Yurchenko (2023) Use of laser welding and surfacing technologies for repair and manufacture of thin-walled welded joints of high-alloy steels. *The Paton Welding J.*, **7**, 25–30.

JOURNAL HOME PAGE
https://patonpublishinghouse.com/eng/journals/tpwj

Received: 21.06.2023
Accepted: 06.09.2023

DOI: https://doi.org/10.37434/tpwj2023.07.04

INFLUENCE OF ELECTRON BEAM FOCUSING CURRENT ON GEOMETRY AND MICROSTRUCTURE OF WELDED JOINTS OF ALUMINIUM 2219 ALLOY

M.O. Rusynyk[1], V.M. Nesterenkov[1], M. Sahul[2], I.M. Klochkov[1]

[1]E.O. Paton Electric Welding Institute of the NASU
11 Kazymyr Malevych Str., 031 %0, Kyiv, Ukraine
[2]Czech Technical University in Prague, Faculty of Mechanical Engineering
Technicka 4, 160 00 Prague 6, Czech Republic

ABSTRACT

The influence of the focusing current of electron beam welding on the nature of the formation of welded joints of aluminium 2219 alloy was investigated. It was established that when the focusing current increases, the width of the face weld grows. And the width of the weld root depends on the real position of the electron beam focus relative to a sharp focus on the metal surface (639 mA). Dependence of the focusing current on the distribution of copper and aluminium in the weld metal was revealed. An increase in the focusing current from 629 to 649 mA led to an increase in the copper content in the interdendritic regions. Energy dispersion X-ray analysis showed that the microstructure of the welded joint produced at the focusing current of 629 mA, consists of equiaxial dendrites with embedded small particles, pores and α+θ-Al_2Cu eutectic, separated in the interdendritic regions.

KEYWORDS: electron beam welding, assembly and welding equipment, aluminium alloy, energy dispersive X-ray spectroscopy, segregation

INTRODUCTION

Aluminium 2219 alloy is a high-strength alloy consisting of aluminium, copper and manganese, which combines good treatment ability and qualitative mechanical properties. Products of this alloy can be used in the temperature range from –270 to 300 °C. At the same time, the alloy has higher mechanical properties compared to wrought alloys of the Al–Mg alloying system [1]. This alloy is a light metallic material with several desirable properties: low density, high specific strength and rigidity. Therefore, it is widely used in automotive, aircraft, aerospace and other industries that require lightweight structures [2]. The use of 2219 alloy became particularly widespread in the aerospace industry, namely, in the manufacture of rocket bodies, fuel tanks, chassis elements and other structural assemblies.

In welding alloys of the Al–Cu–Mg system, difficulties are caused by a great susceptibility of the weld metal to the formation of pores and crystallization cracks (especially typical for alloys based on aluminium). In welding alloys of an increased strength, cold cracking is observed. A significant shrinkage during weld crystallization, as well as high linear expansion coefficient lead to considerable residual deformations. In welding of hardened aluminium and thermally strengthened aluminium alloys, the strength of the welded joint is reduced compared to the strength of the base metal, which creates certain problems. Significant difficulties arise as a result of light oxidation of aluminium in solid and molten states. The formed refractory film of aluminium Al_2O_3 oxide hinders the weld formation and it is a source of nonmetallic inclusions in the weld metal.

Electron beam welding (EBW) compared to other types of welding these types of alloys has several advantages. The welding process runs in vacuum, which is important for chemically active alloys. It is also featured by a quick process of heating and cooling of the metal, which in turn determines the minimal softening of welded joints, and the maximum level of their strength properties. Temporary inner stresses do not have time to affect the solidified metal, i.e., crystallization cracks have no time to arise. For high-strength aluminium alloys, it is possible to avoid metal softening in the near-weld zone at high welding speeds that provide minimal thermal influence on the base metal [3]. The use of EBW allowed reducing the volume of molten metal of the weld pool and dimensions of the heat-affected zone (HAZ) and this led to a decrease in the rate of growth of elastic-plastic deformations in the temperature range of brittleness and an increase in the margin of technological strength of material to be welded [4, 5].

To produce welded joints with the required properties, it is necessary to optimize EBW parameters. The focusing current is one of the main EBW parameters, which affects the focus position and, thus, the total power density created by the electron beam on

Table 1. Chemical composition of plates of 2219 alloy, wt.%

Al	Cu	Mn	V	Fe	Si	Zn	Zr	Ti
Base	6.23	0.32	0.09	0.13	0.28	0.03	0.1	0.07

the surface of the materials to be welded. Until now, there is no information on the study of the influence of the focusing current on the microstructure and the mechanical properties of AA2219 alloy welded by electron beam. Only individual authors investigated the influence of the focus position and the angle of incidence of the beam on the behaviour of the molten pool in the welding AA2219 alloy. It was found that the smallest porosity in the welds of AA2219 alloy was observed when the focus was applied by 8 mm lower than the surface of the metal to be welded [6]. At the moment, other results of studying the alloy, considered in the work, are unknown. The studies and obtained results are unique and contribute to explaining the influence of the focusing current on the geometry and microstructure of welded joints of aluminium 2219 alloy.

The aim of this work is to investigate the effect of the EBW focusing current on the geometry and microstructure of welded joints of aluminium 2219 alloy at a constant input energy of welding and accelerating voltage.

PROCEDURE OF WORK PERFORMANCE

For the study, the plates of aluminium 2219 alloy of 10 mm thickness were used.

The chemical composition of the base material of aluminium 2219 alloy was measured using the X-ray fluorescence spectroscopy. For measurements, the portable X-ray Delta line analyzer of the Innov-X Company was used. The chemical composition was measured in three different places and average values were calculated. XRF results are given in Table 1. A small amount of zirconium (0.1 wt.%) causes a change in grain, namely, reduces the grain size of the alloy.

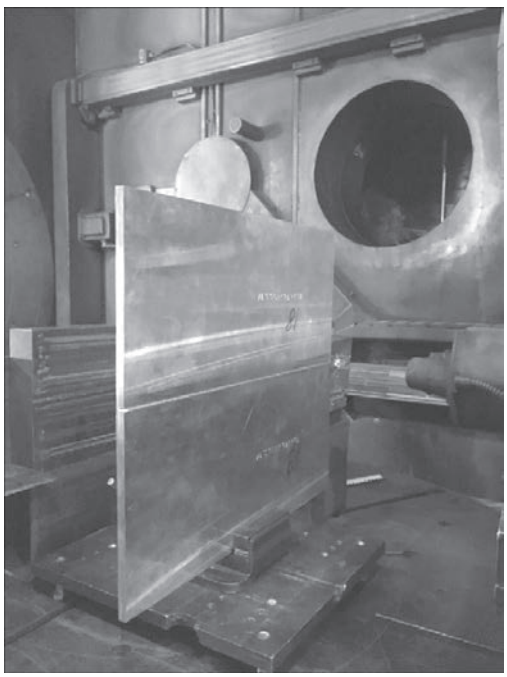

Figure 1. Scheme of EBW using horizontal beam in a horizontal plane

The point EDS analysis of a local chemical composition was performed in an equiaxial zone near the penetration boundary for welded joints produced during focusing currents of 629 and 649 mA.

The chemical composition was analyzed using the energy dispersive X-ray spectroscopy method (EDS): JEOL 7600F SEM FEG with X-max 50 mm^2 analyzer of the Oxford Instruments Company.

The welding process took place in an electron beam welding installation of UL-209M type.

The configuration of the installation involves a movable intrachamber welding gun with a computer numerical control (CNC) for movement of a cantilever type. This mechanism provides a linear movement along the three Cartesian coordinate axes (along the chamber — *X*, across — *Y* and vertical — *Z*), as well as the inclination of the gun at an angle of 90° in the *Z–X* plane (from the "vertical" position of the gun to the "horizontal"). In this case, this "inclination" is performed by rotating the entire cantilever beam, which is the base of the mechanism for movement along the *Y* axis. The beam itself can move freely in the *Z–X* plane within most dimensions of the welding chamber.

The welding gun unit can have an additional degree of freedom — rotation axis of the gun in a plane parallel to the *Y* axis — usually at ± 45° (i.e., axis of this rotation is perpendicular to the *Y* axis).

The installations of this type are completed with a high-voltage welding source with a capacity of 15 %, 30 or 60 kW (at an accelerating voltage of 60 kV) depending on the specific materials to be welded and their thickness.

For welding of plates of different sizes, assembly and welding equipment was developed, in which a batch of butt joints with a through penetration at different welding parameters was welded.

It is known that due to a high thermal conductivity of aluminium, special requirements are specified to the types of welded joints. The uniform weld formation is achieved only at a symmetrical arrangement of the heating source relative to welded edges. At the same time, the scheme of EBW using the horizontal beam in the horizontal plane was chosen (Figure 1). Such an arrangement of the welding pool facilitates the degassing of a liquid metal and its refinement,

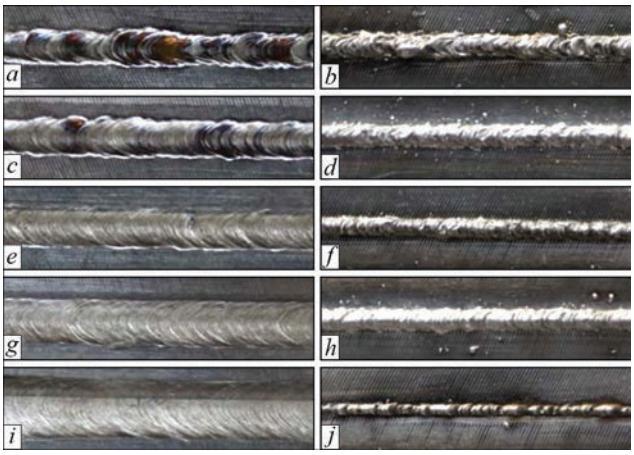

Figure 2. Face and root appearance of welds produced at different values of focusing current, mA: *a*, *b* — 629; *c*, *d* — 634; *e*, *f* — 639 — acute focus; *g*, *h* — 644; *i*, *j* — 649

Table 2. Parameters of welding plates of 2219 alloy

Specimen	Welding current, mA	Welding speed, mm/s	Acceleration voltage, kV	Focusing current, mA	Input energy, J/mm
1	85	20	60	629	255
2				634	
3				639	
4				644	
5				649	

which in turn reduces the requirements for cleanliness and quality of preparation of surfaces to be joined.

RESEARCH RESULTS

At the first stage, the effect of the focusing current on the shape and geometry of the welds was considered. For this purpose, the following welding modes were selected (Table 2). On these modes, plates of 2219 alloy were welded.

Welding was carried out with different focusing currents (Table 2), namely: 629, 634, 639, 644 and 649 mA, where the value of 639 mA is a sharp focus, i.e., the focusing current is on the surface of the plate to be welded (Figure 2, e, f). For the study, welds with the minimum 629 mA and the maximum of 649 mA focusing currents were selected. Other parameters (welding current, welding speed, etc.) were not changed.

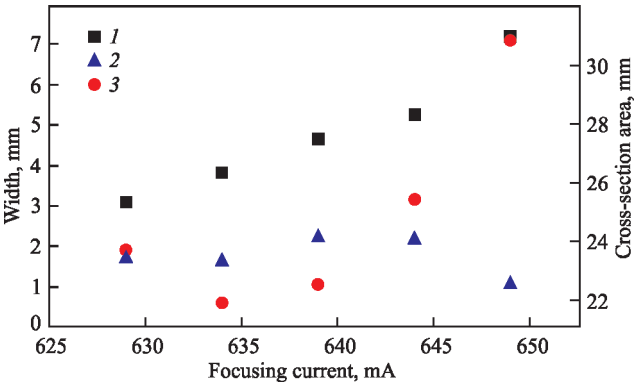

Figure 4. Dependence of the width of face weld (*1*), weld root (*2*) and cross-section area (3) on the value of focusing current

Figure 3 shows cross-sections of the welds produced on different focusing currents. According to this picture, it is possible to evaluate the proportionality of the width of the weld to its length.

The measurements showed that the growth of the width of the facial part of the weld is directly proportional to the growth of the focusing current. However, it is impossible to state this regarding the root. At smaller values of the focusing current, the root width is smaller than at acute focus. But already at much larger values of the focusing current, the width of the root decreases (Figure 4).

To analyze the microstructure of welds, the methods of scanning electron microscopy (SEM) and energy dispersive X-ray spectroscope (EDS) were used.

The microstructure of the base metal of aluminium AA2219 alloy is presented in Figure 5. The alloy microstructure consists of elongated grains of a solid aluminium solution (α); tiny and coarse bright particles distributed mainly on grain boundaries. In the image obtained with the help of backscattered electrons (BSE), a significant difference in brightness between the particles and matrix indicates the presence of heavy elements. According to the chemical composition of the base metal, copper is considered to be this element. In addition, the presence of copper was confirmed by quantitative and qualitative EDS analysis.

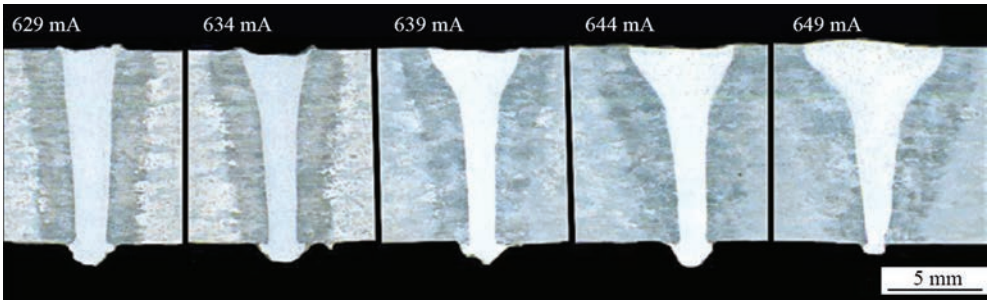

Figure 3. Influence of focusing current on welds geometry

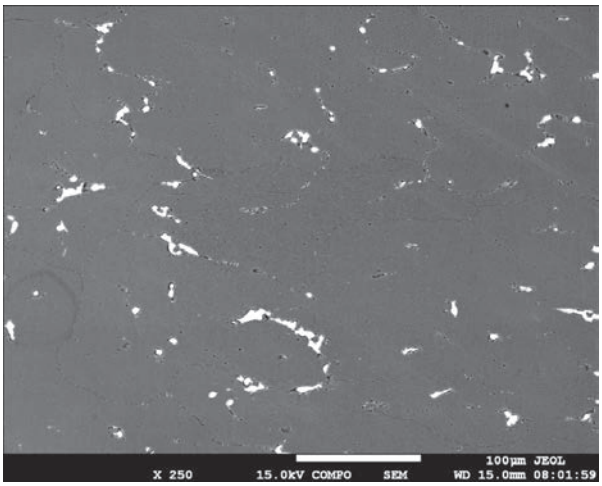

Figure 5. Microstructure of base metal of 2219 alloy

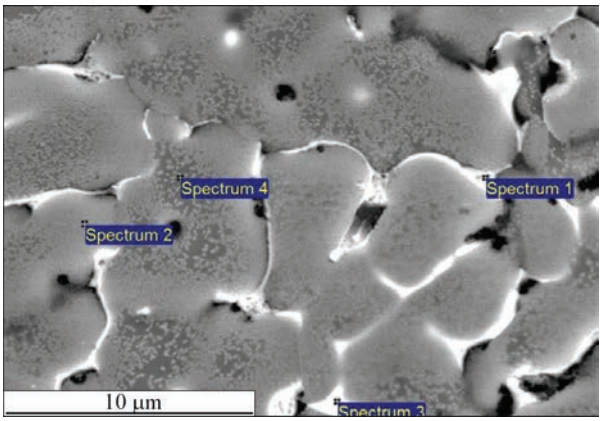

Figure 6. Microstructure of weld metal (focusing current is 629 mA)

Microstructure of the welded joint produced at a focusing current of 629 mA consists of equiaxial dendrites with embedded tiny particles, pores and α + θ Al_2Cu eutectics, separated in the interdendritic regions (Figure 6). The local elemental composition, which was measured from four regions (Spectra 1–4) is given in Table 3. Spectra 1 and 3 were obtained from the interidendritic regions, enriched by separated alloying elements. Compared to dendrites, these zones look brighter and contain about 14 at.% of copper. Accord-

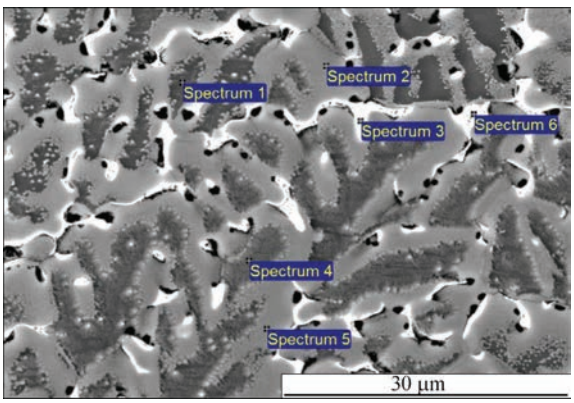

Figure 7. Microstructure of weld metal (focusing current is 649 mA)

Table 3. Chemical composition of weld metal according to EDS analysis (focusing current is 629 mA) (at.%)

Spectra	O	Al	Mn	Fe	Cu
1	6.05	79.43	0.14	0.27	14.10
2	2.65	93.72	0.17	–	3.46
3	3.21	82.15	0.22	0.37	14.06
4	3.15	95.40	0.13	–	1.32

Table 4. Chemical composition of weld metal according to EDS analysis (focusing current is 649 mA) (at.%)

Spectra	O	Al	Mn	Fe	Cu
1	2.00	96.78	0.14	–	1.08
2	0.37	94.91	0.13	–	4.59
3	7.90	71.96	0.14	0.33	19.67
4	2.74	95.57	0.15	–	1.54
5	0.57	94.57	0.18	–	4.67
6	3.95	72.86	0.11	0.31	22.79

ing to the binary diagram aluminium-copper, eutectic may be identified, containing α(Al) + θ(Al_2Cu). In Spectrum 2, a decrease in the copper content and an increase in the aluminium content were observed. The aluminium content revealed in Spectrum 2, amounted to 93.7 at.%. The highest amount of aluminium was measured in the region marked as Spectrum 4, where 95.4 at.% of aluminium was detected.

According to the binary phase Al–Cu diagram, at a homogeneous crystallization, the alloy contains about 2.36 % of α(Al) + θ(Al_2Cu) eutectics. However, the process of crystallization during welding is usually heterogeneous. This leads to the microsegregation of Cu. Therefore, the amount of eutectics in the welded joint is higher than 2.36 %, and the content of Cu in the matrix α(A1) is lower than 5.65 % [7].

The EDS analysis conducted in the weld metal with the focusing current of 629 mA relative to the selected regions is shown in Table 3.

Microstructure of the welded joint produced at a focusing current of 649 mA is shown in Figure 7 and Table 4. The dendritic microstructure was formed after crystallization of the melt pool. The local chemical composition was measured in Spectra 1-6. Spectra 1 and 4 represented dendrites with a high aluminium content. Thus, in these spectra, more than 95 at.% of aluminium were measured in these spectra. In this case, a solid aluminium solution was recorded. An increase in the copper content was observed in Spectra 2 and 5. On the image of backscattered electrons, these places were slightly brighter compared to previous ones. The copper content, which was observed in these places, amounted to 4.6 and 4.7 at.%, respectively. The brightest zones in the deposited metal were observed in Spectra 3 and 6. In such places, a significant increase in the copper content was observed. On

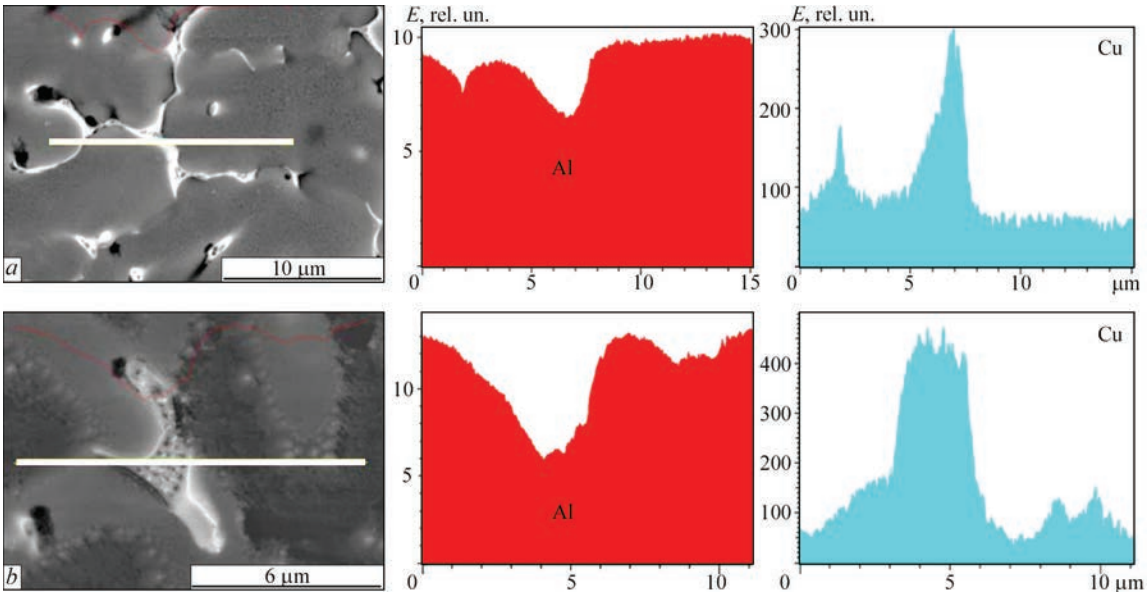

Figure 8. Linear EDS scanning through dendritic zones, in the metal of welds produced using focusing current: *a* — 629; *b* — 649 mA

the other hand, the drop of aluminium content was observed in the abovementioned Spectra 3 and 6. Spectrum 3 was characterized by the content of about 19.7 at.% of copper. In Spectrum 6, 22.8 at.% of copper was revealed. This is associated with the segregation, when interdendritic regions are enriched with alloying elements, in our case, it is mostly copper. The eutectics consisting of $\alpha(Al) + \theta(Al_2Cu)$ can be highlighted in this place, as it follows from the abovementioned binary diagram. In addition, in Spectra 3 and 6, iron was also recorded.

A high cooling rate, characteristic of EBW, not only contributes to the microsegregation, but also improves the solubility of Cu in Al, which is usually lower than 2 % in the conditions of a uniform crystallization process. In addition, it was found [8], that if the current increases, more copper amount diffuses into a solid substance. According to our observations, an increase in the focusing current from 629 to 649 mA has led to an increase in Cu content in the interdendritic regions. However, with the higher Cu content on the grain boundaries, the sensitivity to hot cracking can increase significantly.

Linear EDS scanning along the interdendritic regions were carried out in the metal of welds produced using focusing currents of 629 (Figure 8, *a*) and 649 mA (Figure 8, *b*). The placement of aluminium and copper was observed across the white lines given in (Figure 8, *a*, *b*). In the interdendritic region, a clear increase in Cu and a sharp decrease in Al were recorded. This phenomenon is associated with the presence of microsegregated eutectics in the interdendritic regions. The presence of eutectics was also confirmed by local quantitative EDS analysis.

CONCLUSIONS

1. The influence of the current focusing of electron beam welding on the formation of welds of aluminium 2219 alloy for the plates of up to 20 mm thickness was investigated. It was established that with an increase in the focusing current, the width of the face weld grows. In turn, the width of the weld root depends more on the real position of the focus of the electron beam relative to a sharp focus (639 mA).

2. The dependence of the focusing current on the distribution of copper and aluminium in the weld metal was revealed. An increase in the focusing current from 629 to 649 mA has led to an increase in the content of copper in the phase precipitates placed in the interdendritic regions. An increase in the copper content led to the formation of eutectics in the mentioned interdendritic regions. In the regions of the spectra, where a decrease in the aluminium content was recorded, also an increase in the copper content was observed, associated with segregation.

3. With the help of the energy dispersion X-ray analysis, the microstructure of the weld metal at different focusing currents was determined. Thus, coarser dendrites are formed at the expansion of the weld, which in the tested range of beam focusing corresponds to the higher value of the focusing current.

4. The local quantitative EDS analysis confirmed the presence of $\alpha + \theta(Al_2Cu)$ eutectics in the interdendritic regions of the weld metal.

REFERENCES

1. Vinogradova, N.M., Starostina, Z.I., Ivanova, T.V. (1975) Aluminium weldable alloys 1201 and 01381 for operation at low temperatures. *Aluminium Alloys,* **7**, 65–71 [in Russian].

2. Heinz, A., Haszler, A., Keidel, C. et al. (2000) Recent development in aluminum alloys for aerospace application. *Mater. Sci. Eng.*, **280**, 102–107.
3. Skalskyi, V.P., Andreikiv, O.Ie. (2006) *Evaluation of bulk damage of materials by acoustic emission method.* Lviv, Vydavn. Tsentr Nats. Un-tu [in Ukrainian].
4. Ternovoj, E.G., Bondarev, A.A. (2012) Electron beam welding of aluminium AMg6 and M40 alloys. *The Paton Welding J.,* **4**, 8–14.
5. Bondarev, A.A. (1984) State-of-the-art and advantages of electron beam welding process of aluminium alloy structures. In: *Proc. of Soviet-American Seminar on Welding of Aluminium Alloys of Cryogenic and General Purpose.* Kyiv, 10–19.
6. Yang, Z., He, J. (2021) Numerical investigation on fluid transport phenomena in electron beam welding of aluminum alloy: Effect of the focus position and incident beam angle on the molten pool behavior. *Int. J. Therm. Sci.* **164**, 106914. DOI: https://doi.org/10.1016/j.ijthermalsci.2021.106914
7. Quan, Li, Ai-ping, Wu, Yan-jun,Li, et al. (2017) Segregation in fusion weld of 2219 aluminum alloy and its influence on mechanical properties of weld. *Transact. of Nonferrous Metals Society of China*, 27(**2**), 258–271. DOI: https://doi.org/10.1016/S1003-6326(17)60030-X
8. Ruwei, Geng, Jun, Du, Zhengying, Wei et al. (2020) Multiscale modelling of microstructure, micro-segregation, and local mechanical properties of Al–Cu alloys in wire and arc additive manufacturing. *Additive Manufacturing*, **36**, 101735. DOI: https://doi.org/10.1016/j.addma.2020.101735
9. Poklyatskyi, A.G., Motrunich, S.I., Klochkov, I.M., Labur, T.M. (2021) Some advantages of welded joints of aluminium 1201 alloy produced by friction stir welding. *The Paton Welding J.,* **9**, 15–19. DOI: https://doi.org/10.37434/tpwj2021.09.03

ORCID
M.O. Rusynyk: 0000-0002-7591-7169,
V.M. Nesterenkov: 0000-0002-7973-1986,
I.M. Klochkov: 0000-0001-6490-8905

CONFLICT OF INTEREST
The Authors declare no conflict of interest

CORRESPONDING AUTHOR
V.M. Nesterenkov
E.O. Paton Electric Welding Institute of the NASU
11 Kazymyr Malevych Str., 03150, Kyiv, Ukraine.
E-mail: nesterenkov@technobeam.com.ua

SUGGESTED CITATION
M.O. Rusynyk, V.M. Nesterenkov, M. Sahul, I.M. Klochkov (2023) Influence of electron beam focusing current on geometry and microstructure of welded joints of aluminium 2219 alloy. *The Paton Welding J.*, **7**, 31–36.

JOURNAL HOME PAGE
https://patonpublishinghouse.com/eng/journals/tpwj

Received: 25.05.2023
Accepted: 06.09.2023

DOI: https://doi.org/10.37434/tpwj2023.07.05

TECHNOLOGIES FOR PRODUCING LOW-HYDROGEN FUSED FLUXES

I.O. Goncharov, V.V. Holovko, A.P. Paltsevych, A.M. Duchenko

E.O. Paton Electric Welding Institute of the NASU
11 Kazymyr Malevych Str., 03150, Kyiv

ABSTRACT

The influence of the technology of producing welding fused fluxes on the content of hydrogen in them and nature of its thermal desorption was investigated. From the fluxes produced by the method of duplex process (sequentially operating gas-flame and electric-arc furnace), hydrogen is mainly removed at temperatures to 600 °C. It was established that the content of diffusion hydrogen in the deposited metal in welding under the fused fluxes, produced by the method of duplex process, is approximately by 30 % lower compared to fluxes produced in gas-flame furnaces. The use of fused semi-products in the composition of a charge while producing agglomerated fluxes was proposed.

KEYWORDS: hydrogen, automatic arc welding under the fused fluxes

INTRODUCTION

Hydrogen embrittlement and the formation of pores in welds are common, dangerous and insufficiently studied causes of fracture of many steel metal structures [1, 2]. In welding of high-strength steels under the influence of a thermal cycle in the metal, the formation of structures is probable, which, on the one hand, contribute to the significant strengthening of the metal, and on the other hand, increase its tendency to the formation of cold cracks [3, 4]. The ability of metal to resist the initiation and propagation of cold cracks is improved when the concentration of diffusion hydrogen in it decreases. The conditions were established, under which the risk of formation of cold cracks in welded joints is reduced to a minimum. Thus, in the case of limiting the cooling rate of the metal in the temperature range of 600–500 °C to 10 °C/s, and the content of diffusion hydrogen in the deposited metal to 4 cm^3/100 g, the stress level that can be withstood by the metal of the heat-affected zone (HAZ) of welded joints of steels with a carbon equivalent C_e = 0.35–0.45 % without the formation of cold cracks, amounts to 90 % of its yield strength [5].

It is generally known that the main cause for the formation of pores in the welds during welding steels is an increased content of hydrogen in the welding pool metal and its release at the moment of crystallization as a result of an abrupt decrease in solubility [6]. The hydrogen content in the weld metal, in excess of which pores are formed in the welds during welding of low-alloy steels under manganese-silicate fluxes, amounts to 12–14 cm^3 per 100 g of weld metal [7].

The arc in automatic submerged arc welding burns in a closed envelope created by a molten slag and a layer of flux. The access of hydrogen to the arc zone from the outside is complicated. The sources of saturation of the welding pool with hydrogen are flux, oil and rust on the surface of the welding wire and on the metal edges to be welded. Moreover, the flux is determined as the main source of hydrogen. Therefore, it is important to study the content of hydrogen in welding fused fluxes and the process of its thermal desorption, the creation of technologies for the production of low-hydrogen welding fused fluxes.

PROCEDURE FOR STUDIES OF HYDROGEN CONTENT IN WELDING FLUXES

In order to control the processes of fluxes dehydration in the process of their production and use in welding, it is important to know the peculiarities of the course of the process of its desorption during the heating process. To measure the content of potential hydrogen in the coatings of electrodes, fluxes, cores of flux-cored wires, a method [6] of gradual heating of specimens to a temperature of about 1000 °C in an argon flow with conversion of compounds containing hydrogen was proposed. To avoid errors in the measurement of hydrogen due to the release of O_2, N_2, CH_4, CO and CO_2, a chromatographic method of analysis was proposed, which has high sensitivity and separation ability for the abovementioned compounds. As a result of the constant heating rate, it is possible both to determine the total water content at a temperature of 900–1000 °C, as well as to determine the nature of its bond with the substance under study (hygroscopic, adsorbed on the surface of grains, crystal hydrate, crystallization, zeolitic, dissolved in the form of OH groups). The error in measuring the amount of hydrogen is not more than 7 %. Each peak of thermal desorption in the chromatograms is a peak of hydrogen

evolution. The hydrogen content was recalculated on 100 g of the substance under study using a graduated factor of 0.57 mm^3 H_2/mBC obtained immediately before this work was carried out.

STUDY OF THE INFLUENCE OF FLUX MELTING TECHNOLOGY ON THEIR HYDROGEN CONTENT

In general, the technology of producing welding fused fluxes involves melting charge materials in a flux melting furnace, producing a homogeneous melt of the required chemical composition with the following granulation. Granulation provides obtaining flux grains of the required size and bulk weight. After granulation, fluxes are calcined, dispersed in appropriate sieves and delivered to the user. Depending on the chemical composition and technical requirements for fluxes, different types of furnaces (gas-flame and electric-arc) and methods of granulation (wet, into water) and dry (in air) can be used [8]. Until recently, Ukraine ranked first in the world in terms of production of fused fluxes. In Ukraine, fluxes of the MnO-SiO_2–CaF_2 slag system are produced most massively (more than 80 % of the total volume). These are general-purpose glass-type fluxes (AN-348A, OSTs-45, AN-348V and ANTs-1) for welding carbon and low-alloy steels and pumice-like fluxes (AN-60, AN348AP, OSTs-45P) for high-speed welding of steel structures of the same type. The first are usually produced in gas-flame furnaces, and the latter in electric-arc furnaces. In both cases, fluxes are granulated into water. Namely, the fluxes of this slag system were taken as objects for research. The aim of the work was to study the influence of technological factors on the hydrogen content at various stages of producing welding fused fluxes. The work was performed in industrial equipment at the facilities of PRJSC "Zaporizhskloflus". This equipment is composed of gas-flame and electric-arc flux melting furnaces installed side by side with the possibility of their simultaneous operation. This makes it possible to direct the slag melt from one furnace to another (duplex process). Granulation can also be performed both in wet (into water) as well as in dry (into metal moulds) method.

Gas-flame and electric-arc flux melting furnaces differ in temperatures, to which the slag melt is brought. In the gas-flame furnace, the temperature does not exceed 1400 °C, and in the electric-arc furnace it can reach 1700 °C. Therefore, in order to determine the influence of the temperature of the slag melt on its hydrogen content, AN-348AP flux was produced by the method of duplex process. In the course of melting, samples were taken first at the outlet from the gas-flame furnace, then at the outlet from the electric-arc furnace. The temperature of the slag melt during sampling was determined by an optical pyrometer. These samples were calcined on a thick-walled metal surface, as a result of which a glass-type structure was obtained and preserved until the analysis in a sealed container, which made it impossible for them to absorb moisture from the surrounding atmosphere. The research results given in Table 1, showed that the hydrogen content in the slag melt in the gas-flame furnace at the melt temperature of 1400 °C was 40.6 cm^3/100 g (sample 1), in the electric-arc furnace at the melt temperature of 1530 °C it was 14.8 cm^3/100 g (sample 2).

When the temperature was further increased to 1700 °C, the hydrogen content in AN-348AP flux melt decreased to 6.9 cm^3/100 g (sample 3). It should be noted that not only the temperature of the slag melt determined the final hydrogen content in it. The decrease in hydrogen content is also explained by better conditions for removing hydrogen from the melt in the electric-arc furnace compared to the gas-flame furnace due to more intensive mixing of the melt. In addition, during the combustion of gas in the atmosphere of the gas-flame furnace, a significant amount of water vapours accumulates (up to 15 % by analogy with steel-making furnaces). Therefore, even a significant exposure of the melt in this furnace and the use of low-hydrogen raw materials will not allow reducing the content of dissolved hydrogen in the melt below a certain limit. On the contrary, in the electric-arc furnace, there are conditions for an additional reduction in the concentration of hydrogen in the molten slag, because the probability of removing gases released from the melt during melting through gas extractors exists. In addition, intensive burning of the carbon lining and graphite electrodes leads to a decrease in the concentration of hydrogen in the slag, as is the case in steel melting slags.

Thus, the technology of flux melting using the method of duplex process leads to a decrease in the

Table 1. Hydrogen content in fluxes at different stages of production

Flux	Type of flux melting furnace	Temperature of slag melt in the furnace, °C	Hydrogen content in the slag melt, cm^3/100 g	Hydrogen content in the finished flux after wet granulation, cm^3/100 g
AN-348A	Gas-flame	1400	40.6 (sample 1)	44 (sample 4)
AN-348AP	Duplex-process	1700	6.9 (sample 3)	62 (sample 5)

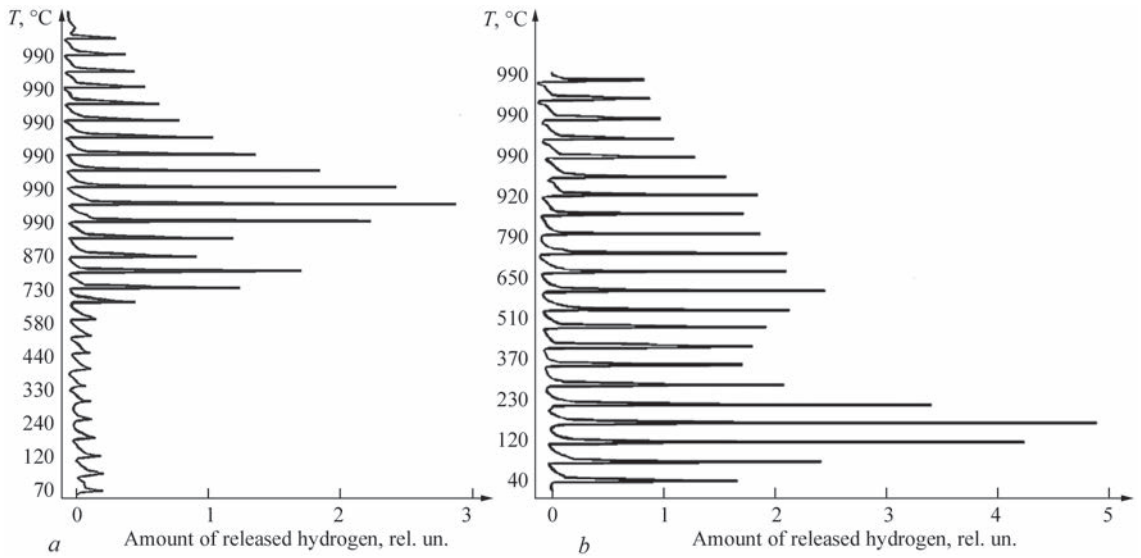

Figure 1. Chromatograms of thermal desorption of hydrogen from fluxes: *a* — AN-348A flux (sample 4) $H = 44$ cm^3/100 g (gas-flame furnace); *b* — AN-348AP flux (sample 5) $H = 62$ cm^3/100 g (duplex process)

hydrogen content in the slag melt by approximately 6 times compared to flux melting in the gas-flame furnace. It is clear that during dry granulation, the hydrogen content in the finished flux remains at the level of its content in the slag melt. The influence of melt granulation into water on the total hydrogen content in the flux remains unexplored. In order to find out this issue, the melts were granulated during sampling 1 and 3 according to the usual technology for the production of fluxes in the gas-flame and electric-arc furnaces. After granulation, the fluxes were calcined in the industrial drum dryers that provided a temperature of the flux at the output from the drying drum of 250–300 °C, as is determined by the technological documentation for the production of fluxes, were dispersed and packed. At this stage, the hydrogen content of the specimens taken from the bags as-delivered was investigated.

It was established that the temperature of the melt before the start of granulation significantly affects the final hydrogen content in the flux. Thus, at a slag melt temperature of 1400 °C, the grains with a glass-type structure are formed. At the same time, the hydrogen content after wet granulation increases by approximately 10 % (from 40.6 to 44 cm^3/100 g (final hydrogen content in AN-348A flux (sample 4)). When a slag melt heated to a temperature of 1700 °C comes into contact with water, a vapour envelope with high water vapour pressure forms around the melt particles. Considering the low viscosity of the slag melt at such temperatures, cavities are formed in the flux particles, occupying up to 80 % of the total volume of the flux. These cavities are filled with water vapours, which condenses during cooling. In general, this leads to an increase in the hydrogen content in the flux by approximately 9 times (from 6.9 to 62 cm^3/100 g (final hydrogen content in AN-348AP flux (sample 5)).

The studies of thermal desorption of hydrogen showed that the main part of moisture from AN-348AP flux is removed while heating to 600 °C (in contrast to AN-348A flux, from which hydrogen is removed at temperatures close to the melting point of the flux and, of course, enters the welding pool). To confirm this fact, Figure 1 shows chromatograms of thermal desorption of hydrogen from AN-348A flux — gas-flame furnace + granulator — sample 4) and AN-348AP flux – duplex process + granulator — sample 5).

To reduce the hydrogen content in the fused flux, the use of electric-arc furnace or the duplex process while melting flux can be recommended, which allow bringing the melt to a temperature of 1700 °C and using dry granulation fluxes. However, for the fluxes of the studied $MnO–SiO_2–CaF_2$ slag system, the use of the duplex process is more appropriate. In addition to limiting the hydrogen content, the duplex process provides a significant reduction in the content of sulphur and phosphorus in fluxes and, at the same time, prevents undesired increased losses of the main components in fluxes of this slag system. As a result, the dependence on scarce, expensive high-quality raw materials is reduced and the possibility of using wastes of metallurgical, welding and mining production in the production of fluxes is achieved, and their competitiveness grows [9, 10]. In order to reduce the hydrogen content in the flux produced by the method of duplex process, it was proposed to bring the melt to a temperature of 1700 °C, hold it at this temperature, then lower the temperature of the melt to 1400 °C and only then granulate it into water. To check these

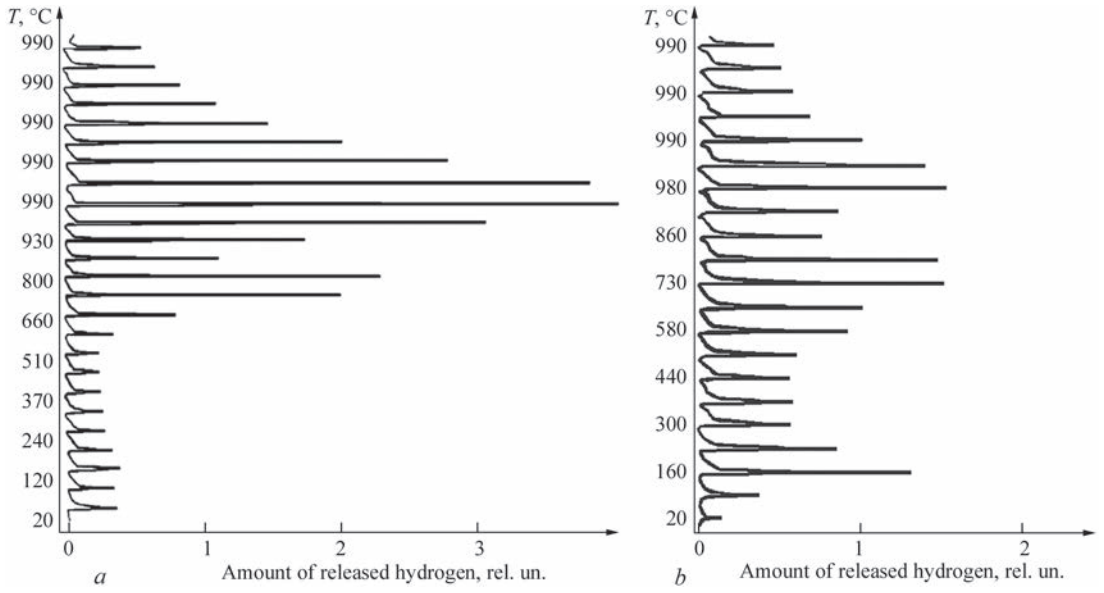

Figure 2. Chromatograms of thermal hydrogen desorption: *a* — OSTs-45 flux (gas-flame furnace) H = 36 cm^3/100g; *b* — OSTs-45M flux (duplex process) H = 30 cm^3/100 g

recommendations, the content and nature of thermal desorption of hydrogen from vitreous flux OSTs-45 (gas-flame furnace) and glass-type flux OSTs-45M (duplex process) were investigated. OSTs-45M flux was produced by heating the melt to 1700 °C, holding the melt at this temperature for 20 min, cooling the melt to 1400 °C and granulating it into water. Comparing the fluxes produced by the method of duplex process (OSTs-45M and AN-348AP), it should be noted that the total hydrogen content in OSTs-45M flux is 2 times lower than that of AN-348AP flux (30.0 and 62 cm^3/100 g respectively). This can be explained by the fact that the melt of OSTs-45M flux is cooled to a temperature of 1400 °C before granulation. As a result, a flux with a glass-type grain structure is formed. Comparing OSTs-45 and OSTs-45M fluxes, which differ in the production method, it is worth noting that both fluxes have the similar glass-type grain structure. The total hydrogen content in OSTs-45M flux (30 cm^3/100 g) compared to OSTs-45 flux produced in the gas-flame furnace (36 cm^3/100 g) is slightly lower. It was found that these fluxes differ significantly in the nature of hydrogen desorption during heating process (Figure 2). From Table 2 and the chromatograms of fluxes produced in the gas-flame furnace (AN-348A, OSTs-45), it is seen, that the main amount of hydrogen is removed at temperatures close to the melting point of the flux (990 °C). The fluxes produced by the method of duplex process (OSTs-45M and AN-348AP) are characterized by the fact that hydrogen desorption from them occurs at lower temperatures (mainly up to 800 °C). Even for pumice-like AN-348AP flux, which has a high total hydrogen content (62 cm^3/100 g), only 9.3 cm^3/100 g is released during exposure at 990 °C. For glass-type OSTs-45M flux, this value amounts to 8.7 cm^3/100 g of flux.

At the next stage of studies, the influence of the total content of hydrogen in the fluxes and the nature of its thermal desorption on the content of diffusion hydrogen in the deposited metal during welding was determined. The content of diffusion hydrogen in the metal of welds was determined by the method of chromatographic analysis according to GOST 23338–91 using OB 2178 gas analyzer designed at PWI. The objectivity of the results of measuring the amount of diffusion hydrogen is predetermined by the fact that the hydrogen released from the specimen in a sealed metal chamber is measured by the method of gas chromatography. The reliability of the results of measuring the content of diffusion hydrogen is con-

Table 2. Total content and nature of thermal desorption of hydrogen in welding fluxes

Flux	Production method		Grain structure	Total content (H), cm^3/100 g	Amount of hydrogen removed during heating in the temperature range, cm^3/100 g/%				
	Type of furnace	Granulation method			0–20 °C	200–600 °C	600–800 °C	990 °C	Higher than 990 °C
AN-348A	Gas-flame	Wet	Vitreous	44	2.6/6	4.0/9	5.3/12	3.5/8	28.6/65
OSTs-45				36	1.8/5	4.0/11	5.0/14	9.7/27	15.5/43
OSTs-45M	Duplex process			30	4.5/15	6.9/23	5.4/18	4.5/15	8.7/29
AN-348AP			Pumice-like	62	24.2/39	14.2/23	6.9/11	7.4/12	9.3/15

Table 3. Content of hydrogen in fluxes and deposited metal

Flux grade	Content of hydrogen in flux, cm^3/100 g of flux	Content of hydrogen in metal, cm^3/100 g	
		$[H]_{diff}$, deposited metal	$[H]_{res}$, weld
AN-348A	44	6.8; 7.4; 7.7/ 7.3	2.2; 2.4; 2.6/ 2.4
AN-348AP	62	4.7; 5.2; 5.4/ 5.1	1.6; 1.6; 1.7/ 1.6

firmed by numerous comparative tests of it with the mercury method of analysis according to ISO 3690 standard [11].

The specimens to analyse the content of diffusion hydrogen in the deposited metal were produced by the method of depositing a bead on an assembled specimen of 10G2FB steel. Before welding, the specimens were kept at a temperature of 800 °C for 1 h. The welding wire of Sv-10G1NMA grade with a diameter of 4 mm was stripped from the coppered coating and degreased. The surfacing was carried out on a direct current of reverse polarity on the mode: I_w = = 550–600 A, U_a = 32–34 V, V_w = 36 m/h. The parameters of the welding mode were determined from the conditions of providing the input energy required by GOST 23338–91 (not more than 3 kJ/mm), producing welds with geometric dimensions that allow an easy separation of the specimen from the run-off tabs (with width up to 22 mm and height up to 6 mm). The deposited specimen was cooled with water at a temperature of 0 °C for 3 s and immersed in liquid nitrogen. When a temperature of 196 °C was reached, the run-off tabs were removed, and the specimen was preserved in liquid nitrogen before carrying out the analysis. Three specimens were produced for each flux sample. Immediately before welding, all fluxes were calcined at a temperature of 300 °C for 1 h. The content of diffusion hydrogen was calculated according to ISO 3690.

From Table 3, it is seen that the content of diffusion hydrogen in the deposited metal when using the technology of duplex process in the production of flux is approximately by 30 % lower compared to the traditional technology of melting fluxes in the gas-flame furnace. At the same time, from the results of studying the nature of thermal desorption of hydrogen, shown in Figure 1 and in Tables 2, 3, it is seen that the content of diffusion hydrogen in the deposited metal is determined not by the total content of hydrogen in the flux, but by the amount of hydrogen removed from the flux at temperatures close to their melting point. It is clear that this hydrogen cannot be removed from fluxes by calcination of fluxes at a temperature of 300–400 °C for 1 h recommended by GOST 9087–81, which should be performed immediately before welding. It is known from [12], that such hydrogen is dissolved in the form of OH groups during melting in the furnace. I.e., the amount of dissolved hydrogen is determined by the method of flux production.

Taking into account the obtained positive results regarding the reduction of hydrogen content in welding fused fluxes produced by the technology of duplex process, the use of fused semi-products in the charge of agglomerated welding fluxes is promising.

CONCLUSIONS

1. It was established that the technology of melting flux using the method of duplex process leads to a decrease in the total hydrogen content in the slag melt by almost 6 times compared to melting flux in the gas-flame furnace.

2. When pouring the slag melt into water during granulation, the hydrogen content in the flux increases nonuniformly depending on the initial temperature of the melt: by 10 % at a melt temperature of 1400 °C and approximately 9 times at a melt temperature of 1700 °C.

3. It was established that depending on the temperature of the slag melt before granulation into water, the nature of thermal desorption of hydrogen changes. The main amount of hydrogen from the glass-type fluxes granulated at a melt temperature of 1400 °C is removed at temperatures close to their melting point (over 990 °C). For pumice-like fluxes, granulated at a melt temperature of 1700 °C, the main part of hydrogen is removed at temperatures of up to 800 °C.

4. Recommendations for the creation of technology for the production of low-hydrogen fused fluxes were developed. To reduce the hydrogen content in the fused flux, it was recommended to use the duplex process when melting the flux, which allows bringing the melt to a temperature of 1700 °C and using dry granulation fluxes. In the case of wet granulation, it is necessary to bring the melt to a temperature of 1700 °C, maintain it at this temperature, then lower the temperature of the melt to 1400 °C and only then granulate it into water.

5. It was established that the content of diffusion hydrogen in the deposited metal when using welding fused fluxes produced by the method of duplex process is approximately 30% lower compared to the option of using fluxes produced in the gas-flame furnace.

6. In order to further reduce the hydrogen content in the weld metal, a promising direction is conducting

research on the use of fused semi-products as part of the charge in the production of agglomerated fluxes.

REFERENCES

1. Milos B. Djukic, Gordana M. Bakic, Vera Sijacki Zeravcic et al. (2016) Hydrogen embrittlement of industrial components: Prediction, prevention, and models. *Corrosion*, 72(**7**), 943–961.
2. Vigdis Olden, Antonio Alvaro, Odd M. Akselsen (2012) Hydrogen diffusion and hydrogen influenced critical stress intensity in an API X70 pipeline steel welded joint: Experiments and FE simulations. *Int. J. of Hydrogen Energy*, 37(**15**), 11474–11486.
3. Poznyakov, V.D. (2023) *Welding technologies for repair of metal structures.* Kyiv, PWI [in Ukrainian].
4. Tianli Zhang, Zhuoxin Li, Frank Young et al. (2014) Global progress on welding consumables for HSLA steel. *ISIJ Inter.*, **8**, 1472–1484.
5. Poznyakov, V.D. (2017) Welding technologies for manufacturing and repair of metal structures from high-strength steels. *Visnyk NANU,* **1**, 64–72 [in Ukrainian].
6. Pokhodnya, I.K., Yavdoshchyn, I.R., Paltsevych, A.P. et al. (2004) *Metallurgy of arc welding. Interaction of metal with gases.* Kyiv, Naukova Dumka [in Ukrainian].
7. Goncharov, I.A., Paltsevich, A.P., Tokarev, V.S. (2001) Effect of hydrogen in low-alloyed weld metal on pore formation in submerged arc welding. *The Paton Welding J.*, **7**, 20–23.
8. Podgaetsky, V.V., Lyuborets, I.I. (1984) *Welding fluxes.* Kyiv, Tekhnika [in Russian].
9. Zhdanov, L.A., Duchenko, A.N., Goncharov, I.A. et al. (2012) Thermodynamic analysis of slag melts in manufacture of fused welding fluxes. *The Paton Welding J.,* **11**, 23–27.
10. Zalevsky, A.V., Galynych, V.I., Osypov, M.Ya. et al. (2001) *Method of manufacture of fused welding fluxes*. Pat. Ukraine, Publ. 16.07.2001 [in Ukrainian].
11. Volkov, V.V., Kasatkin, B.S., Mikhajlov, V.E. (1985) Comparison of methods for determination of hydrogen content in welds. *Avtomatich. Svarka,* **6**, 36–38.
12. Goncharov, I.A., Paltsevich, A.P., Tokarev, V.S. et al. (2001) About the form of hydrogen existence in welding fused fluxes. *The Paton Welding J.,* **4**, 27–30.

ORCID

V.V. Holovko: 0000-0002-2117-0864,
A.P. Paltsevych: 0000-0001-8640-7909

CONFLICT OF INTEREST

The Authors declare no conflict of interest

CORRESPONDING AUTHOR

I.O. Goncharov
E.O. Paton Electric Welding Institute of the NASU
11 Kazymyr Malevych Str., 03150, Kyiv, Ukraine.
E-mail: goncharovia@ukr.net

SUGGESTED CITATION

I.O. Goncharov, V.V. Holovko, A.P. Paltsevych, A.M. Duchenko (2023) Technologies for producing low-hydrogen fused fluxes. *The Paton Welding J.*, **7**, 37–42.

JOURNAL HOME PAGE

https://patonpublishinghouse.com/eng/journals/tpwj

Received: 19.06.2023
Accepted: 06.09.2023

DOI: https://doi.org/10.37434/tpwj2023.07.06

DETERMINATION OF THE EFFICIENCY OF PRODUCING METAL NANOPARTICLES BY EB PVD TECHNOLOGY

O.V. Hornostay

E.O. Paton Electric Welding Institute of the NASU
11 Kazymyr Malevych Str., 03150, Kyiv, Ukraine

ABSTRACT

Approaches to synthesis of Ag, Cu nanoparticles in liquid matrices and on the surface of both organic and inorganic powders and granules of different dispersity for biomedical purposes were analyzed. The advantages of nanoparticle synthesis by the methods of physical deposition in vacuum over the methods of chemical and hybrid synthesis are given. The high effectiveness and advantage of deposition from the evaporator with a directed vapour flow in vacuum are shown, compared to the classical crucible evaporation scheme. Optimal technological modes of deposition from the evaporator were established for achieving uniformity of the directed vapour flow. The dependence between the target temperature, efficiency of the evaporation scheme and evaporator to target distance was experimentally determined.

KEYWORDS: nanoparticles, electron beam evaporation and deposition, composites, dispersed systems, silver, copper, directed vapour flow, vacuum

INTRODUCTION

Due to the size effect, nanoparticles (NP) have unique properties, which allows them to be used as components of modern materials for a wide range of applications, such as optics, catalysis and biomedicine. Research works are carried out in the areas of diagnostic, therapeutic and prophylactic applications of Au, TiO, Ag, Cu, Zn, Si, CeO and Pt nanoparticles [1, 2].

ANALYSIS OF LITERATURE DATA AND PROBLEM STATEMENT

Today, there are thousands of different NP synthesis methods that allow obtaining stable colloidal solutions of single-dispersed NP and discrete coatings with NP on powders and granules. However, not all presented synthesis methods are suitable for expanded production because of a low efficiency, poor reproducibility or complex purification processes [3–5]. The available technological variants of obtaining such systems with a certain degree of conditions can be divided into three main groups: chemical, physical, hybrid (bio-assisted methods, green synthesis) [6]. Typically, chemical methods are low-cost and allow obtaining a large amount of NP. However, several disadvantages can be distinguished, among which contamination by precursor chemicals, use of solvents and formation of dangerous by-products. The so-called bio-assisted methods, biosynthesis or green synthesis also attract the attention of many researchers due to the ecological nature of these processes, which contribute to the involvement of biological systems or because they are directly related to biological systems [6–8]. These methods use, among other things, bacteria, fungi, viruses, yeast and plant extracts for NP synthesis. Although biological procedures are very promising, the main problem is the reproducibility of processes. In addition, the exact mechanisms, which are the basis of NP formation with the help of green plant extracts, are still not clarified. Physical methods are valuable because they are free from contamination with solvents, reducing agents and other reaction products [9]. However, the rate of production is relatively low, and the cost of production is very high, mainly due to the power consumption to maintain the necessary pressure and temperature conditions used in the process of synthesis. The methods of chemical synthesis and mechanical grinding do not fully meet the requirements to obtaining chemically pure NP metals. The most promising among the physical methods used for NP synthesis are methods based on the vapour phase condensation (VPC), which can be classified taking the power source as the basis. They include methods of magnetron, electrical discharge, pulsed-arc, ion-plasma synthesis, etc., among which electron beam exceeds all the mentioned sources by the specific power capacity, ease of control, efficiency and locality of heating. It should also be noted that despite the relative chemical purity of obtained nanoparticles, VPC methods have a low efficiency inherent in most physical methods. Since the formed vapour flow is distributed according to the law (cos φ) throughout the whole volume of the working chamber, it leads to undesirable consumption of condensing material, especially during the synthesis of nanoparticles from expensive metals (Cu, Ag, Au, Pt), and also to some

extent limits the list of materials, that can be used as a target (liquids, powders) [10]. In [10, 11] it was demonstrated that it is possible to use electron beam evaporation with the subsequent deposition in vacuum (EB-PVD) by means of an evaporator and a steam line, which allows directing the vapour flow directly to the target at an angle of 45°. The use of an evaporator with a vapour flow direction at an angle of 90° can increase the evaporation efficiency and increase the reproducibility of the NP synthesis process. In [12, 13], the possibility of using the EB-PVD method with a directed vapour flow for the synthesis of Ag and Cu nanoparticles in the size range of 20–40 nm in liquid matrices based on monomers, precursors of polyurethane, fatty and synthetic oils was demonstrated. Also the possibility of producing discrete coatings from Ag and Cu nanometer size on powders and granules of different dispersion [14] and medical bandages was presented [15].

AIM OF WORK AND TASKS OF RESEARCH

is to determine the optimal parameters of the technological scheme of electron beam evaporation using an evaporator with a directed vapour flow to achieve a high efficiency and reproduction of the process of nanoparticle synthesis in the volume of liquid matrices-carriers and on the surface of powders, granules, tissues. To achieve the set aim, the following tasks were solved: to produce evaporators with the ability to direct a vapour flow at a set angle; develop a procedure and adapt electron beam equipment for determination of efficiency and distribution of vapour flow over the target surface; set the technological mode of a directed deposition of silver and copper, that will provide a high value of the efficiency and reproducibility of the NP synthesis process.

MATERIALS, EQUIPMENT AND RESEARCH METHODS

Experimental works on determination of the efficiency of the technological scheme of using evaporators with a directed vapour flow and uniformity of vapour flow distribution on the target surface was carried out in the electron beam unit UE-142. Heating of the materials and transferring them to the vapour phase was carried out by an electron gun at 20 kV accelerating voltage with $5 \cdot 10^3$ Pa vacuum level in the working chamber. The evaporation schemes (angular and vertical) were developed and applied with the direction of a vapour flow from the top down (Figure 1). The vapour flow was directed at a negative angle to a horizontal plane of 45 and 90°, respectively. As an evaporator material, the refractory material graphite was used. For the steam line, molybdenum was used, which has a chemical resistance at high temperatures against evaporated metals: silver and copper.

The vapour flow above the target was formed in the form of a cone. The capture of as larger volume of the formed vapour flow by the target as possible can be realized when the distance from the steam line to the target is reduced and the area (of the surface) of the target itself is increased. At the same time, the distance between the steam line and the target affects not only the efficiency, but also the heating of the target at the expense of heat transfer. The distance from the reactor steam line to the surface of the dispersed liquid was determined based on the value of efficiency, thermal effect and uniformity of the distribution of vapour flow of the metal over the target surface. The length of the steam line was chosen based on the optimal length, at which condensation of the metal from the vapour flow on the surface of the inner walls of the molybdenum tube does not occur.

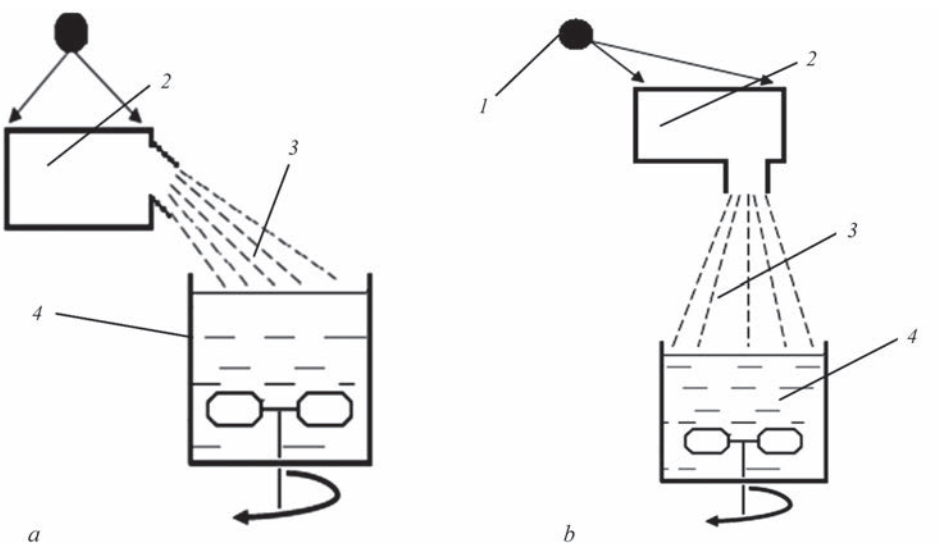

Figure 1. Technological schemes of vapour flow deposition: *a* — angular; *b* — vertical, where *1* — electron beam gun; *2* — graphite evaporator with a molybdenum steam line; *3* — directed vapour flow; *4* — liquid matrix

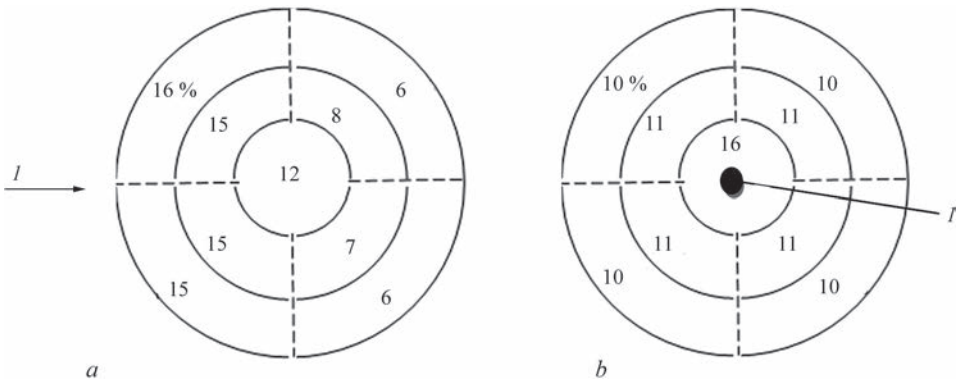

Figure 2. Uniformity of vapour flow distribution on the surface of a test copper disc, depending on the location of a graphite evaporator, %: *a* — angular scheme of vapour flow deposition; *b* — vertical one, where *1* — direction of vapour flow

The deposition was performed on the surface of a flat copper disc with a diameter of 90 mm. The size of the disc corresponded to the inner diameter of the copper water-cooling bowl, in which the target material (liquid or powder) was placed. Before deposition, the surface of the disc was cleaned and degreased with technical alcohol. The disc was arranged on the place of the bowl so that the axis of the steam line coincided with the centre of the copper disc. The distance between the evaporator and the disc corresponded to the distance between the evaporator and the surface of the liquid, powderlike target. Before placing the copper disc, it was weighed in the vacuum chamber. After conducting the experiment on the deposition of a directed vapour flow on the surface of the disc, its weight was recorded repeatedly. Similarly, before the experimental works and after, the weight of a silver weighed amount was recorded. Knowing the amount of evaporated silver and the weight gain of the copper disc, the efficiency was determined based on the proportion. Also, with the help of a chromel-alumel thermocouple, the temperature of the copper disc during the deposition process was recorded.

At the next stage of the experimental works, the process of vapour flow distribution on the target surface was determined. For this aim, witnesses were manufactured — copper flat squares of 10×10 mm. The witnesses were placed on the copper disc surface along and across the horizontal and vertical diameter of the copper disc in a 10 mm step in order to determine the vapour flow distribution over its surface. The same as for the copper disc, the weight of the witnesses was recorded before deposition and after. Having established the amount of evaporated silver, previously weighing the silver weighed amount before the experiment and after, based on the proportion, the percentage weight gain on each witness relative to the total weight gain on the witnesses was determined. On the basis of the obtained data, the diagrams of the vapour flow distribution on the target surface for both types of evaporators were constructed (Figure 2). The statistic data were processed using the computer software complex Statgraphics.

RESEARCH RESULTS AND DISCUSSION

Experimental works on the determination of vapour flow distribution over the target surface showed that the obtained results indicate a nonuniform vapour flow distribution for the angular evaporator (Figure 2, *a*). The vapour flow concentration gradient is observed along the target at an interval of 12–16 and 12–6 % for the left and right sides of the target, respectively. To the left side of the target, 67 % of the deposited material and for the right one, 33 % accounts. For a vertical evaporator (Figure 2, *b*), a gradient of the vapour flow concentration was observed from the centre to the end of the target, as was evidenced by the vapour flow distribution interval of 16–10 % for the left as well as for the right parts of the target. This indicates the relative uniformity (symmetry) of the vapour flow distribution for the left and right sides of the target and is explained by the coincidence of the steam line axis with the target centre.

The distribution of the vapour flow was determined with the help of a cover glass of the same area, the mass of which was compared before deposition and after. A series of experimental works was carried out for two types of evaporators — vertical and angular one. It was found that depending on the distance to the target, the efficiency of the evaporator with an angular orientation of the steam line ranged from 16 to 18 %, and with a vertical one was 36–40 %. Based on the fact that the efficiency of the vertical reactor is

Table 1. List of experimental data

Distance from the steam line to the copper disc surface, mm	Efficiency of evaporation scheme, %	Surface temperature of the copper disc, °C
25	61	116
45	56	72
65	40	47
85	33	41
115	22	36

2.2 times higher than the angular one, and such location provides a more uniform distribution of a vapour flow, for the further study, a scheme with a vertical arrangement was selected. The obtained experimental data of efficiency and temperature ratio of the copper disc-target depending on the distance to the target are given in Table 1.

CONCLUSIONS

1. The proposed variant of evaporators with the possibility of evaporated material (Ag, Cu) formation in a set direction of an intensive vapour flow makes it possible to reduce its consumption by 6–10 times compared to the traditional scheme.

2. It was determined that the efficiency of the evaporator with an angular steam line orientation amounts to 16–18 %, and with a vertical one it is 22–61 %. The evaporator with a vertical steam line orientation has a higher uniformity of the vapour flow distribution over the target surface compared to the angular evaporator, which provides the higher value of the reproducibility of the nanoparticles synthesis process in the volume of liquid matrices - carriers and on the surface of powders, granules and tissues. The optimum distance amounts to 70 mm, since such values do not exceed the boundary temperature and a rather high value of efficiency of the evaporation scheme.

REFERENCES

1. Khezerlou, A., Alizadeh-Sani, M., Azizi-Lalabadi, M., Ehsani, A. (2018) Nanoparticles and their antimicrobial properties against pathogens including bacteria, fungi, parasites and viruse. *Microbial Pathogenesis*, **123**, 505–526. DOI: https://doi:10.1155/2014/347167
2. Malarkodi, C., Rajeshkumar, S., Paulkumar, K. et al. (2014) Biosynthesis and antimicrobial activity of semiconductor nanoparticles against oral pathogens. *Bioinorganic Chemistry and Applications*, 1–10. DOI: https://doi.org/10.1155/2014/347167
3. Stavis, S.M., Fagan, J.A., Stopa, M., Liddle, A.A. (2018) 15 Nanoparticle manufacturing — heterogeneity through processes to products. ACS Appl. *Nano Mater*., **1**, 4358–4385. DOI: https://doi.org/10.1021/acsanm.8b01239
4. Liz-Marzán, L.M., Kagan, C.R., Millstone, J.E. (2020) Reproducibility in nanocrystal synthesis? Watch out for impurities. *ACS Nano*, **14**, 6359–6361. DOI: https://doi.org/10.1021/acsnano.0c04709
5. Sebastian, V., Arruebo, M., Santamaria, J. (2013) Reaction engineering strategies for the production of inorganic nanomaterials. *Nano Micro Small*, 10(**5**), 835–853. DOI:https://doi.org/10.1002/smll.201301641
6. Sergievskaya, A., Chauvin, A., Konstantinidis, S. (2022) Sputtering onto liquids: A critical review. *Beilstein J. Nanotechnol.*, **13**, 10–53. DOI: https://doi.org/10.3762/bjnano.13.2
7. Dhand, C., Dwivedi, N., Loh, X.J. et al. (2015) Methods and strategies for the synthesis of diverse nanoparticles and their applications: A comprehensive overview. *RSC Advances*, **127**, 105003–105037. DOI: https://doi:10.1039/c5ra19388e
8. Shanker, U., Jassal, V., Rani, M., Kaith, B.S. (2016) Towards green synthesis of nanoparticles: From bio-assisted sources to benign solvents. *Inter. J. of Environmental and Analytical Chemistry*, **96**, 801–835.
9. Iravani, S. (2011) Green synthesis of metal nanoparticles using plants. *Green Chemistry*, **10**, 2638–2650. DOI: https://doi:10.1039/c1gc15386b
10. Yakovchuk, K.Yu. (2013) Application of electron beam evaporation technology for coating deposition on powders and granules. *Tekhnologicheskie Sistemy*, **3**, 49–55 [in Russian].
11. Movchan, B.A., Yakovchuk, K.Yu. (2012) *Device and method of electron beam evaporation and directed deposition of vapor flow on substrate in vacuum*. Pat. 98085, C23C 14/24, C23C 14/28, C23C 14/30; No. a2011 06568 [in Ukrainian].
12. Makhynia, L.M., Movchan, B.O., Gornostai, O.V. et al. (2017) Effect of silver nanoparticles on the physical and chemical properties of plant oil sand the antimicrobial activity. *Biotechnologia Acta*, **6**, 35–44. DOI: https://doi.org/10.1015407/biotech10.06.035
13. Gornostai (2021) Acquisition of bandaging materials with silver nanoparticles by the methods of vacuum physical deposition. Visnyk KrNu M. Ostrogradskogo, 131, 85–91 [in Ukrainian].
14. Savelyev, Y., Gonchar, A., Movchan, B. et al. (2017) Antibacterial polyurethane materials with silver and copper nanoparticles. *Materials Today: Proceedings*, **4**, 87–94. DOI: https://doi.org/10.1016/j.matpr.2017.01.196
15. Kovinskii, I.S., Gornostai, A.V. (2012) Nanosized discrete copper oxide coatings on sodium chloride crystals deposited in vacuum from the vapour phase. *Advances in Electrometallurgy*, **2**, 146–149.

ORCID

O.V. Hornostay: 0000-0003-4961-7397

CORRESPONDING AUTHOR

O.V. Hornostay
E.O. Paton Electric Welding Institute of the NASU
11 Kazymyr Malevych Str., 03150, Kyiv, Ukraine.
E-mail: goncharovia@ukr.net

SUGGESTED CITATION

O.V. Hornostay (2023) Determination of the efficiency of producing metal nanoparticles by EB PVD technology. *The Paton Welding J*., **7**, 43–46.

JOURNAL HOME PAGE

https://patonpublishinghouse.com/eng/journals/tpwj

Received: 14.02.2023
Accepted: 06.09.2023

DOI: https://doi.org/10.37434/tpwj2023.07.07

NON-DESTRUCTIVE EVALUATION OF RESIDUAL STRESSES IN WELDED JOINTS ON THE BASE OF A COMBINATION OF ULTRASONIC TESTING AND SPECKLE-INTERFEROMETRY

L.M. Lobanov[1], V.V Knysh[1], M.O. Pashchyn[1], V.G. Kot[1], O.L. Mikhodui[1], Ye.D. Pekar[1], Luyi Huang[2], A.O. Alyoshyn[3]

[1]E.O. Paton Electric Welding Institute of the NASU
11 Kazymyr Malevych Str., 03150, Kyiv, Ukraine
[2]Zhejiang Special Equipment Research Institute
211 Kaixuan Road, Hangzhou, China
[3]"Foreign Economy Representation of the E.O. Paton Chinese-Ukrainian Institute of Welding", Ltd.
E.O. Paton Electric Welding Institute of the NASU
11 Kazymyr Malevych Str., 03150, Kyiv, Ukraine

ABSTRACT

It was found that a combination of the advantages of ultrasonic testing and electronic speckle-interferometry in the case of elimination of their disadvantages is the base for development of the method of non-destructive evaluation of residual welding stresses in full-scale structures. A procedure of non-destructive evaluation of the distribution of residual tensile welding stresses in the weld zone of a butt welded joint was developed. It is based on a simultaneous application of ultrasonic testing and electronic speckle-interferometry and fulfillment of the condition of "area equality" of the epures of balanced compressive and tensile residual stresses. The procedure was proposed for the application on specimens of single-pass welded joints of thin-sheet constructions from metallic materials with a stable structure. The subject of the study is tensile residual welding stresses in a MIG-welded specimen of a butt joint of structurally stable 1561 aluminium alloy. Residual welding stress σ_x component longitudinal relative to the weld was evaluated in the plate central area. It was found that the discrepancy of the values of residual welding stresses near the center of the welded joint of 1561 aluminium alloy is equal to approximately $0.1\sigma_{0.2}$ for this material, which corresponds to the claimed accuracy of the methods. Based on the research results, a range of procedures was proposed for the non-destructive evaluation of the residual welding stresses in full-scale welded structures, based on a combination of ultrasonic testing and electronic speckle-interferometry.

KEYWORDS: residual welding stresses, ultrasonic testing (UT), electronic speckle-interferometry (ESPI), butt joint specimen, MIG welding, compressive and tensile testing, longitudinal component of stresses, aluminium alloy, procedure of non-destructive evaluation of stresses

INTRODUCTION. RELEVANCE AND AIM OF THE WORK

Residual welding stresses (RWS), arising after welding in structural elements, are one of the factors that determine the strength, reliability and service life of products. For engineering practice, the development and improvement of experimental methods for stress determination, which are divided into two groups — destructive and non-destructive, are traditionally relevant [1].

Destructive methods are based on the measurement of deformations occurring when a welded structure element is completely or partially destroyed. They are quite common in scientific research. However, the use of destructive methods is not always appropriate for high-cost full-scale products and structures being in operation. Therefore, in engineering practice, non-destructive methods for RWS evaluation are used, during implementation of which, an examined structure remains undamaged. This is the main advantage of non-destructive methods over destructive ones.

Among non-destructive methods, the most famous are X-ray, magnetic and ultrasonic (UT-method) [2]. The latter is currently used both in the industry of Ukraine and abroad to measure residual stresses averaged over the thickness of the material [3–5]. However, for the correct evaluation of RWS, the UT-method has certain limitations related to the peculiarities of welded joint formation. Thus, the zone of tension (active) of RWS in the weld and in the area around it is formed by the field of plastic compression deformations, the values of which are characterized by a rather high gradient. A reliable evaluation of components of the plane stress state when applying the UT method, based on the propagation of elastic waves in metallic materials, is possible only in the field of elastic stresses [1]. In the zone of tensile RWS, formed as a result of plastic deformation of the weld metal and near-weld zone during shrinkage of the deposited metal,

Table 1. Characteristics of RWS evaluation methods

Number	Method of RWS determination/Availability of standard	Thickness of metal with RWS δ, mm	Base of measur. B, mm	Accuracy of the method	Advantages of the method	Drawbacks of the method
1	ESPI-method/DSTU 8852:2019	≥2	1.0	$\pm 0.1\sigma_{0.2}$ in all areas of RWS	1. It is possibile to register RWS on the surface of metal and membrane. 2. It is possibile to register RWS on the base of B_{ESPI} = 1 mm.	1. Local surface damage while drilling. 2. Difficulties in drilling solid materials.
2	UT method/none	≥3	10.0	$\pm 0.1\sigma_{0.2}$ in the zones of joints, where the values of elastic-acoustic coefficients were experimentally determined	1. There is no need to destroy metal during RWS registering. 2. It is possibile to apply the method on full-scale structures.	1. It is impossible to obtain RWS on the metal surface. 2. Averaging of RWS on the base of measuring B_{UT} = 10 mm. 3. It is necessary to determine elastico-acoustic coefficients of various zones of welded joint.

the values of elastic-acoustic coefficients differ from their values in the elastically-strained metal [6]. This reduces the reliability of RWS evaluation in the plastically-strained zone of the metal without establishing their values for this zone [7].

For engineering practice, it is relevant to obtain reliable values of tensile RWS, which (in contrast to compressive RWS) have a negative effect on the service life of welded structures. In addition, the values of RWS when using the UT-method are averaged on the measuring base B_{UT} of the UT-waves transducer, which is 10 mm. The half-width of tensile RWS distribution in the weld zone, which have a high gradient, is comparable to the value of B_{UT}. Therefore, the use of the UT-method does not allow setting the peak values of RWS in the center of the weld and close to it. However, the determination of RWS by the UT-method in the reactive compression zone, which is characterized by an insignificant stress gradient, the absence of plastic deformations and shrinkage of the weld metal, is implemented with satisfactory accuracy (Table 1).

In modern studies, to determine RWS, the method of electronic speckle interferometry (ESPI-method) is used, which is based on the elastic unloading of RWS as a result of drilling holes with a diameter d_h and a depth h_h of 1 mm on the surfaces of examined areas of a welded joint, and can be considered as conditionally non-destructive [8]. Tensile RWS when measured by the ESPI method are averaged on the base $B_{ESPI} = d_h$. This implements a localized determination of RWS, i.e. minimizes their averaging due to a small measurement base, which results in a high reliability of evaluating the peak stress values in the center of the weld (in contrast to the UT-method).

The characteristics, advantages and disadvantages of both methods of RWS evaluation are summarized in Table 1, from the data of which it can be seen that the combination of advantages of both methods while excluding their disadvantages will allow improving the reliability of non-destructive determination of RWS in full-scale welded structures.

THE AIM OF

the work is the development of RWS evaluation procedure, which is based on the combination of advantages of UT- and ESPI-methods.

PROCEDURE, OBJECT AND SUBJECT OF RESEARCH

As an object, the processes of RWS determination in a butt joint specimen were studied using the UT- and ESPI- methods.

RWS were studied in welded joints of aluminium alloy with a stable structure, during welding of which no microstructural phase transformations occur in the melting zone and HAZ, which are associated with the volume effects and can lead to a change in residual stresses from tensile to compressive.

Consideration of the residual stress state of the welded joint when comparing membrane and surface stresses is correct for small thicknesses and in a single-pass welding. Therefore, the subject of the research was RWS in a plate of a structurally stable 1561 aluminium alloy with the dimensions of 320×205×5 mm with a longitudinal butt weld (Figure 1, *a*), produced

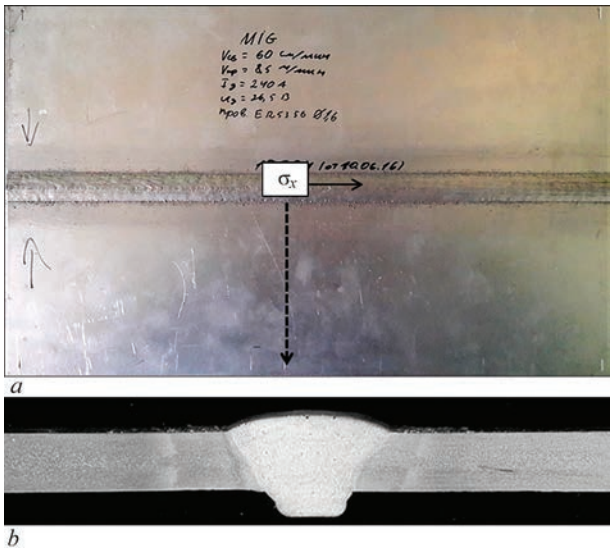

Figure 1. Specimen of butt joint of 1561 alloy: *a* — outer appearance of butt joint specimen, where a solid arrow shows the direction of σ_x action, a dotted line — the direction of stress registration by the UT and ESPI methods; *b* — macrosection of welded joint

by a single-pass MIG welding. The appearance of the macrosection of the welded joint is shown in Figure 1, *b*. MIG welding mode, residual longitudinal f_1–f_3 and transverse Δ_1, Δ_2 deflections of the plate after welding are presented in Table 2.

It can be seen that the values f_1–f_3 and Δ_1, Δ_2 are insignificant and do not exceed 1.5 mm, which excludes considerable differences between the values of membrane RWS and on the plate surfaces.

Diagnostics of the longitudinal (along the weld) σ_x component of RWS in the central part of the plate was carried out using the ESPI- and UT-methods [8, 9]. The choice of σ_x component (Figure 1) for evaluating RWS is predetermined by its larger values in the tension area (compared to the transverse component σ_y). The consequence of this is a more significant influence of σ_x (compared to σ_y) on the characteristics of the loads of the joints in operating conditions.

When registering the values of σ_x stresses using the UT-method, the UT-waves transducer was moved along the surface of the plate on the side of the weld root along its central cross-section in the directions indicated by the dotted arrows in Figure 1, *a*.

When applying the ESPI-method, the stress values σ_x on the surface of the specimen were registered on both sides of the plate in the weld center and at a distance of 7 mm from it in the directions indicated by the dotted

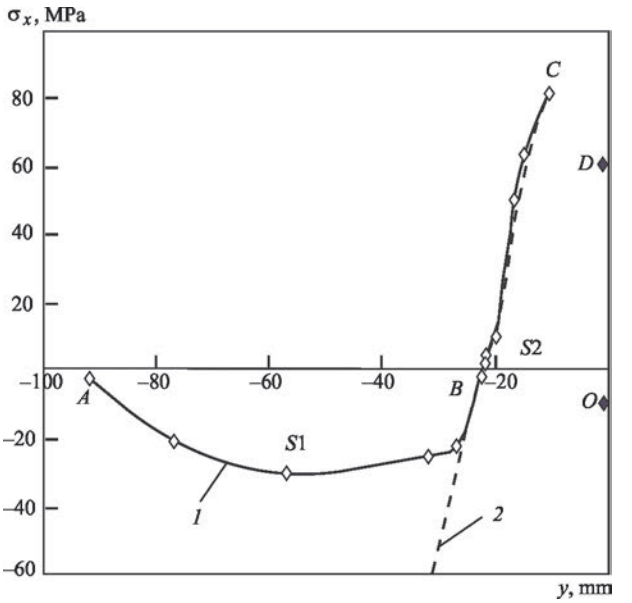

Figure 2. σ_x stresses in the central cross-section of welded joint specimen of 1561 alloy (Figure 1), obtained by the UT-method (curve *1*) and the ESPI-method (point *D*), where 2 is a straight line, showing the gradient of growing tensile RWS, *S*1 is the area of the compression epure, *S*2 is the area of the tension epure

arrow (Figure 1, *a*). The values of membrane σ_x were obtained by averaging the values of stresses over the thickness on the surface of the specimen on the corresponding areas of the outer and back surfaces of the plate.

RESULTS OF EXPERIMENTS AND THEIR DISCUSSION

Figure 2 shows σ_x stress distributions (curve *1*) in the central cross-section of the welded joint specimen (Figure 1), produced by the UT-method. The straight line *2* shows the gradient of growing tensile RWS in the active zone.

Taking into account the fact that the application of the UT-method excludes the determination of stresses in the center of the weld, the value of σ_x in this area was performed by the ESPI-method (point *D* in Figure 2). Epures of tensile and compressive RWS should have equal areas, i.e. be "balanced". Thus, the area *S*1 of the curvilinear surface between the 0–*Y* axis and the curve *AB* (compression zone) should be equal to the area *S*2 of the quadrilateral *BCDO* (tension zone) (Figure 2). However, in this quadrilateral, the position of the point *C* remains undefined on the straight line *2*, since the UT-method does not allow measuring tensile σ_x stresses in the area close to the weld metal.

Table 2. MIG welding modes and deflections of butt joint specimen from 1561 alloy

Welding speed V_w, mm/s	Welding current I_w, A	Welding voltage U, V	Grade/diameter of filler d_f, mm	$f_1^*/f_2/f_3$, mm	Δ_1/Δ_2, mm	$\sigma_{0.2}$, MPa (for BM)
10	240	26.5	ER5356/1.6	1.0/1.5/1.2	1.5/1.5	180

Note. $^*f_1$ and f_3 are the deflections of longitudinal edges of the plate; f_2 is the longitudinal deflection of the plate along the weld; Δ_1 and Δ_2 are the deflections of transverse edges of the plate, respectively, at the beginning and end of the weld; BM is the base metal.

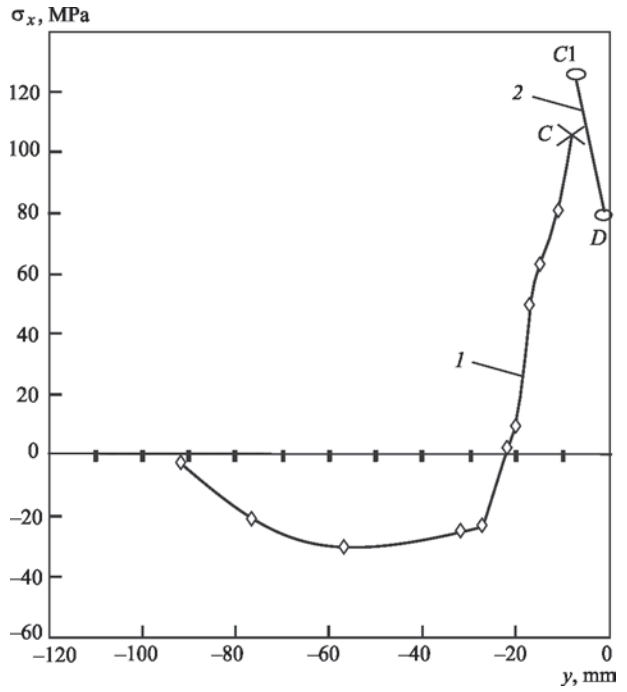

Figure 3. Residual σ_x stresses in the central cross-section of welded joint specimen of 1561 alloy (Figure 1), obtained by the UT-method (curve *1*) and the ESPI-method (curve *2*)

In the quadrilateral *BCDO*, the length of the side *BO* (the size of the width of the tensile stress zone) and the length of the side *DO* near the right angle, which in the selected scale of the ordinate axis corresponds to the value of the tensile σ_x stresses in the center of the weld produced by the ESPI method, are unchanged. Thus, the condition of equality of the areas $S1 = S2$ is set by the position of the point *C* on the straight line *2* (Figure 2). The coordinate of this point *C* on the ordinate axis (if the condition $S1 = S2$ is fulfilled) determines the value of σ_x stresses in the area near the weld, and the center of the weld on the abscissa 0–*Y* axis. Thus, the fulfillment of the condition $S1 = S2$ determines the position of the point *C* on the straight line *2* (Figure 2).

The distribution of σ_x stresses in the central cross-section of the plate (UT-method), which was extended to the point *C*, is shown in Figure 3 (curve *1*). The coordinates of the point *C* were determined under the condition that the corresponding areas of the tension and compression epures are equal. With the use of the ESPI method, the values of membrane σ_x in the center of the weld (point *D*) and near it (point *C*1) were obtained, which are shown by the straight line *2*. It should be noted that obtaining reliable values of σ_x in the region *C*1–*D* by the UT-method is impossible.

When comparing the values of σ_x at the points *C* and *C*1 (Figure 3), obtained by the UT- and ESPI-methods, respectively, it can be seen that their difference does not exceed 18 MPa, i.e., it is close to $0.1\sigma_{0.2}$ for 1561 alloy (Table 2), which corresponds to the claimed accuracy (Table 1).

Based on the abovementioned results, the procedure of diagnosing RWS in thin-sheet full-scale structures with single-pass welds, which is based on the combined application of UT- and ESPI-methods, is promising. However, it should be noted that the proposed procedure has certain limitations. Thus, with significant thicknesses and multipass welding, there is always a non-uniform distribution of residual stresses over the thickness, even with a change of sign, and the determination of the averaged stresses over the thickness is not of interest. Eliminating these limitations is the direction of further research, including using methods based on other physical principles.

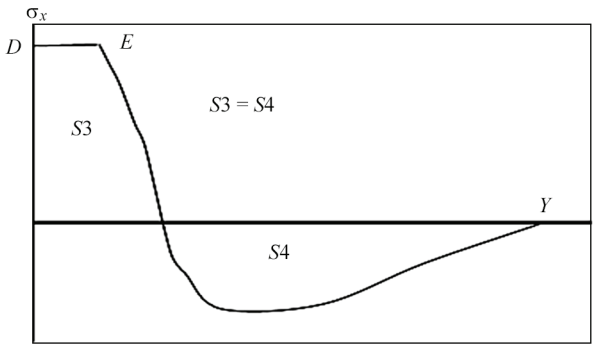

Figure 4. Epure of membrane RWS obtained using the procedure according to variant 1, where *S*3 and *S*4 are the areas of the tension and compression epures, respectively, points *D* and *E* are the values of RWS in the weld center and in the fusion zone

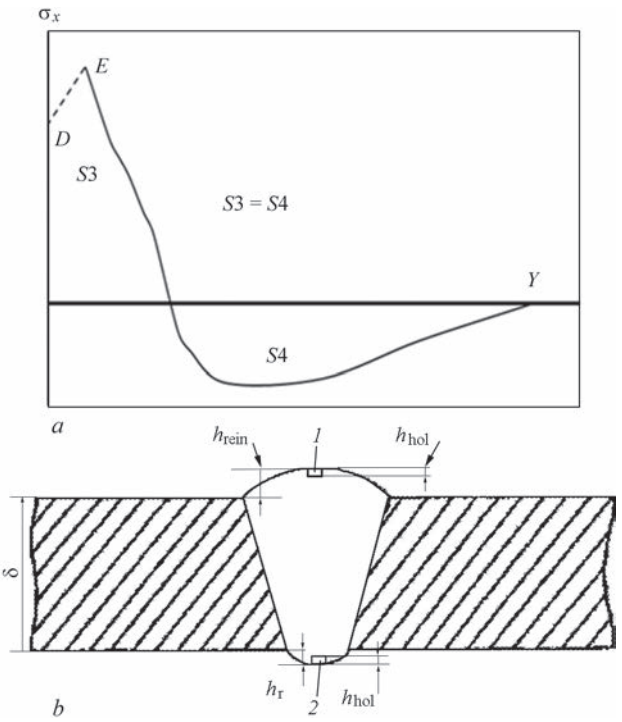

Figure 5. Procedure of RWS evaluation according to variant 2: *a* — epure of membrane RWS, where areas *S*3, *S*4, points *D* and *E* are similar to Figure 4; *b* — location of holes *1* and *2* for stress evaluation by the ESPI-method, respectively, on the outer and back surfaces of the weld

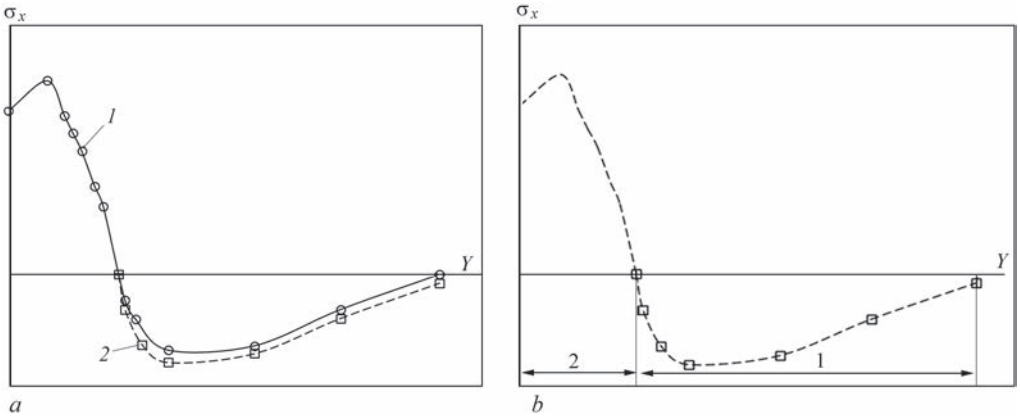

Figure 6. Procedure of RWS evaluation according to variant 3: *a* — curve *1* — epure of membrane RWS obtained by the ESPI-method on the witness specimen; curve *2* — epure of membrane RWS, obtained by the UT-method in the reactive compression zone of the witness specimen; *b* — 1 — area of the epure of membrane compression RWS, obtained by the UT-method on the structure; *2* — area of the epure of membrane tensile RWS, constructed by the method of analogies

It is possible to use the procedure in three variants.

VARIANT 1

(Figure 4) is the express-evaluation of RWS by the UT-method, which allows a quick non-destructive determination of the general level of tensile stresses in the active zone on a full-scale structure. When applying the procedure, the condition of equal stresses in the center of the weld (point *D*) and near it (point *E*) is accepted. At the same time, the geometric shape of the tension epure is taken in the form of a trapezoid (Figure 4). This excludes the determination of the features of RWS formation in the central part of the joint, which is a disadvantage of this procedure despite its advantages such as speed and ease of implementation.

1. Stages of RWS evaluation according to variant 1:

1.1. Distribution of RWS in the reactive zone (compression) is determined by the UT-method.

1.2. The area of the compression epure *S*4 is calculated (Figure 4).

1.3. Under the condition *S*3 = *S*4, the height of the trapezoid with the area *S*3 of the tensile stresses epure (Figure 4) is calculated, which on the ordinate axis determines the value of RWS at the points *D* (weld center) and *E* (fusion zone).

VARIANT 2

is the evaluation of RWS (Figure 5) by a combination of ESPI- and UT-methods, which allows obtaining the values of tensile RWS in the active zone on a full-scale structure with minimal mechanical impact on the surface of the weld metal.

The minimization of the impact is achieved due to the application of the ESPI-method for determination of RWS (in Figure 5, *a*, point *D*) exclusively on the areas of root reinforcement in the weld center (on the condition of free access to them). At the same time, the heights of the reinforcement h_{rein} and the root h_r of the weld should be greater than h_h, as is shown in Figure 5, *b*. After the determination of RWS values on both surfaces of the weld, the holes for stress registeration can be (if necessary) removed by mechanical methods of metal layers from the mentioned surfaces, provided that the thickness δ of the working cross-section of the base metal is preserved.

2. Stages of RWS evaluation according to variant 2:

2.1. The value of membrane RWS in the weld center is determined by the ESPI-method (in Figure 5, *a*, point *D*).

2.2. The UT-method determines the distribution of RWS in the reactive (compression) zone.

2.3. The area of compressive stresses *S*4 is calculated (Figure 5, *a*).

2.4. Under the condition *S*3 = *S*4, where *S*3 is the area of the tensile stress epure, the coordinates of the point *E* and the relative value of RWS (Figure 5, *a*) are calculated similarly to the method corresponding to Figure 2.

VARIANT 3

is the non-destructive evaluation of RWS (Figure 6) in full-scale structures by combining the ESPI and UT methods with the simultaneous use of a witness specimen from a similar material. Basing on the method of analogies, the procedure allows obtaining values of membrane tensile RWS in the specimen, which are equal to the stresses in a full-scale structure. The error between the distributions of compression RWS in the specimen and the structure should not exceed the claimed accuracy of the methods (Table 1). This is achieved by the equivalence of such components of the criterion of similarity of the specimen and structure as their geometric characteristics and welding modes.

3. Stages of RWS evaluation according to variant 3 (Figure 6):

3.1. The ESPI-method is used to determine the distribution of membrane RWS in the witness specimen (Figure 6, *a*, curve *1*).

3.2. The UT-method is used to determine the distribution of RWS in the reactive zone (compression) in the witness specimen (in Figure 6, *a*, curve *2*).

3.3. The UT-method is used to determine the distribution of RWS in the reactive zone (compression) in a full-scale structure (in Figure 6, *b*, area *1*).

3.4. The characteristics of the compressive stress epures of the specimen and structure are compared according to the curve *2* (Figure 6, *a*) and the curve in the area *1* (Figure 6, *b*) and their identity within the accepted measurement error is established.

3.5. Taking into account the results of the item 3.4 (identity of the compressive stress epures of the specimen and structure), the distribution of tensile RWS in the structure is constructed by the method of analogies (in Figure 6, *b*, area *2*).

Analyzing the abovementioned results, it should be noted that a combined application of the UT- and ESPI-methods allows minimizing their disadvantages (Table 1) while combining their advantages. This creates prerequisites for the development of a number of procedures for the non-destructive determination of stress states in full-scale welded structures.

CONCLUSIONS

1. It was established that the combination of the advantages of the UT- and ESPI-methods while eliminating their drawbacks is the basis for developing a method for non-destructive determination of RWS in full-scale structures.

2. It was established that the difference in the values of tensile RWS in the butt joint weld zone of 1561 aluminium alloy, obtained by the UT- and ESPI-methods, is close to the index $0.1\sigma_{0.2}$ for this material, which corresponds to the claimed accuracy of the methods.

3. A procedure for the non-destructive determination of peak values and distribution of tensile RWS in the butt joint weld zone was developed, which is based on the combined application of the UT- and ESPI-methods and compliance with the condition of "equal areas" of the epures of balanced tensile and compressive residual stresses.

4. Based on the results of the research, three types of procedures for the non-destructive determination of RWS in full-scale welded structures were proposed based on the combination of UT- and ESPI-methods.

REFERENCES

1. Guz, A.N. (1986) *Elastic waves in bodies with initial stresses*. Vol. 2. Regularities of propagation. Kyiv, Naukova Dumka [in Russian].
2. Kasatkin, B.S. et al. (1981) *Experimental methods of stresses and strains examination*. Kyiv, Nukova Dumka [in Russian].
3. Lutsenko, T.M. (2022) New systems and technologies of non-destructive testing for industry of Ukraine under current conditions. In: *Abstr. of Papers of Sci. Conf. on Welding and Technical Diagnostics for Economic Revival of Ukraine.* IAW, 66 [in Ukrainian].
4. Kudryavtsev, Y., Kleiman, J., Gushcha, O. (2000) Ultrasonic measurement of residual stresses in welded railway bridge. In: *Proc. of Conf.* on *Structural Materials Technology (Atlantic City, NJ, February 28–March 3, 2000)*, 213–218.
5. Kudryavtsev, Y., Kleiman, J., Polezhaeva, H. (2011) Ultrasonic measurement of residual stresses in welded elements of ship structure. *Applied Mechanics and Materials*, **70**, 273–278. DOI: https://doi.org/10.4028/www.scientific.net/AMM.70.273
6. Javadi, Y., Akhlaghi M., Najafabadi M. (2013) Using finite element and ultrasonic method to evaluate welding longitudinal residual stress through the thickness in austenitic stainless steel plates. *J. Mater. Des.*, **45**, 628–642. DOI: https://doi.org/10.1016/j.matdes.2012.09.038
7. Guz, A.N., Makhort, F.G., Gushcha, O.J. (1977) *Introduction into acoustoelasticity*. Kyiv, Naukova Dumka [in Russian].
8. Lobanov, L.M., Pivtorak, V.A., Savitsky, V.V., Tkachuk, G.I. (2006) Procedure for determination of residual stresses in welded joints and structural elements using electron speckle-interferometry. *The Paton Welding J.,* **1**, 24–29.
9. Gushcha, O.J. (1995), Makhort, F.G. (1995) Application of acoustic method for determination of residual stresses in welded structures. *Tekh. Diagnost. ta Nerazrush. Kontrol,* **4**, 8–15 [in Russian].

ORCID

L.M. Lobanov: 0000-0001-9296-2335,
V.V Knysh: 0000-0003-1289-4462,
M.O. Pashchyn: 0000-0002-2201-5137,
V.G. Kot: 0000-0002-4759-9992,
O.L. Mikhodui: 0000-0001-6660-7540,
Luyi Huang: 0000-0003-4155-2824,
A.O. Alyoshyn: 000-001-9696-6800

CONFLICT OF INTEREST

The Authors declare no conflict of interest

CORRESPONDING AUTHOR

M.O. Pashchyn
E.O. Paton Electric Welding Institute of the NASU
11 Kazymyr Malevych Str., 03150, Kyiv, Ukraine.
E-mail: svarka2000@ukr.net

SUGGESTED CITATION

L.M. Lobanov, V.V Knysh, M.O. Pashchyn, V.G. Kot, O.L. Mikhodui, Ye.D. Pekar, Luyi Huang, A.O. Alyoshyn (2023) Non-destructive evaluation of residual stresses in welded joints on the base of a combination of ultrasonic testing and speckle-interferometry. *The Paton Welding J.*, **7**, 47–52.

JOURNAL HOME PAGE

https://patonpublishinghouse.com/eng/journals/tpwj

Received: 24.03.2023
Accepted: 06.09.2023